



Technische Universität München
Ingenieurfakultät Bau Geo Umwelt
Deutsches Geodätisches Forschungsinstitut und
Lehrstuhl für Geodätische Geodynamik
Prof. Dr.-Ing. habil. Florian Seitz

Deformation model of the Alpine region inferred from GNSS observations

Alexandr Sokolov

Master's Thesis

Master's Course in Earth Oriented Space Science and Technology

Supervisors:

Prof. Dr.-Ing. habil. Florian Seitz
Deutsches Geodätisches Forschungsinstitut und Lehrstuhl für Geodätische Geodynamik. Technische Universität München

Dr.-Ing. Laura Sánchez-Drewes
Deutsches Geodätisches Forschungsinstitut und Lehrstuhl für Geodätische Geodynamik. Technische Universität München

Dr.-Ing. Christof Völksen
Projekt Erdmessung und Glaziologie. Bayerische Akademie der Wissenschaften

March, 2017

Declaration

This thesis is a presentation of my original research work. Wherever contributions of others are involved, every effort is made to indicate this clearly, with due reference to the literature, and acknowledgement of collaborative research and discussions.

Munich, March 1, 2017

..... (Author's signature)

Table of Contents

Declaration	i
Table of Contents	ii
List of Tables	iv
List of Figures	iv
Abbreviations and acronyms	vi
Abstract	1
1 Introduction	1
2 GNSS data analysis	3
2.1 Description of the GNSS network	3
2.2 Preparation of auxiliary data for the Bernese GNSS Software.....	6
2.3 Processing strategy of the GNSS network	6
2.3.1 Ambiguity resolution.....	7
2.3.2 Reference frame and antenna phase center variations	7
2.3.3 Satellite orbits	8
2.3.4 Troposphere estimates.....	8
2.3.5 Tides, tidal and non-tidal loading	9
2.3.6 Clustering and weekly combination	9
2.4 Quality assessment of the processed GNSS data.....	11
3 The multi-year combination and analysis	14
3.1 Datum definition	15
3.2 Performing the combination.....	18
3.2.1 Time-series analysis	20
3.2.2 Test of the datum definition	25
3.2.3 Datums effect on the station velocities	26
4 Horizontal and vertical velocity fields	29

4.1	Estimation of velocity uncertainties.....	31
4.2	Estimation of the Eurasian plate motion.....	34
4.2.1	Estimation of the Euler pole	36
4.3	Residual horizontal velocity field.....	39
4.4	Validation of the horizontal and vertical velocity fields.....	40
5	Horizontal surface-deformation field	43
5.1	Empirical covariance function.....	43
5.2	Least-Squares Collocation.....	45
5.3	The resulting surface-deformation model	47
6	Strain field	52
6.1	Computation of the strain field.....	52
6.2	Results of the strain field computation	56
7	Vertical surface-deformation field.....	59
7.1	Alternative solution for a vertical surface-deformation field.	64
8	Conclusions	66
	Acknowledgment.....	68
	Bibliography	69
	Annex A. Velocity field table.....	73
	Annex B. Discontinuities	78

List of Tables

Table 1. Contributing GNSS networks.....	3
Table 2. Processing options.....	6
Table 3. Ambiguity resolution schemes.....	7
Table 4. Bernese project related file sources.....	10
Table 5. Minimum constraints datum definition parameters.....	19
Table 6. Setup of thresholds for time-series screening	20
Table 7. Multi-year solutions and datum definition sources	26
Table 8. Average differences between solutions based on different datums.....	28
Table 9. Average values of an estimated precision from different sources and the scale factors.....	33
Table 10. Euler pole for the Eurasian plate.....	38
Table 11. The external velocity fields used for comparison.....	41

List of Figures

Figure 1. GNSS stations processed for the estimation of the deformation model in the Alps	4
Figure 2. The availability of daily observation RINEX files used in the study	5
Figure 3. The allocated clusters for the processing of the large GNSS network	10
Figure 4. Example of the network topology for the specific day 2014/01/02 and color-coded vertical residuals of station position.....	11
Figure 5. Statistics of ambiguity resolution.....	13
Figure 6. Flow chart diagram of the multi-year combination and time-series analysis.....	14
Figure 7. Example of miss-fit in the minimum constrained solution based on the IGS16P26 datum	16
Figure 8. Example of an over-constrained solution.....	17
Figure 9. Schematic illustration of relatively constrained station velocity estimation.....	18
Figure 10. The histogram of the observation continuity.....	19
Figure 11. Time-series of position residuals for station KALR (Karlsruhe).....	21
Figure 12. Station CANV (Caneva) experience the silent earthquakes.....	22
Figure 13. Time-series for station BOLG (Bologna)	22
Figure 14. Example of residual positon time-series for the reference station WTZR (Wettzell)	23
Figure 15. Weekly position residuals of station WTZR (Wettzell)	24
Figure 16. RMS of the station position residual time-series after resolving discontinuities	25
Figure 17. Helmert translation transformation parameters between weekly solutions and the multi-year solution	26

Figure 18. Comparison of reference station velocities included in the three different sources: IGB08, IGS16P26 and EPN.....	27
Figure 19. Datum effect on the stations velocities, comparison between IGB08 and EPN datums	28
Figure 20. Tectonics of the Alpen region with their plates (i.e. Eurasian, Pannonian, Adriatic and Liguria)..	29
Figure 21. Horizontal velocity field. It is strong correlated with the Eurasian plate motion.....	30
Figure 22. Vertical velocity field in the Alpine region.....	31
Figure 23. Dependency of the station velocity precision on the extension of observation period	33
Figure 24. Horizontal residual velocities after ITRF/ETRF transformation	34
Figure 25. Vertical velocities after ITRF/ETRF transformation	35
Figure 26. Illustration of the Euler pole	36
Figure 27. Statistics of horizontal residual velocities used for estimation of the Euler pole	38
Figure 28. Illustration of the Euler pole for the Eurasian plate (for the European region)	39
Figure 29. Residual horizontal velocity field after removing the Eurasian plate motion from the station velocities.....	40
Figure 30. Validation of estimated velocities.....	42
Figure 31. Empirical covariance function.....	44
Figure 32. Interpolation of measurements with the LSC for one dimensional case.....	45
Figure 33. Horizontal components of the deformation field	48
Figure 34. Surface-deformation field and residual horizontal velocity field of the Western and Central Alps	49
Figure 35. Surface-deformation field and residual horizontal velocity field of the Eastern and Central Alps..	50
Figure 36. Estimated precision of the deformation field.	51
Figure 37. Strain.....	52
Figure 38. Example of strain estimation over a regular grid.	55
Figure 39. Principal strain.	56
Figure 40. Shear strain.	57
Figure 41. Processes contributing to rock uplift in a contractional orogen	59
Figure 42. Vertical deformation model based on the station velocities directly.....	61
Figure 43. Estimated precision of vertical velocity field	62
Figure 44. Cross-section profiles of the deformation field and local topography at the Western and Eastern Alps.....	63
Figure 45. Vertical surface-deformation model based on the separate analysis of the trend function and a stochastic signal.....	65

Abbreviations and acronyms

CODE	Center for Orbit Determination in Europe
CORS	Continuously Operating Reference Station
DORIS	Doppler Orbitography and Radiopositioning Integrated by Satellite
EPN	EUREF Permanent GNSS Network
ETRF	European Terrestrial Reference Frame
EUREF	Regional Reference Frame IAG Sub-commission for Europe
FReDNet	Friuli Regional Deformation Network
GAIN	Geodetic Alpine Integrated Network
GIA	Glacial isostatic adjustment
GLONASS	(ГЛОНАСС) Глобальная навигационная спутниковая система (transliteration: Globalnaya navigatsionnaya sputnikovaya sistema), or "Global Navigation Satellite System"
GMF	Global Mapping Function
GNSS	Global Navigation Satellite System
GPS	Global Positioning System
GREF	Integriertes geodätisches Referenznetz Deutschlands
HOI	High order ionosphere
IAG	International Association of Geodesy
IERS	International Earth Rotation and Reference Systems Service
IGS	International GNSS Service
ITRF	International Terrestrial Reference Frame
ITRS	International Terrestrial Reference System
LGM	Last glacial maximum
NNR	No-Net-Rotation
NNT	No-Net-Translation
PCV	Phase center variation
PPP	Precise Point Positioning
QIF	Quasi-Ionosphere-Free
RENAG	Reseau national GNSS permanent
RINEX	Receiver independent exchange format
RMS	Root mean square
SINEX	Solution independent exchange format
VMF1	Vienna Mapping Function 1
ZPD	Zenith path delay

Abstract

This study focuses on the determination of a horizontal and vertical surface-deformation model of the Alpine mountain belt and surrounding regions. A network of 210 permanent GNSS stations with collected observations during 12.4 years is used for the precise determination of station positions and velocities. For most of the stations, the station velocities are estimated with precision of approximately 0.1 mm/a for horizontal components and about 0.3 mm/a for the vertical. The discrete station velocities are the input data for the estimation of a continuous surface-deformation model and strain field, revealing the ongoing tectonic processes in the Alpine region. The interpolation of station velocities is performed by the least-squares collocation method. The resulting vertical surface-deformation model reveals an uplift of the Alpine belt of about 2.5 mm/a at the Western and Central Alps, while in the Eastern Alps the uplift rate is approximately 1.5 mm/a and decreases towards the eastern side of the mountain belt. Additionally, in the local neighborhood outside the mountain belt, three local subsidence zones with rate of $1.0\text{--}1.5 \text{ mm/a}$ are observed. Those subduction zones are near Venice in Italy, near Marseille in France and at the valley in Eastern France near the north-western boundary of the Alps. The horizontal surface-deformation model reveals a velocity pattern of the Alps mainly as weak stretching of the mountains longitudinally along the belt with the superimposed northwards motion in the Eastern Alps, e.g. at the collision zone of the Adriatic microplate with the Eurasian plate. The strain field helps to determine the behavior and the interaction of the microplates at the Adriatic-Alpine region, e.g. the compressional strain rate of approximately 20 nstrain/a is well observed at the Friuli region in Italy. At the exterior of the mountain belt the compressional strain of $5\text{--}10 \text{ nstrain/a}$ is observed. In the central mountain belt, near the seismically active zones in the Western Alps and in the Eastern Alps at the triple junction of the Eurasian plate with the Adriatic and Pannonian microplates, a tensile stress of approximately 10 nstrain/a is revealed locally.

1 Introduction

Modern geodetic techniques such as the Global Navigation Satellite Systems (GNSS) are able to provide precise positions for Continuously Operating Reference Stations (CORS). Observations collected over long time periods (e.g. several years) at regionally distributed GNSS stations allow to identify small signals related to intraplate velocities, surface-deformation, glacial isostatic adjustment (GIA), mountain-building, hydrological, anthropogenic effects, etc.

The objective of this study is the determination of the surface-deformation in the Alpine region. The existing studies of the Alpine belt often had a regional scope, showing the velocity fields and deformation models for a segment of the mountain chain. The present regional studies in: the Western Alps (Nocquet et al., 2016; Calais et al., 2002), the Swiss Alps (Egli et al., 2007; Tesauro et al., 2006) and the Eastern Alps (Haslinger et al., 2009; Umnig et al., 2015; Grenerczy et al., 2000, 2005) cover

specified regions only. There are also several results with comparable network density covering the entire Alps usually based on the multi-network combinations (Caporalli et al., 2009) or combining results of several processing centers; or on studies performed by the precise point positioning (PPP) scheme (Serpelloni et. al, 2013).

In addition to the surface-deformation model, the estimation of the strain components is also undertaken in this study. The recent studies on strain in the Alpine region and surroundings are undertaken by Bada et al. (2007) on the Adriatics, by Calais et al. (2002) on Western Alps, Grenerczy et al. (2000) on Central Europe, Serpelloni et al. (2005) and Sue et al. (2007) on the Alps region.

The advantage of this study is a homogeneously processed GNSS network of 210 stations, with observations collected during 12.4 years, covering the entire Alpine mountain belt region and the surroundings up to one thousand kilometers. Another advantage of this study is the use of only one reference frame for the entire period as well as unified processing standards. Thus, the resulting station position time-series are free from discontinuities caused by, for instance, due to switching from relative antenna phase center variation model to the absolute one (e.g. at 2006) or due to change of the reference frame from IGS05 to IGS08 (e.g. at 2012).

The major steps from processing GNSS observations to the estimation of the surface-deformation model are described in allocated sections. The general description of the GNSS network, and the description of the processing strategy is provided in the Chapter 2.

The Chapter 3 explains details of the multi-year combination, datum definition, constraining method and validation of the estimated station velocities.

The resulting horizontal and vertical velocity fields are provided in the Chapter 4. A short overview of the tectonic settings on the Alpine region is provided at the beginning of the Chapter 4. Since the formal errors of the station positions and velocities are usually overestimated, the subsection 4.1 describes the empirical derivation of a more realistic velocity uncertainty. The methodology for the estimation the tectonic plate motion using the Euler theorem and the resulting residual horizontal velocity field are described in subsections 4.2 and 4.3 consequently.

The methodology for the estimation of the surface-deformation model by means of Least-Squares Collocation (LSC) is provided in the Chapter 5. The resulting horizontal and vertical surface-deformation fields are provided in the Chapters 5 and 7 accordingly.

The Chapter 6 is covering the method for the computation of the strain field and the end of this chapter describes the results: the principal strain and shear strain fields, revealing the interaction of the tectonic micro-plates at the Alpine-Adriatic region.

Numerical results, supplements and the source code of this study are available in digital format in the attached CD.

2 GNSS data analysis

The determination of small signals such as surface-deformation and mountain building process may be performed by analyzing GNSS data from geodetic networks in post-processing. Here precise satellite orbits, Earth orientation parameters and other corrections are computed and included as known parameters in the GNSS data analysis. The main activities associated to the estimation of the precise satellite orbits, troposphere and ionosphere corrections for GNSS observations, antenna phase center corrections, biases and calibrations, etc. are performed by the International GNSS service (IGS), Dow et al. (2009).

In this study, GNSS station positions and velocities are estimated using the double-difference baseline approach and the least-square adjustment implemented in the Bernese GNSS software, Version 5.2 (Dach et al., 2007, 2015). The processing strategy follows in general the guidelines applied for the EUREF (Regional Reference Frame IAG Sub-commission for Europe) Permanent GNSS Network (EPN) (http://www.epncb.oma.be/_documentation/guidelines/guidelines_analysis_centres.pdf), they are mainly outlined by the Center of Orbit Determination in Europe (CODE) (Dach et al., 2015).

2.1 Description of the GNSS network

For the estimation of the velocity field in the Alpine region GNSS observations collected at nearly 210 continuously operating GNSS stations in the Alps and surrounding regions were used (Figure 1). GNSS stations belonging to different national and international geodetic networks were selected (Table 1).

Nominally, the station metadata, describing the station set up, monument, approximate position, GNSS equipment used (antenna, radom and receiver) for allocated time-intervals are recorded by the station operator in so-called site-log in a format defined by the IGS (see example in: <ftp://igscb.jpl.nasa.gov/pub/station/general/blank.log>).

Table 1. Contributing GNSS networks.

Network	Description and source
Alpen	The set of stations from the various GNSS networks distributed all over the Alpine region (Aoudia et al., 2007). The main contributing network is the Geodetic Alpine Integrated Network (GAIN). ftp://ftp.ictp.trieste.it/a/aborghi/WORLD/
Austria	The set of GNSS stations in Austria, mainly in the Alpine region (Haslinger and Stangle, 2007). ftp://olggps.oeaw.ac.at/pub/
FReDNet	The network covering the North-East of Italy (Caporali et al., 2009). ftp://www.crs.inogs.it/pub/gps/rinex
RENAG (partially)	The French GNSS network with dense coverage in Eastern France (Nocquet et al., 2016). A set of 50 stations in the mountain region is included in the project. Low availability of metadata (i.e. site-logs) along with poor completeness and consistency of RINEX file headers. ftp://webrenag.unice.fr/data/ and ftp://renag.unice.fr/data

GNSS data analysis

Network	Description and source
ORPHEON (partially)	The GNSS network in France for differential positioning. (http://reseau-orpheon.fr/) For the analysis, 51 stations are included. The station information metadata is provided by the RENAG network. ftp://webrenag.unice.fr/data/ and ftp://renag.unice.fr/data
GREF (selected sites)	The GNSS network in Germany. The nine stations are selected to provide improved homogeneous coverage of the network. ftp://igs.bkg.bund.de/GREF/obs
IGS (selected sites)	From the IGS network, 22 stations are included for referencing. ftp://igs.bkg.bund.de/IGS/obs
EPN/EUREF (selected sites)	From the EPN/EUREF network (Bruyninx et al., 2012, 2013) additionally 13 sites are selected for better referencing and more homogeneous coverage. ftp://igs.bkg.bund.de/EUREF/obs
DGFI	Five stations in the Northern Alps, in the south of Bavaria (Seitz et al., 2014).

The spatial distribution of the contributing GNSS stations is illustrated in the Figure 1. The network consists of freely available GNSS data in the Alpine region as for May 2016. Unfortunately, the coverage is not uniform. Stations located at distances up to one thousand kilometers from the Alps are included into the network for an improved estimation of the tectonic plate motion and the determination of the crustal deformations with respect to the stable surrounding area (Pelzer, 1985).

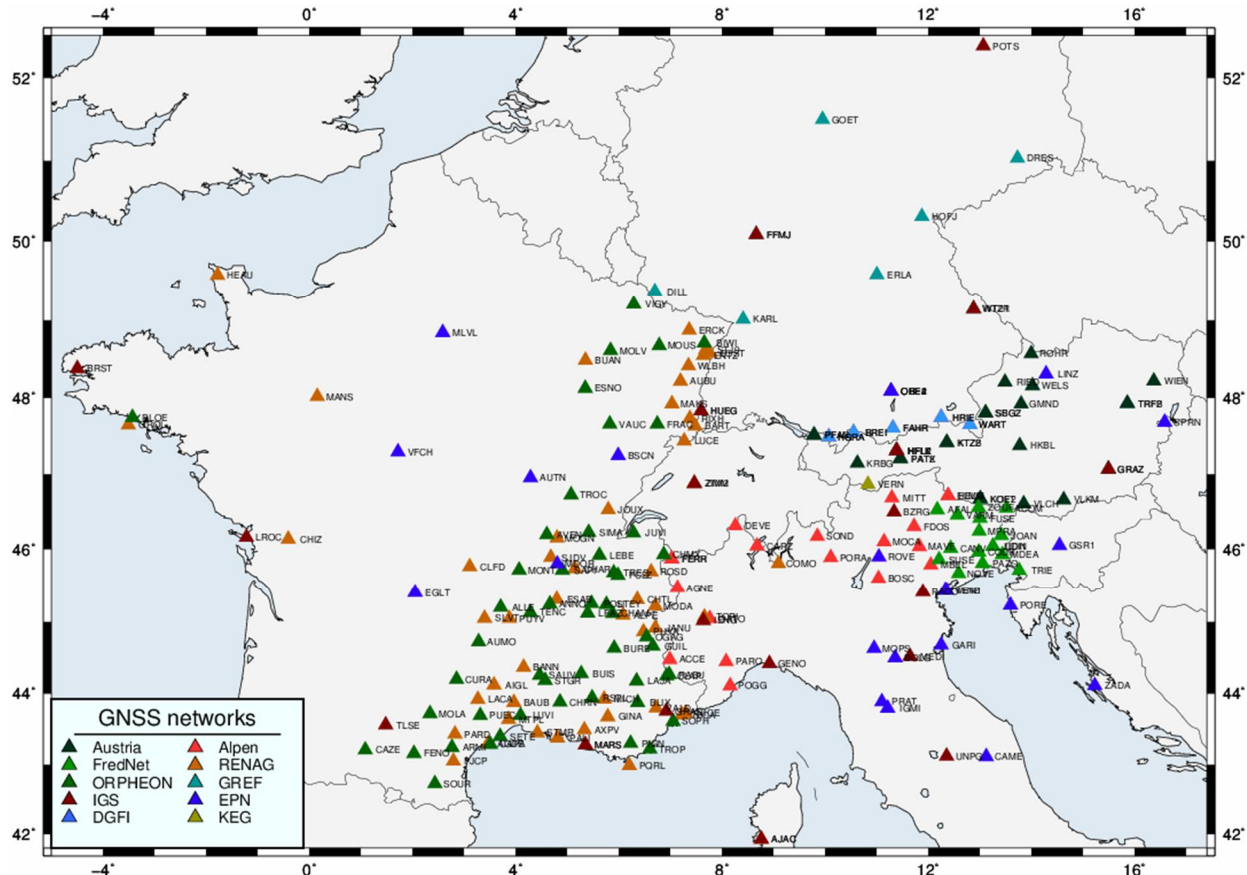


Figure 1. GNSS stations processed for the estimation of the deformation model in the Alps. The stations of the contributing GNSS network are color-coded.

Most of the stations are mounted on concrete monuments that reach down to the bedrock. Several stations are mounted on steel-masts on the roofs of buildings. Since the current study involves many networks, in general, it is possible to classify them by the following categories (Serpelloni et al., 2013): geodetic networks (e.g. IGS, EUREF, GREF), stations of which are located mostly in stable areas and provide good continuity of observations and complete metadata; geophysical networks (e.g. FReDNet, RENAG), stations of which are located in hazard areas like: seismically active zones and with careful maintenance of the site-logs to resolve discontinuities; and differential network (e.g. ORPHEON) stations of which are located on grids with regular pattern and used for differential navigation, those stations are often provided with poor maintenance of the metadata.

Nominally, GNSS observations are provided in so-called receiver independent exchange format (RINEX) files. Generally, the amount of available GNSS observations, provided as RINEX data, varies with time (Figure 2). The observation period is covering the time-span 2004/01/01 – 2016/05/30. The total number of the daily RINEX files is almost 0.57 Mi. The maximum number of stations in the network occurred between 2012-2015, reaching nearly 180 stations per day. Figure 2 shows the offsets in the total number of daily RINEX files caused by the limited number of available GNSS data. For instance, the offset in 2015 is caused by the reduction of available stations from the ORPHEON network.

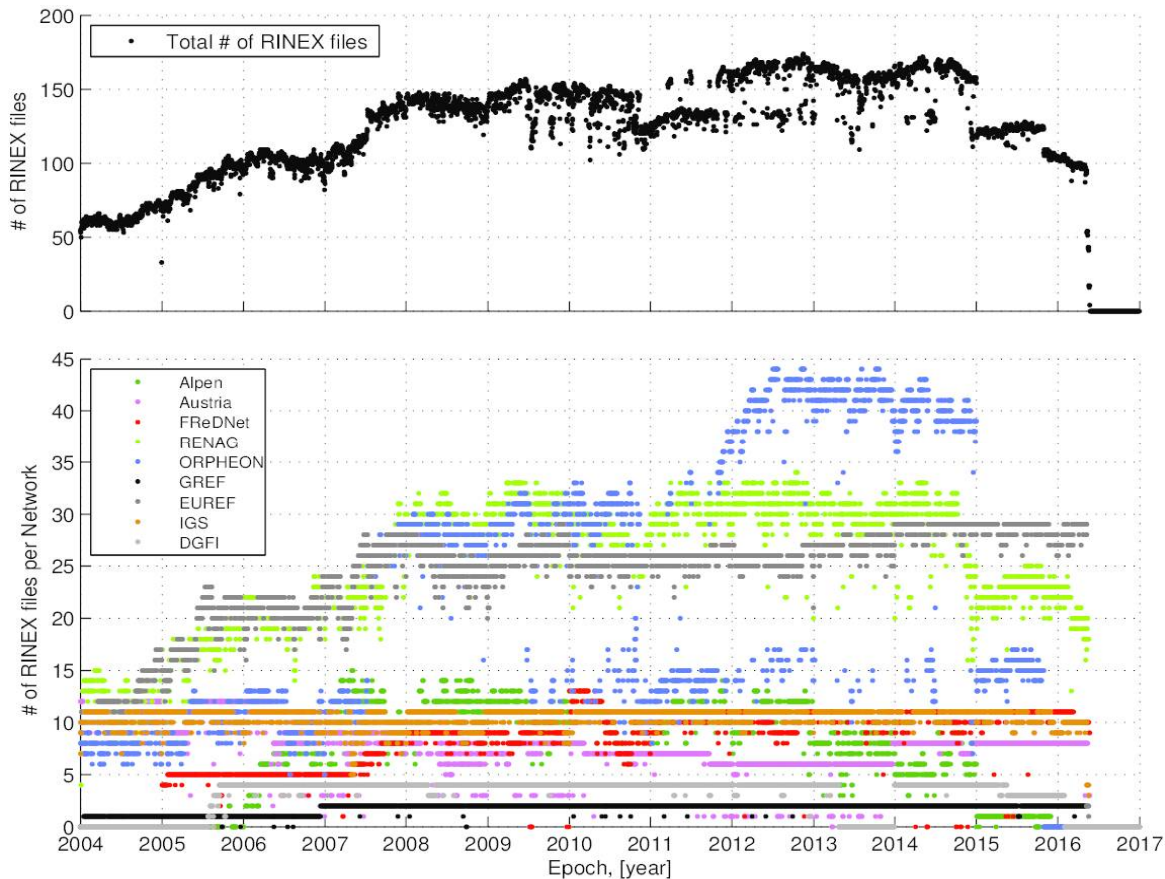


Figure 2. The availability of daily observation RINEX files used in the study. The GNSS networks are color-coded.

2.2 Preparation of auxiliary data for the Bernese GNSS Software.

One of the most time-consuming steps is preparation of the station-metadata, which contains information about station characteristics, equipment, and their changes. Usually, this information is provided in the site-logs. The consistency of such site-logs and their availability is often a problem, especially for the non-IGS or non-EPN/EUREF sites. In such cases, the only way to obtain information about the GNSS equipment is the header of RINEX observation file. For some stations without an available site-log, the information in the RINEX headers is not reliable, especially at the beginning of the station observation period. Obviously, station operators need some time to implement the standards used by the IGS. In case of the ORPHEON network, the metadata is provided by a web-interface (<http://webrenag.unice.fr>).

To get a-priory station coordinates and velocities of the stations, all the major networks were processed individually, with gaps of several months between processed data. Additionally, the first routine processing helped to check and verify for completeness and consistency of the metadata and the other campaign related files. For the homogeneous introduction of the datum into the networks, a set of five IGb08 stations (i.e. BRST, GRAZ, LROC, POTS and TLSE) was included into the analysis of all the major sub-networks for further constraining and combination.

2.3 Processing strategy of the GNSS network

The main idea of the GNSS observation analysis is the precise estimation of the relative network geometry. Over a large time-span (e.g. years), the changes in the relative geometry reveal the tectonic processes, such as mountain building, surface deformation, strain accumulation, etc. This relative network geometry is preserved in the free normal equation (NEQ) files that are later used for the multi-year combination.

The processing of the network is performed in the Bernese GNSS Software V5.2 (Dach et al., 2015) using the double-difference processing strategy recommended for this type of analysis and used by the EUREF community. The description of the analysis strategy is summarized in the Table 2.

Table 2. Processing options.

Parameter	Option/value
Systems	GPS and GLONASS
Basic observable	Ionosphere-free linear combination (L3)
Baselines forming strategy	By maximizing the number of common observations between stations with bonus factor for short baselines
Sampling rate	30 seconds
Elevation cut off angle	3°
Elevation-dependent weighting of observations	$1/\cos^2(z)$, where z is the zenith angle

The main aspects of the ambiguity resolution, troposphere parameter estimation, reference frames, satellite orbits, antenna phase center variation and clusterization are allocated into separate subsections from 2.3.1 to 2.3.6.

2.3.1 Ambiguity resolution

The advantage of the double-difference processing strategy proposed by CODE is the advanced ambiguity resolution scheme (Dach et al., 2015). It includes ambiguity resolution strategies as they are provided in the Table 3.

Using the so-called wide-lane ambiguity resolution scheme, each baseline is processed twice. In a first step, the Melbourne-Wübbena or wide-lane (L5) linear combination is processed and the wide-lane ambiguities are resolved and stored. In the subsequent step, the ionosphere-free (L3) linear combination is processed, the previously estimated wide-lane ambiguities are introduced as known, and the narrow-lane (L1) ambiguities are resolved. The Quasi-Ionosphere-Free (QIF) ambiguity resolution scheme is applied on the remaining real-valued ambiguities on baselines less than 2000 km. Then the phase-based wide-lane scheme is used resetting all previously fixed ambiguities. Finally, the Direct L1/L2 ambiguity resolution scheme is applied instead of the above mentioned sequence of strategies on very short baselines (e.g. less than 20 km).

The SIGMA resolution algorithm is iterative and exploits a-posteriori RMS error in the least-squares adjustment. The RMS errors are sorted in ascending order and a set (e.g. first 10) of best determined ambiguities is resolved (rounded to nearest integers) and introduced as fixed for the next iteration.

The ionosphere model from CODE (<ftp://ftp.unibe.ch/aiub/CODE/>) is used to assist the ambiguity resolution. The high order ionosphere (HOI, the second and third terms), is applied in the final network processing step.

Table 3. Ambiguity resolution schemes.

Scheme	Baseline, max. length, km	Baseline observable	Ambiguities resolved	Resolution Strategy	System
Code-Based Wide-Lane	Long, 6000	Melbourne-Wübbena & L3	Wide-Lane & Narrow-Lane	SIGMA	GPS
Phase-Based Wide-Lane	Medium, 200	L5 & L3	Wide-Lane & Narrow-Lane	SIGMA	All
Quasi-Ionosphere-Free (QIF)	Long, 2000	L1 & L2	L1 & L2	QIF	All
Direct L1/L2	Short, 20	L1 & L2	L1 & L2	SIGMA	All

2.3.2 Reference frame and antenna phase center variations

An IGS reference frame normally corresponds to a subset of ITRF positions and velocities for specified globally distributed GNSS reference stations, with explicitly stable time-series in a long-term (i.e. years). The IGS08 (Rebischung et al., 2011) reference frame corresponds to the ITRF2008 (Altamimi et al., 2011) reference frame. After the IGS reference frame is refined by including or excluding some

stations, its name is changed accordingly. For instance, the IGb08 reference frame is the improved version of the IGS08. The main difference between the IGS08/IGb08 and the ITRF2008 is the applied correction model the antenna phase center variations. The ITRF2008 coordinates are consistent with the igs05.atx set of antenna calibrations (Schmid, et al., 2007), while the IGb08 are consistent with the updated igs08.atx model (Schmid et al., 2016). Internally, the IGS08/IGb08 coordinates are more self-consistent than the ITRF coordinates, nominally, ITRF2008 and IGS08/IGb08 are considered to be identical as there are no translations, rotations or scale between them.

The antenna phase center variation (PCV) file (in Bernese format) is downloaded from the CODE server (originally, the igs08.atx file is maintained by the IGS, and converted by CODE into Bernese format). For some receiver antenna types the phase center variations for GLONASS system are still not provided by the IGS. Therefore, the missing antenna patterns for the GLONASS system were derived (adopted) from the GPS system. In this study, for stations with undefined antenna radom (neither in the site-log, nor in the RINEX file) antenna pattern without radom (type NONE) is assumed.

2.3.3 Satellite orbits

The final satellite orbits and Earth rotation parameters were downloaded from server of the Center of Orbit Determination in Europe (CODE). The orbits for the time-span 2014-2016 are downloaded from (<ftp://ftp.unibe.ch/aiub/CODE/>). The latest reprocessed satellite orbits for the period 2004-2013 are taken from (ftp://ftp.unibe.ch/aiub/REPRO_2013/CODE/). The reprocessed orbits differ from the nominal orbits by enabling the albedo model by Rodriguez-Solano et al. (2012), satellite antenna thrust effect, and the a-priori solar radiation pressure model switch-off. The GLONASS orbits are realized by CODE in the same reference frame as the GPS orbits. Satellite orbits, Earth rotation parameters and satellite clocks are fixed to the CODE products referring to the IGS08/IGb08 reference frame (Rebischung et at., 2011).

2.3.4 Troposphere estimates

For the estimation of the troposphere parameters, the Global Mapping Function (GMF, Böhm et al., 2006) has been used. The troposphere parameters are composed of a dry (hydrostatic) part and site specific corrections: wet part and horizontal gradients. The a-priori troposphere zenith path delay (ZPD) (dry part) is computed using the dry GMF. The ZPD corrections are computed based on Global Pressure Temperature model (GPT, Böhm et al., 2007) using the wet GMF at 1-hour sampling with relative constrains to 5 m. The horizontal gradient parameters (along North-South and East-West) are estimated using the model by Chen and Herring (1997) as linear variation (24-hour sampling) with relative constraining to 5 m.

According to the study on the performance of the Vienna Mapping Function 1 (VMF1, Böhm et al., 2006) by Steigenberger et al. (2009), it could be shown that the VMF1 provides comparable results with the GMF in the European region, including the Alps. The application of the VMF1 is more important for precise determination of the height component, while, in this study, the objective is the determination of the station velocities. The processed network is a regional network, hence it benefits from the shorter baselines between stations. The shorter baselines allow an improved estimation (and elimination) of the troposphere effects, in contrast with the lower density global geodetic GNSS networks (preferable use of VMF1). Moreover, the application of the VMF1 is more computationally expensive than the GMF. Therefore, we used GMF in this study.

2.3.5 Tides, tidal and non-tidal loading

The corrections for a solid Earth tide, permanent tide, and solid Earth pole tide are applied according to IERS Conventions 2010 (Petit and Luzum, 2010). The ocean tide loading is estimated using the FES2004 model, provided at (<http://holt.oso.chalmers.se/loading/>). According to the IERS and IGS conventions (for official products), the non-tidal loading such as, ocean bottom pressure and hydrological effects are not reduced. Other effects causing site displacements like post-earthquake relaxation or post-glacial rebound are not modeled.

The changing mass distribution in the atmosphere consist of the tidal and non-tidal part. The atmospheric tidal loading is reaching the maximal amplitudes of 1.5 mm at the equatorial area. Still, because of the uncertainty of atmosphere tidal models, the IGS recommends at moment not to apply the corresponding corrections to the observations (Dach et al., 2015). This will probably change as soon as more precise models are developed and understood. Atmospheric and ocean tide geocenter coefficients are already contained in the IGS (and CODE) products and therefore not further considered in this study.

2.3.6 Clustering and weekly combination

Due to the large number of stations (210) in the network, the network was divided into 10 clusters consisting of approximately 20 stations each (Figure 3). Each cluster is processed individually, following the strategy described before. Afterwards, the ten clusters for a day are combined in a daily solution for the complete network. In this case, station positions for all stations are constrained to 1 meter.

As the satellite orbits, Earth rotation parameters and satellite clocks errors were included as fixed parameters, these solutions are known as “loosely constrained solutions”. The geometry is however maintained with high precision. After the daily free normal equations are computed, the network is loosely constrained to 1 meter with respect to the available IGb08 station coordinates to provide the absolute coordinates.

To reduce the dispersion of the daily solutions and to identify outliers, the seven daily solutions corresponding to a GPS week are combined into one weekly solution. Quantitatively, the noise of the station position time-series of weekly solutions is reduced approximately by 20-30% with respect to the time-series based on the daily solutions.

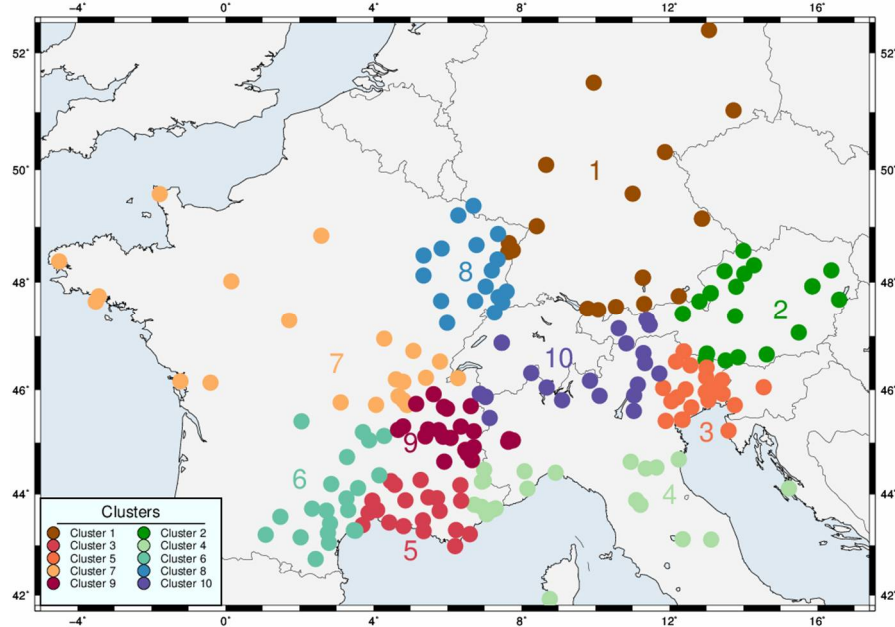


Figure 3. The allocated clusters (color-coded) for the processing of the large GNSS network.

The data processing is based on the least-squares adjustment approach. In a first step, the GNSS observations of one day and belonging to the same cluster are processed in one block. In a second step, the normal equations corresponding to each cluster are combined to generate a daily normal equation containing the entire network. This is possible as the results of a least-square adjustment (including all observations in one block) is the same as if the least-square estimation would be divided in different blocks, which are later combined on the normal equation level. This so-called *sequential least-square adjustment* is very useful, because it is performed at the normal equation level. It is independent of the observation types considered in the individual solutions and allows the handling of a large number of parameters. A detailed description about sequential least-square adjustment can be found, for instance, in Dach et al. (2015). The sequential least-squares adjustment is also applied to combine daily normal equations to weekly normal equations and weekly normal equations to multi-year solution.

Table 4 summarizes the additional external sources required for GNSS processing.

Table 4. Bernese project related file sources.

File	Source	Comments
PCV – phase center variation	ftp://ftp.unibe.ch/aiub/BSWUSER52/GEN/PCV_COD.108 original file is ftp://ftp.igs.org/pub/station/general/igs08.atx	Correction to the phase center variations at satellite and receiver antennas.
CRX – Satellite problem file	ftp://ftp.unibe.ch/aiub/REPRO_2013/BSWUSER52/GEN/	Satellite problem information (to exclude unhealthy satellites)

File	Source	Comments
BLQ – Ocean loading	FES2004 model. Generated at: http://holt.oso.chalmers.se/loading/	
EPH – Orbit ephemeris	ftp://ftp.unibe.ch/aiub/REPRO_2013/CODE/ and ftp://ftp.unibe.ch/aiub/CODE/	
ERP – Earth rotation parameters	ftp://ftp.unibe.ch/aiub/REPRO_2013/CODE/ and ftp://ftp.unibe.ch/aiub/CODE/	
DCB – Differential code biases	ftp://ftp.unibe.ch/aiub/CODE/	
ION – Ionosphere file	ftp://ftp.unibe.ch/aiub/CODE/	Biases between GPS and GLONASS code observations

2.4 Quality assessment of the processed GNSS data

The quality of the processed GNSS data depends on the processing strategy and on the GNSS observation itself. The network consists of baselines, which are formed by the Bernese GNSS software. As it is seen from the Figure 4, the network topology is a graph of a type *tree*. A set of stations is connected by the baselines in a ‘star-like’ group to the common ‘core’ station. The ‘cores’ of several groups are connected with each other by longer baselines. Thus, two arbitrary stations are connected only by a single path, so they have a linear dependency. The topology of the network (Figure 4) was constant over time, but varying from one daily solution to the next one. This is due to variation in number of available stations for a given epoch (Figure 2).

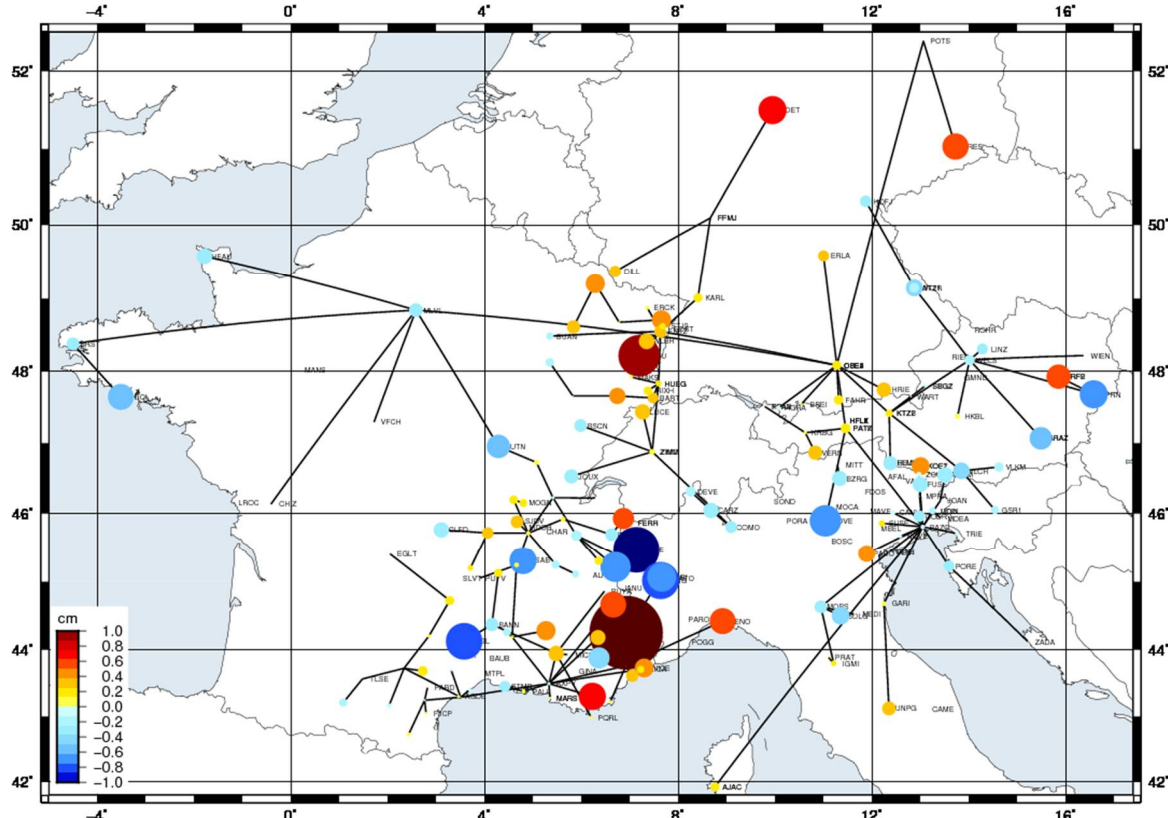


Figure 4. Example of the network topology for the specific day 2014/01/02 and color-coded vertical residuals of station position. Residuals are taken from the combined solution (see section 3.2).

The topology itself is strongly correlated with the estimated station position. The stations that contribute only to one baseline in general have larger residuals, than the ‘core’ stations. Moreover, stations on the shorter baselines have smaller residuals, than stations on longer baselines. For instance, for the arbitrary day 2014/01/02 (Figure 2), station ZIMM (Zimmerwald) present a smaller vertical residual of about 0.1 mm , while the other stations connected to the ZIMM by baselines have residuals larger than 0.2 mm .

Stations with large residuals (over 10 mm) tend to be included only one baseline. This is probably due to larger number of unresolved ambiguities and less precise determination of atmosphere parameters, than for stations that share larger number of baselines.

Figure 5 illustrates the statistics of resolved ambiguities for different ambiguity resolution schemes and systems (GPS, GLONASS and mixed). The sequence of the ambiguity resolution schemes is described in the section 2.3.1. As it can be seen in Figure 5, the percentage of resolved ambiguities was not constant over time. For most of the ambiguity resolution schemes using GPS signals (marked with letter G in Figure 5), the percentage of resolved ambiguities was decreasing with time. For the GLONASS percentage of resolved ambiguities on L5 and L3 has tendency to improve over time and saturates at approximately 80%. The significant drop in percent of resolved ambiguities in the middle of 2004 at QIF scheme for GPS is probably due to variations in the actual ionosphere parameters that cannot be handled by the a-priory model defined in the QIF strategy. Moreover, in a percentage of resolved ambiguities using QIF strategy for GPS, it is possible to observe the annual signal, with better ambiguity resolution in winter and worse in summer (the network is in the mid-latitudes in Northern hemisphere), revealing the influence of the ionosphere.

The plots are color-coded to account for the number of baselines. On the plots illustrating the ambiguity statistics for GLONASS (marked with letter R), it can be seen the gradual increase of the number of stations (and, therefore, the number of baselines) tracking GLONASS signals. Short baselines connecting stations with receivers capable of tracking GLONASS signals appear only since 2008. Thus, the Direct L12 ambiguity resolution statistics on GLONASS started from 2008.

The variation of the plots is also due to variability in the number of GNSS stations (Figure 2) and due to non-constant topology of the network (Figure 4) over the time.

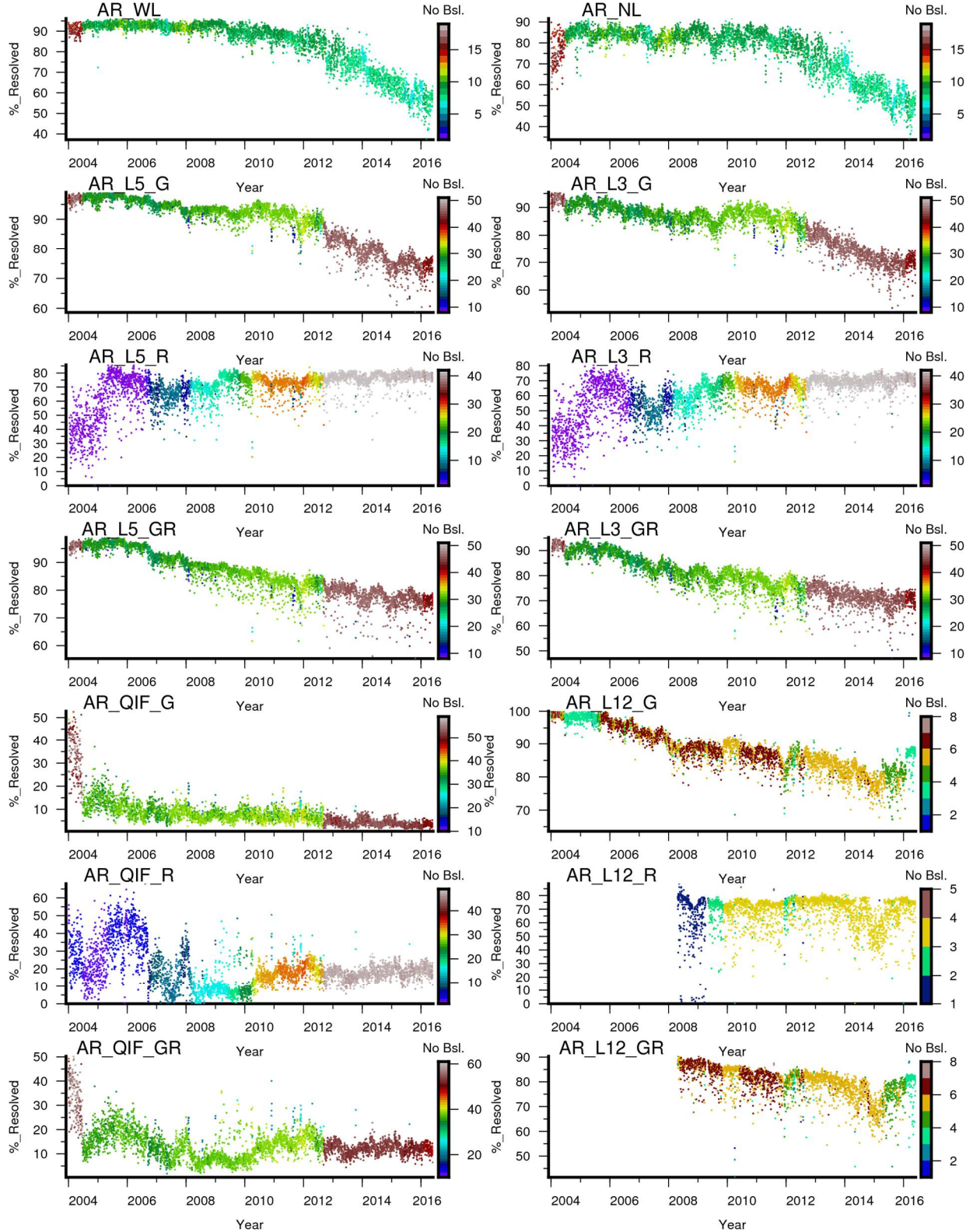


Figure 5. Statistics of ambiguity resolution. The x-axis denotes epoch. The y-axis denotes the percentage of resolved ambiguities. The number of baselines are color-coded, according to the colorbar. Ambiguities resolved on GPS or GLONASS are marked with letters G and R, respectively. GR stands for mixed (GPS and GLONASS) statistics.

3 The multi-year combination and analysis

The purpose of the multi-year combination in the current study is the estimation of precise velocities for the GNSS sites. The multi-year combination is performed with the Bernese software, by stacking the weekly free normal equations (NEQ).

According to this, the weekly normal equations obtained in the Chapter 2 are combined to a multi-year solution by extending the NEQ for the station velocities (as a constant linear motion). The normal equation combination is solved applying a minimum constraint condition with imposed Helmert transformation (translation and rotation only) condition to selected IGS reference stations. Translational constraints are imposed, so the origin ($x=y=z=0$) of the estimated coordinates coincides with the origin of the reference coordinates. Minimization of the rotation is usually applied to the global networks, but still applicable for the regional one. The scale factor was not used, since it is applied in rare cases, for instance, for the estimation of satellite antenna phase center offsets (Dach et al., 2015; Herring et al., 2010). The validity of the computed velocities relies on a station position time-series analysis and the evaluation of different strategies for the geodetic datum realization within the multi-year solution computation.

In practice, the multi-year combination is usually done iteratively, together with an analysis of the time-series for the position components. The flow chart diagram is illustrated in Figure 6. The purpose of iteration is the identification of discontinuities and outliers in station position time-series and further refinement of the multi-year combination.

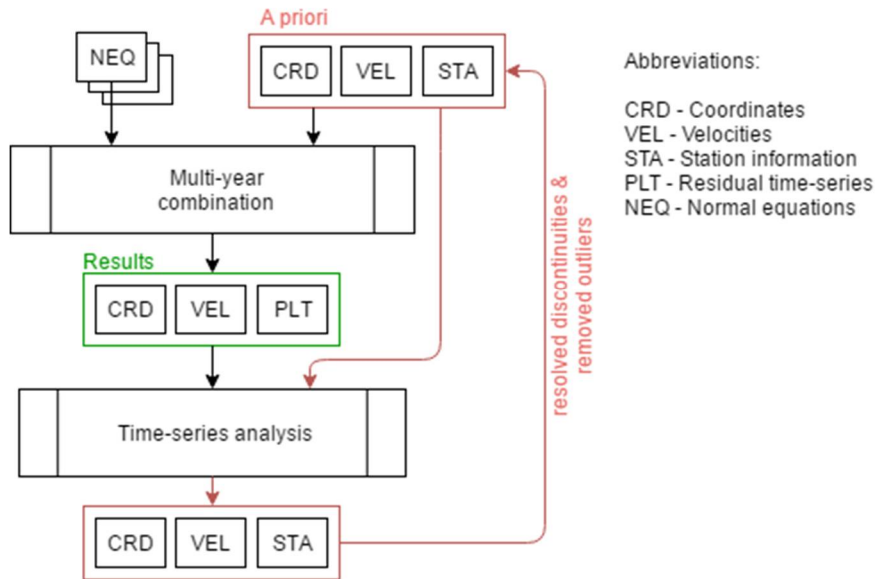


Figure 6. Flow chart diagram of the multi-year combination and time-series analysis. In red color outlined the loop of iterative refinement of stations set-up to resolve discontinuities and elimination of outliers. The station position and velocities (outlined by green box) are the results of a multi-year combination.

One of the important aspects of the multi-year combination is the datum definition. The details about datum definition are provided in the section 3.1 and the multi-year combination procedure is discussed in the section 3.2. The time-series analysis is covered in the section 3.2.1.

3.1 Datum definition

To estimate the station positions and velocities from the free normal equations, the geodetic datum shall be introduced. By the introduction of the datum, the internal precision of positions and velocities is usually degrading into external precision, because of inconsistencies in the position and velocity of the reference stations itself (Pelzer, 1985; Niemeier, 2008).

The datum definition of the network can be performed by several conditions: e.g.: minimum-constrained, constrained, free-network condition (used for test purpose only) and fixed (this datum definition type is not considered as useful for the multi-year combination and it is not further discussed). In the preliminary step, three different types of datum definition were applied in the multi-year combination for the purpose of selecting the most appropriate one (among minimum-constrain and constrained solutions).

The most practical datum definition is the minimum constraints condition. It minimizes the deformation in the network caused by constraining selected sites to a-priori known coordinate and velocity parameters. Under this constraint type, it is preferable to use reference stations with complete availability of GNSS observations for a given station during the 12.4 years of observations (in this study, the period between 2004/01/01 – 2016/05/30). Reference sites with short time-series may introduce some additional degree of freedom in the time-series trends of the stations (Figure 7). This additional trend was clearly found in time-series of the network and exactly during observations of that reference site with incomplete time-series. This effect happened because internal velocities of the reference stations in the network and external velocities (from external datum, IGb08 for example) do not match. Thus, this discrepancy is absorbed in the temporal deformation (wrong velocity) of the reference sites with the shortest time-series.

In Figure 7 misleading minimum constrained solution based on the IGS16P26 datum is illustrated. The discrepancies in the datum itself are seen in the Figure 18. For instance, station GRAZ (Graz) has relatively stable a-priori values of station velocities defined for each time interval between discontinuities (see Figure 18). Nevertheless, the estimated velocity for the first interval (2004-2006) differs from the other intervals (see Figure 7). Such discrepancy propagated to other station time-series. The time-series of station GRAS (Caussols) show the same effect. On the contrary, the discrepancy in a-priori velocity of station TLSE (Toulouse) (see Figure 18) is not revealed in its estimated time-series (Figure 7). This leads to conclude that the IGS16P26 datum is inconsistent.

The multi-year combination and analysis

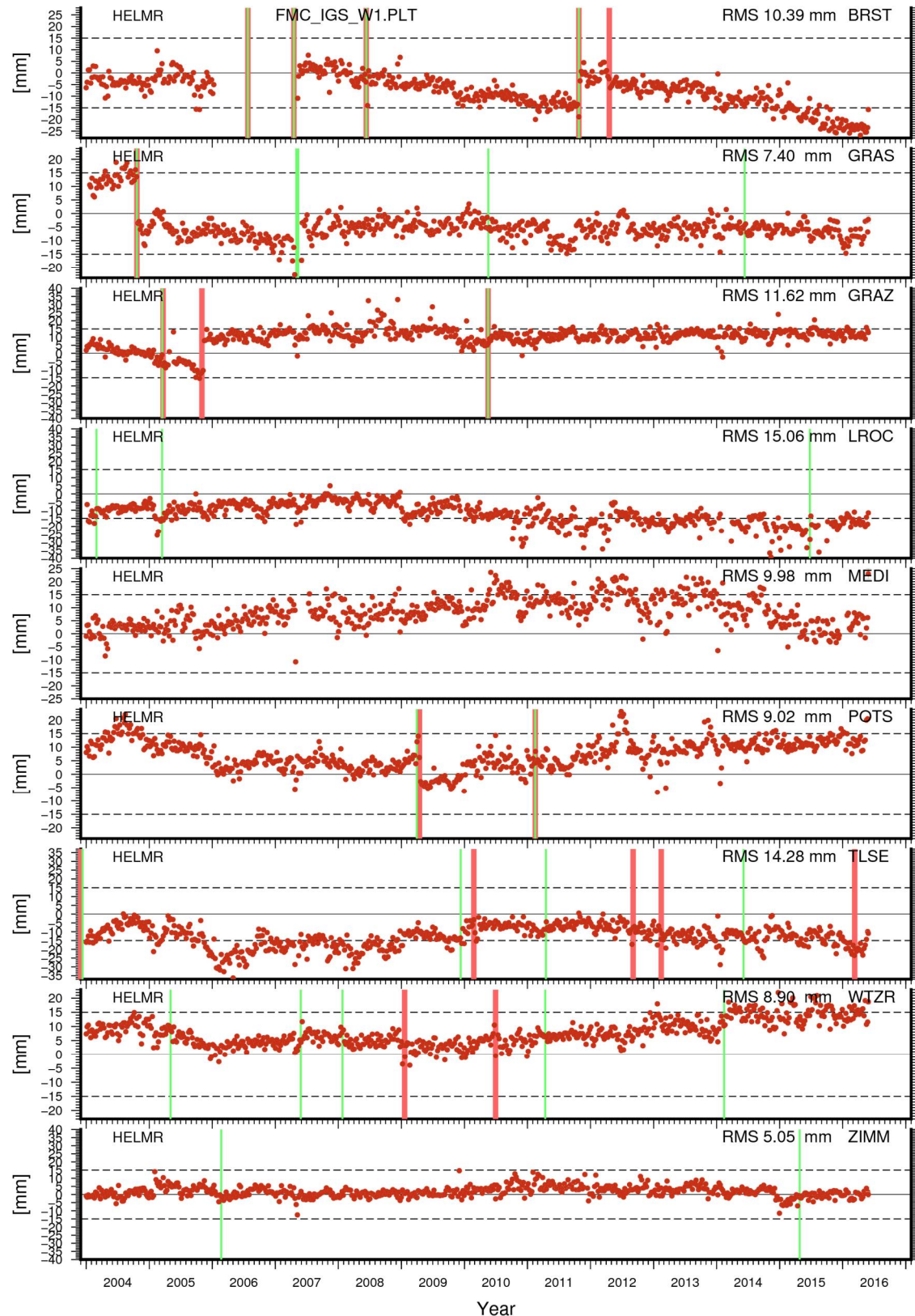


Figure 7. Example of miss-fit in the minimum constrained solution based on the IGS16P26 datum. Only the vertical component is shown. Green lines refer to the receiver change. Red lines refer to the antenna/radom change.

Another possible option for the datum definition is the constraint condition, when position and velocities of reference stations are constrained within some uncertainty. This option has a risk of over-constraining, when the pattern from the time-series of the reference stations propagate into the time-series of the other stations in the network. Usually, by over-constraining the reference sites, the systematic errors, (pattern, large-period like yearly variations) are very well visually identified in the time-series of neighboring stations (Figure 8). Quantitatively, the RMS of the time-series in network is enlarged by the over-constraining.

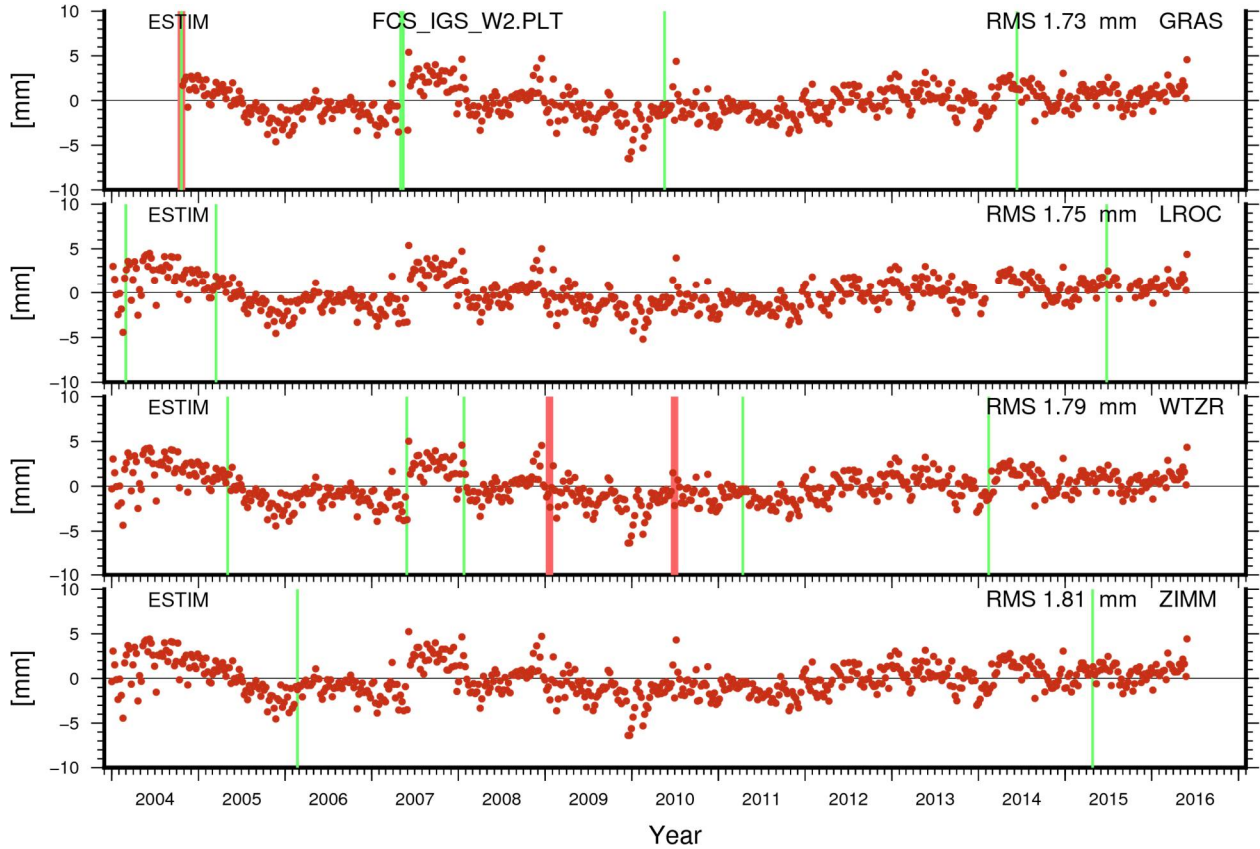


Figure 8. Example of an over-constrained solution. Time-series became look alike. Only the vertical component is shown. Green lines refer to the receiver change. Red lines refer to the antenna/random change.

The free-network condition is the unconstrained datum definition. It is constrained only to the satellite orbits. As result, it provides the least deformed network solution. Neither coordinates, nor velocities are meaningful, but the time-series of residuals itself are highly reliable. This datum type serves for test purposes only: it provides the time-series with lowest noise and allows checking time-series for problems of minimum constrained (Figure 7) or constrained solutions (Figure 8). However, it should be noted that the resulting station position and velocities obtained with free-network datum definition do not have practical use.

After testing the three different datum definition types, the minimum constrained condition was chosen for the multi-year combination.

3.2 Performing the combination

To provide the most accurate stations velocities, a set of IGb08 stations (i.e. WTZR, ZIMM, GRAS, GRAZ, MEDI and LROC) was selected as reference. Those stations were chosen as the most reliable in terms of low number of equipment changes and nearly complete coverage of the time-series along 2004.0-2016.4. In practice, if stations with incomplete time-series (e.g. BRST) or frequent equipment change (e.g. TLSE, POTS) are used as reference stations one may introduce disturbances into the network leading to discrepancies in the results. It reveals as an artificial slope in the temporal fraction of time-series of neighboring stations (Figure 7).

Those stations with an observation period of less than two years were excluded from the combination, since the convergence of the estimated velocity for a short observation interval (less than two years) is insufficient, due to the influence of seasonal signals. According to Brockmann et al. (2014) the formal error of the velocity determined from less than 5 years of continuous observations is more than 0.2 mm/a .

Performing the multi-year combination, station position time-series experience discontinuities due to equipment changes, earthquakes, landslides, etc. The time-series of each station revealing such discontinuities were split into a set of fragmented station time-series and their velocities were relatively constrained to each other, while positions for each period are not constrained (Figure 9). This is done to absorb the discontinuities in the time-series and to provide a single value of the station velocity for the complete observation period. Those piece-wise fractions of time-series are further designated as fragments or ‘artificial’ stations.

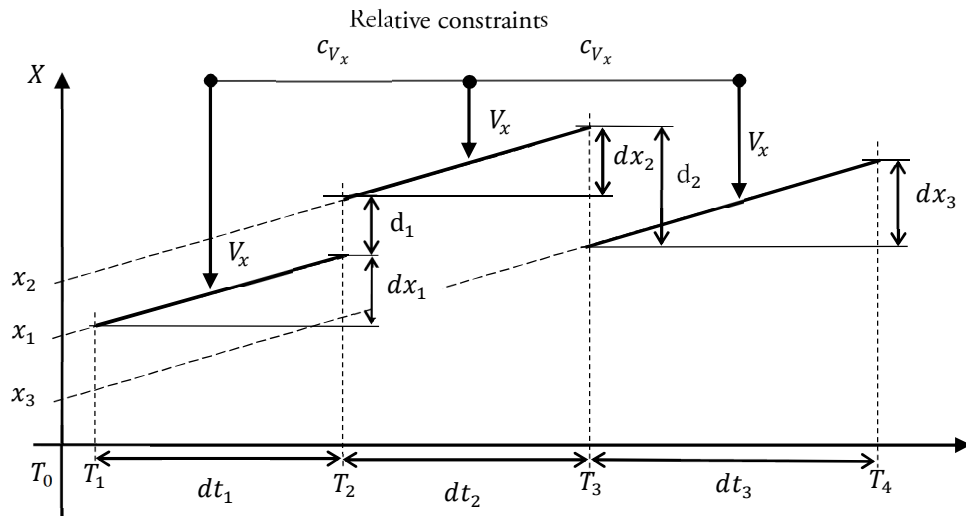


Figure 9. Schematic illustration of relatively constrained station velocity estimation. Velocities of piece-wise segments representing the fragments of station time-series are relatively constrained to each other.

The reasonable value for relative velocity constraints (between fragments of station time-series) is 10^{-6} m/a , while the smaller value like 10^{-5} m/a allows certain flexibility for velocity estimation in the sub-millimeter range, resulting in different velocities for different time intervals. To avoid different mean station velocities; it is convenient to constraint the velocities of the fragmented station time-series by one order of magnitude stronger than the default value.

For the reference stations, the coordinates and velocities are taken from the IGB08 reference frame (<ftp://igs-rf.ign.fr/pub/IGb08/IGb08.snx>). Even though that IGB08 provides officially solutions only for the period between 1994/01/01 – 2012/08/21, the velocities after 2012/08/21 were assumed to be unchanged and continuous. For the datum definition, the minimum constraint condition was chosen with the applied parameters shown in Table 5.

Table 5. Minimum constraints datum definition parameters.

	Component	Helmert transformation parameters
Position	Translation	10^{-7} m
	Rotation	10^{-7} mas
Velocity	Translation	10^{-9} m
	Rotation	10^{-9} mas

The continuity statistics of the original observations and after splitting (introducing the set of fragmented station time-series instead of original one) is illustrated in the Figure 10. This figure shows the histogram, there the bars corresponds to the length of observation interval. For instance, in this study 34 stations keep continuous records during 12 years. After splitting time-series at discontinuities, only 20 stations left, that keep 12 years of observations. Due to such splitting, the average observation interval shortens from 7-8 years to 4-5 years.

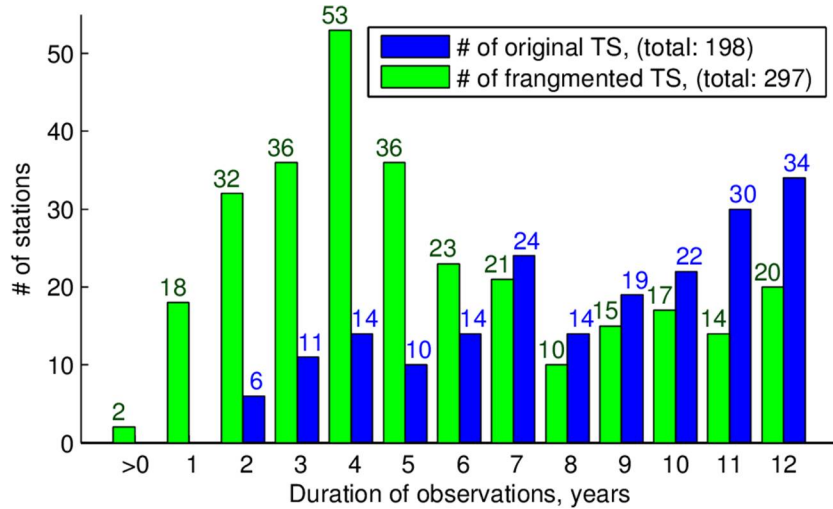


Figure 10. The histogram of the observation continuity. The blue color bars represent the number of original stations and green bars represents the fragmented station time-series (split due to discontinuities) per certain duration.

3.2.1 Time-series analysis

After computing the multi-year solution, the time-series were checked to identify discontinuities, outliers, velocity changes and periodic motion. The functional model of time-series analysis is the following (Ostini et al., 2008; Dach et al., 2015, pp. 274-275):

$$\begin{aligned} \mathbf{f}(t_i) = & \mathbf{d}_0(t_0) + \mathbf{v}_0(t_i - t_0) \\ & + \sum_{k=1}^{n_d} \mathbf{d}_k \eta_{d,k}(t_i) + \sum_{k=1}^{n_s} \mathbf{s}_k \eta_{s,k}(t_i) + \sum_{k=1}^{n_v} \mathbf{v}_k(t_i - t_k) \eta_{v,k}(t_i) \\ & + \sum_{k=1}^{n_p} [\mathbf{p}_{a,k} \cos(w_k(t_i - t_0)) + \mathbf{p}_{b,k} \sin(w_k(t_i - t_0))] \eta_{p,k}(t_i) \end{aligned} \quad (1)$$

where $i = 1, \dots, N$ – is the index of epoch t_i of the series of N elements;
 \mathbf{d}_0 and \mathbf{v}_0 – are the initial position and velocity;
 $\eta_{d,k}(t_i), \eta_{s,k}(t_i), \eta_{v,k}(t_i)$ and $\eta_{p,k}(t_i)$ – are the functions returning either 0 or 1 to indicate the validity of the related component;
 \mathbf{d}_k – is the list of η_d discontinuities;
 \mathbf{s}_k – is the list of η_s outliers;
 $\mathbf{v}_k(t_i - t_k)$ – is the list of η_v velocity changes;
 $\mathbf{p}_{a,k}, \mathbf{p}_{b,k}$ – are the phase and out-of-phase components for the η_p periodic functions.

To remove the seasonal (i.e. annual and semiannual) signals from the time-series and to screen for discontinuities, outliers and velocity changes, the following thresholds (Table 6) were used for the functional model eq. (1). The station position time-series were screened independently from each other, but the all three components of the time-series (North, East and Up) for each station were estimated together at once, using the full covariance from the SINEX file.

Table 6. Setup of thresholds for time-series screening.

Component	Horizontal	Vertical	3D
Discontinuities, m	0.05	0.05	0.07
Velocity changes, m/a	0.01	0.01	0.01
Outliers, m	0.015	0.03	0.03
Amplitude of periodic functions (annual and semiannual), m	0.0001	0.0001	0.0001

After performing the multi-year combination, several stations (e.g. CLAP, ACCE, PATK, PAT2, SOND) have velocities that deviate from the velocities of the stations located in the neighborhood. Most of them were located on slowly moving landslides, contaminating the tectonic signal.

The station position times-series are often affected by seasonal signals (e.g. station KARL, illustrated in the Figure 11). This type of motion is relatively easy to determine using the periodic functions. While some stations may experience more complex motion, like landslides, earthquakes, silent earthquakes (e.g. station CANV in the Figure 12), etc. Those types of motion usually trigger a displacement of the station or sometimes even a velocity change (e.g. station BOLG, in the Figure 13). As the consequence, this effects have a negative influence on estimation of station velocities.

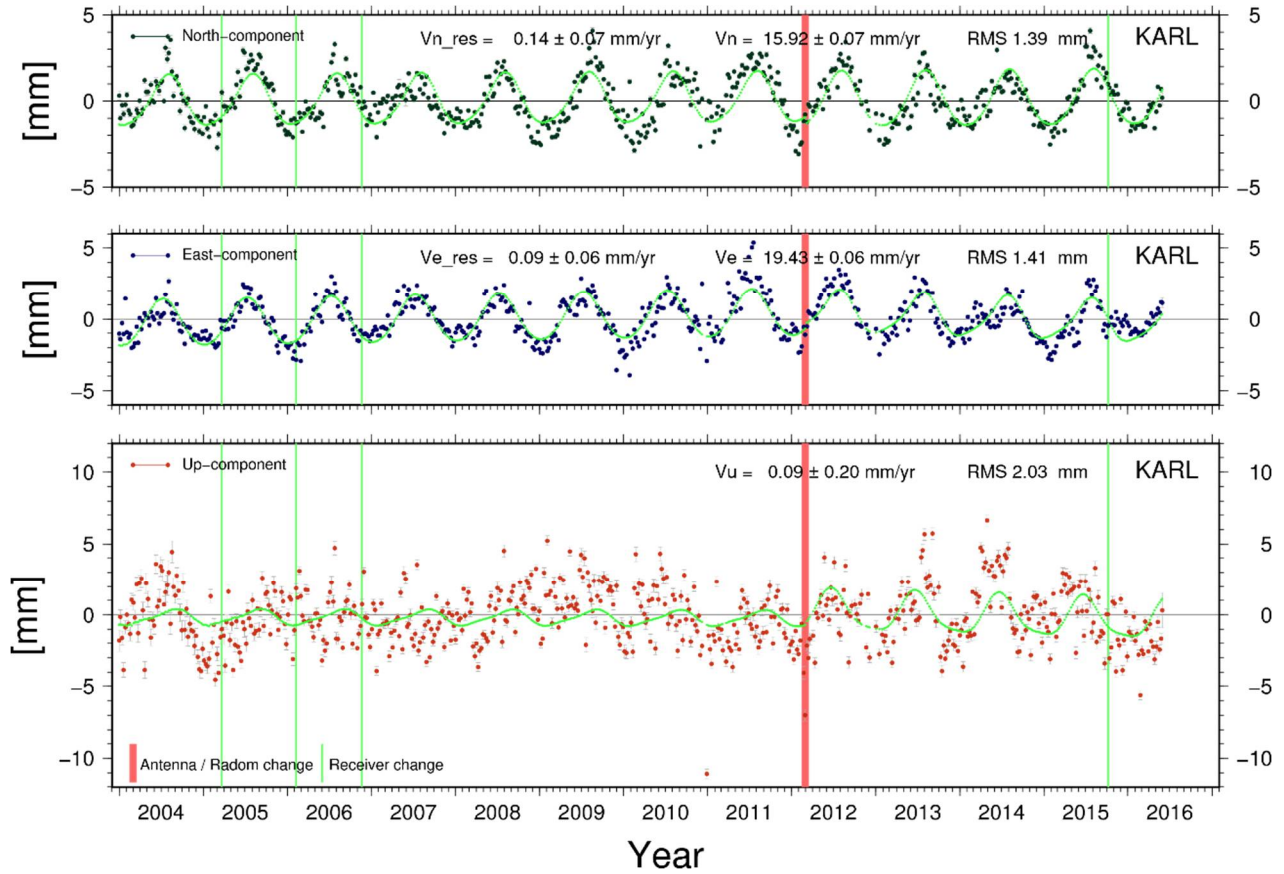


Figure 11. Time-series of position residuals for station KALR (Karlsruhe). In the North and East components, the annual signal is well-observed. Equipment change seems to be not affecting the time-series.

The multi-year combination and analysis

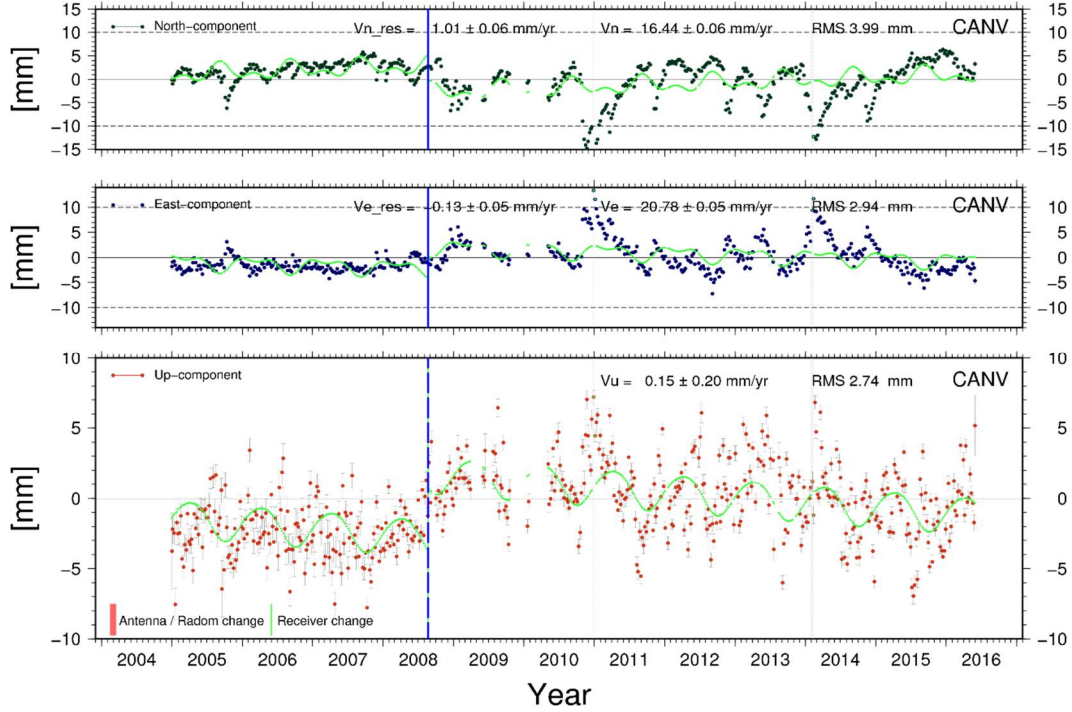


Figure 12. Station CANV (Caneva) experience the silent earthquakes. Station is located in the south of Italian Alps, in the seismic region. Blue vertical lines refer to a probable discontinuity, which happened after a receiver change.

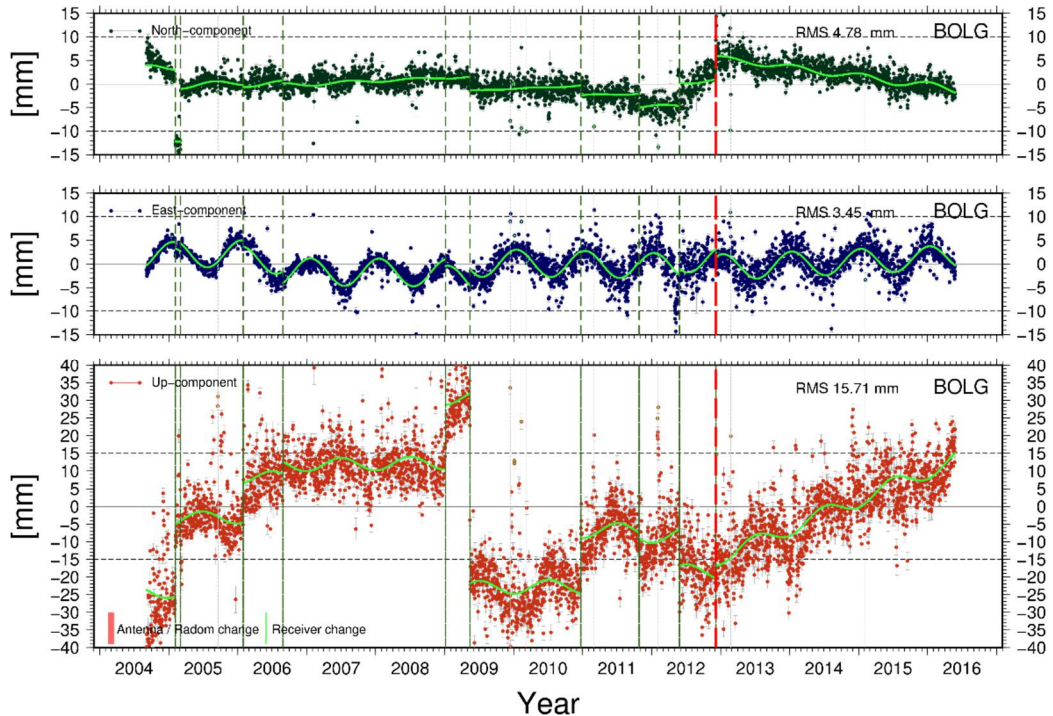


Figure 13. Time-series for station BOLG (Bologna). This is an example of station that frequently affected by the earthquakes. Station BOLG maintains the same equipment set up during the observation period. Red line denotes the time of a velocity change and green dashed line denotes discontinuities. Due to strong non-linearity, this station was excluded from the final multi-year combination.

Figure 14 illustrates the daily solutions combined in the preliminary multi-year combination for the reference station WTZR (Wettzell). There the discontinuities are not yet resolved. The RMS is approximately 1.5-1.9 mm for the horizontal components and around 3.8 mm for the vertical one. The green piece-wise sinusoidal time-series is the functional model, revealing the contribution of the seasonal signal and the discontinuities. Figure 15 illustrates the time-series after the final multi-year combination obtained from the weekly solutions for the same station. Here, the RMS is improved, approximately 0.7 mm for the horizontal and 2 mm for the vertical components. The discontinuity after the receiver change (e.g. in 2007) is more notable. Since WTZR is a reference station, it was constrained to the a-priori defined set of positions and velocities (i.e. to the IGb08 frame). Hence, its time-series may reveal a remaining trend in the position time-series.

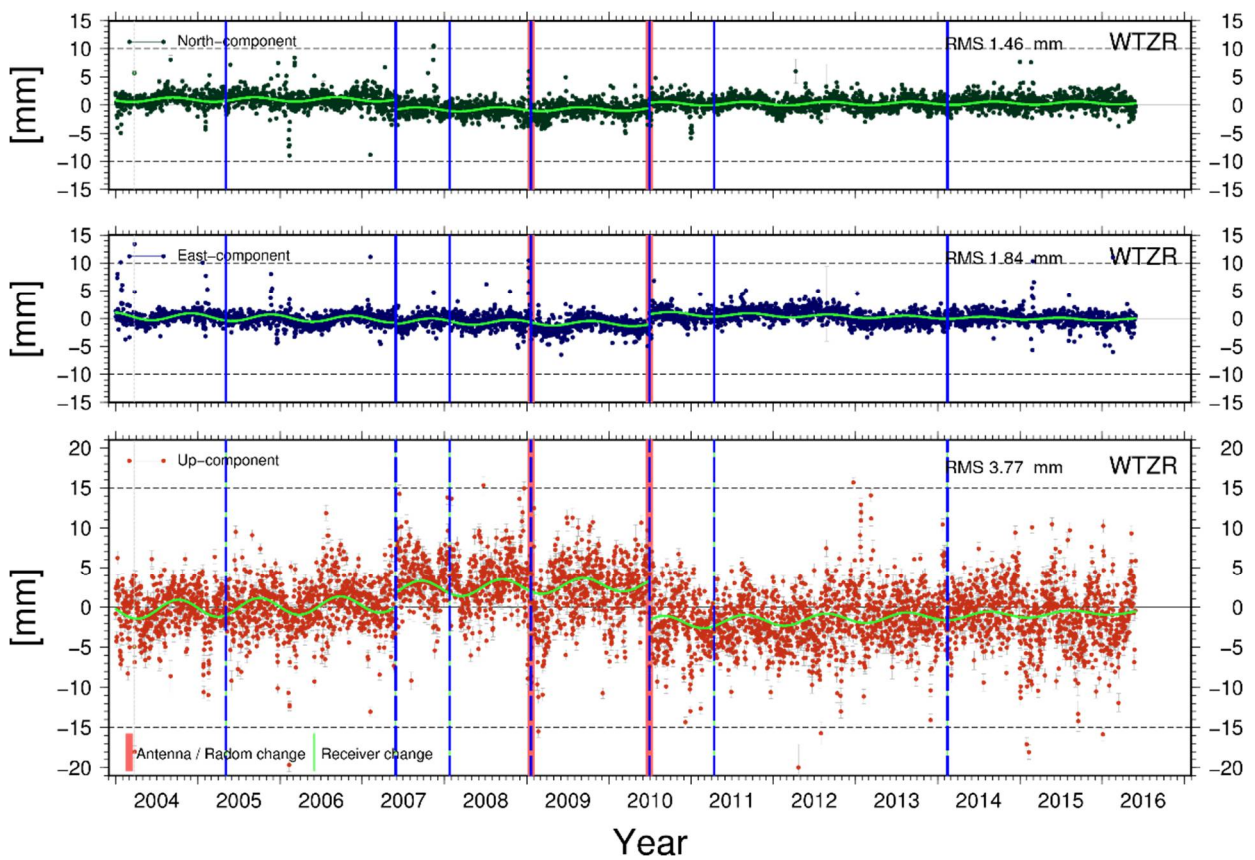


Figure 14. Example of residual positon time-series for the reference station WTZR (Wettzell). The daily residuals, single set of reference positions and velocities are used (IGb08_R datum). Offsets are observed in 2010. Green piece-wise sinusoidal time-series is the functional model.

The multi-year combination and analysis

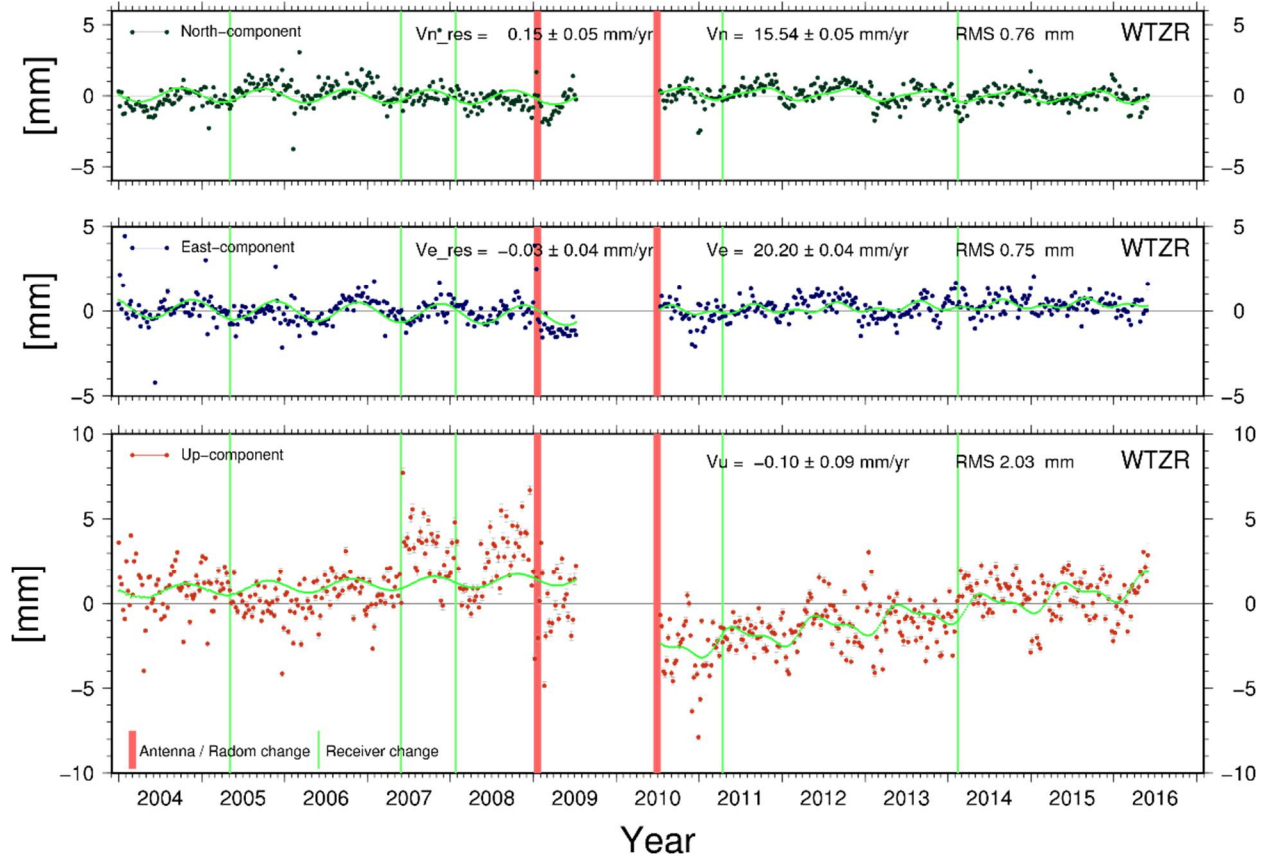


Figure 15. Weekly position residuals of station WTZR (Wettzell). Time-series are comprised of two fragments with individually coordinates and common velocities (e.g. IGB08 datum). Offsets after antenna changes remain. Several offsets after receiver change became more pronounced.

After the determination of the discontinuities in the station position time-series, the total (from East, North and Up components) RMS of station position residual time-series is illustrated in Figure 16. Here, the seasonal signals were preserved in the station position time-series. The average RMS for the entire network in the East and North components is nearly 1 mm, while in the Up component is approximately 2.5 mm and the total is 3 mm (Figure 16). A few stations has larger RMS of station position residuals in the order of 5-7 mm. This is mainly due to pronounced annual signals (e.g. AFAL, AUBU, FERH, OGAG, WIEN, even for station KALR (see Figure 11) or due to silent earthquakes (e.g. CANV, time-series illustrated in Figure 12).

As it can be seen from the Figure 16, stations located in the mountains tend to have a larger RMS of time-series. This could be explained by the frequent seismicity. The snow accumulated on the antenna leads to elevated station position estimate (e.g. AUBU).

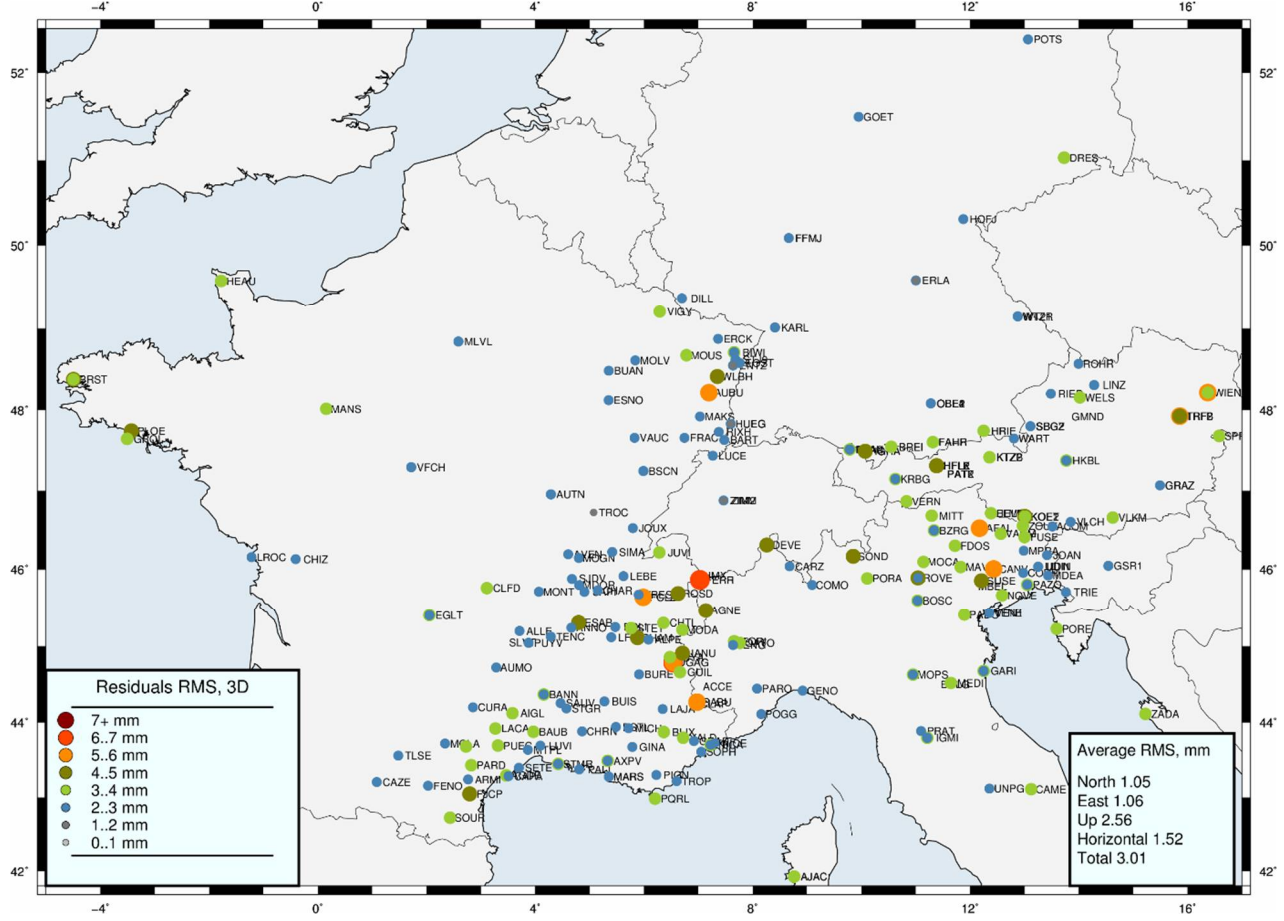


Figure 16. RMS of the station position residual time-series after resolving discontinuities. For the computation of RMS values, the seasonal signals were preserved.

3.2.2 Test of the datum definition

After performing the multi-year combination, its consistency was checked by testing the datum definition. Using the Helmert transformation, the weekly solutions are compared with respect to the multi-year solution (Figure 17). This procedure is used for the identification of problem epochs and stations, which should not contribute to the multi-year solution.

The Helmert translation transformation are provided in a 3D Cartesian system (XYZ frame). The XYZ residuals are transformed into a local topocentric ENU frame (East, North and Up components), assuming the center of the local network at the position 46°N latitude and 8°E longitude. In Figure 17, it can be seen that the vertical translation component has a variability approximately twice larger than the horizontal components.

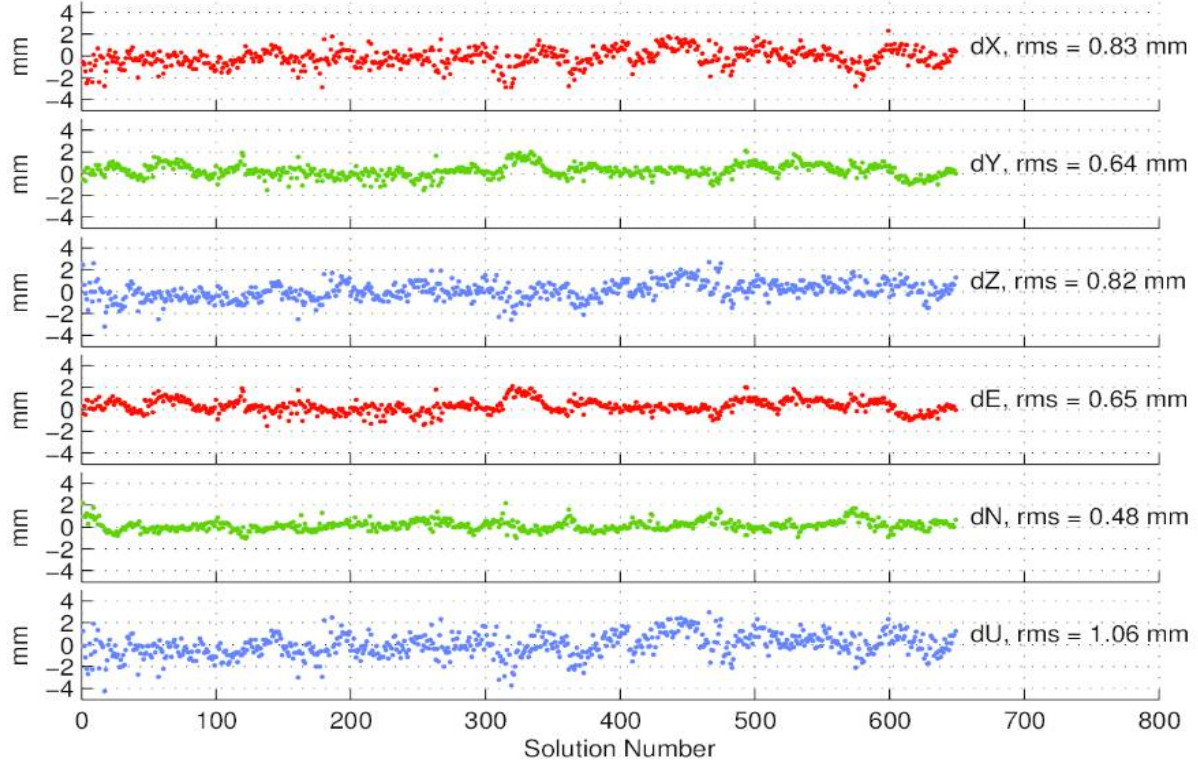


Figure 17. Helmert translation transformation parameters between weekly solutions and the multi-year solution. The shift in local ENU frame obtained assuming a local topocentric coordinate system at the position 46°N and 8°E.

3.2.3 Datums effect on the station velocities

The datum effect is a disturbance that propagates into the network due to inconsistencies of the reference station positions and/or velocities. For verification, three sets of reference coordinates and velocities were used for the datum definition (Table 7) and the results are compared with each other (Figure 19). The global GNSS network solutions (e.g. IGS/IGb) may contain velocity outliers, which can only be identified in the scope of local or regional networks.

Table 7. Multi-year solutions and datum definition sources.

Case	Solution	Datum source	Short notation in this text
1	FMC_IGB_W7	ftp://igs-rf.ign.fr/pub/IGb08/IGb08.snx	IGB, IGb08
2	FMC_IGS_W5	ftp://igs-rf.ign.fr/pub/1903/IGS16P26.snx.Z	IGS
3	FMC_EPN_W1	ftp://epncc.oma.be/pub/station/coord/EPN/EPN_A_Igb08.SNX.Z	EPN/EUREF

All three solutions were obtained using the minimum constrained condition datum definition type.

The largest variations of stations velocities are observed between the datum definition based on the EPN (case 3) and the datum definition based on the IGS (case 2) networks (see stations ZOUF and UNPG in the Figure 18). The datum IGS16P26 cumulative solution shows the instability in velocities, this is most likely, that the velocities were not tightly relatively constrained and/or some of the large discontinuities were not resolved.

The IGb08 stations GRAS, GRAZ, LROC, MEDI, WTZR and ZIMM are included in the three reference coordinate sets used for the datum definition (Table 7), and they are applied for set up of the minimum constrained condition. It should be mentioned that station MEDI is not included in the EPN coordinate set.

For all three datums, there were common stations: GRAS, GRAZ, LROC, MEDI (not included into the EPN), WTZR and ZIMM. Those are the only six out of nine IGb08 stations in the network. For datum definition type is chosen the minimum constraint condition.

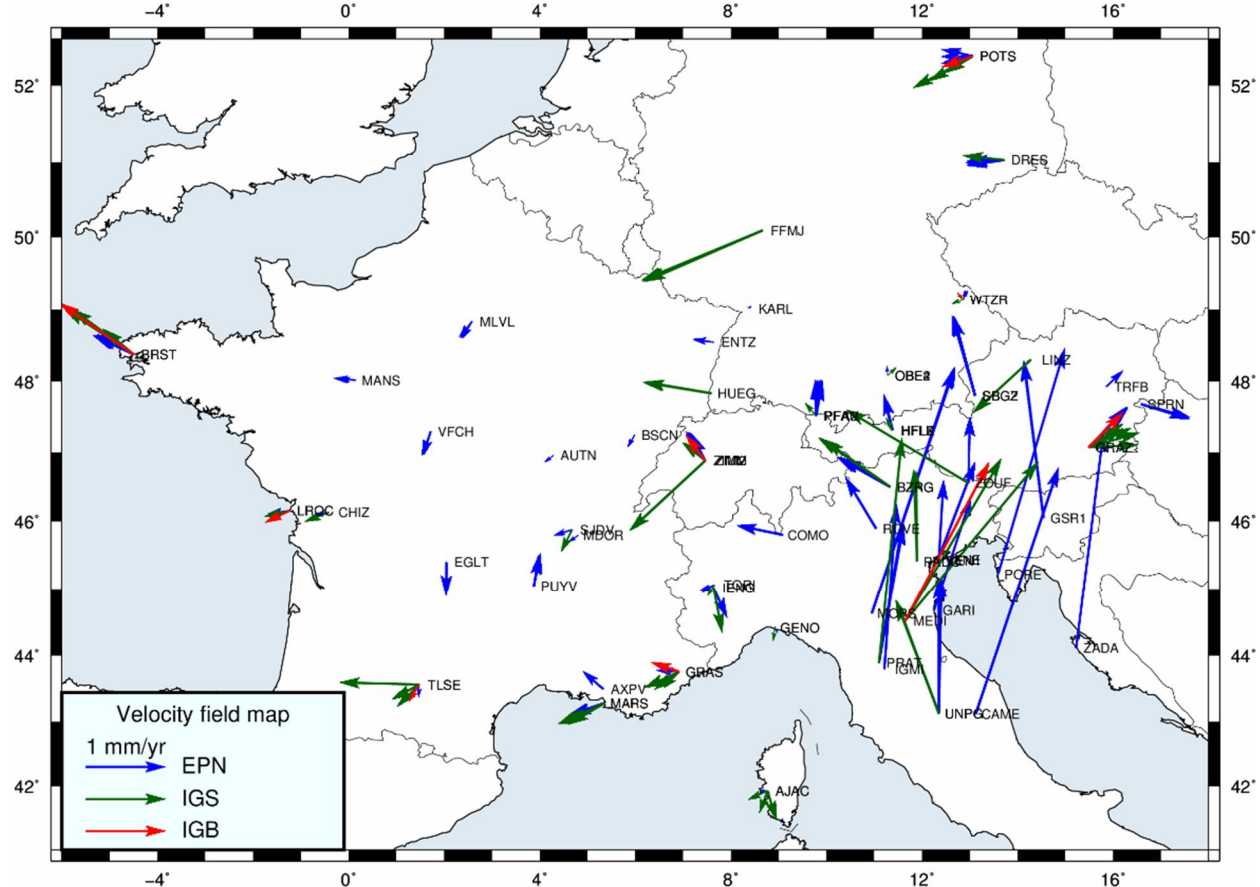


Figure 18. Comparison of reference station velocities included in the three different sources: IGb08, IGS16P26 and EPN

For instance, the difference in the velocities of the entire network due to different datums IGb08 (case 1) and EPN (case 3) is provided in the Figure 19. It is possible to conclude, that the datum effect on the network has a feature of uniform velocity and/or coordinates bias over the entire network.

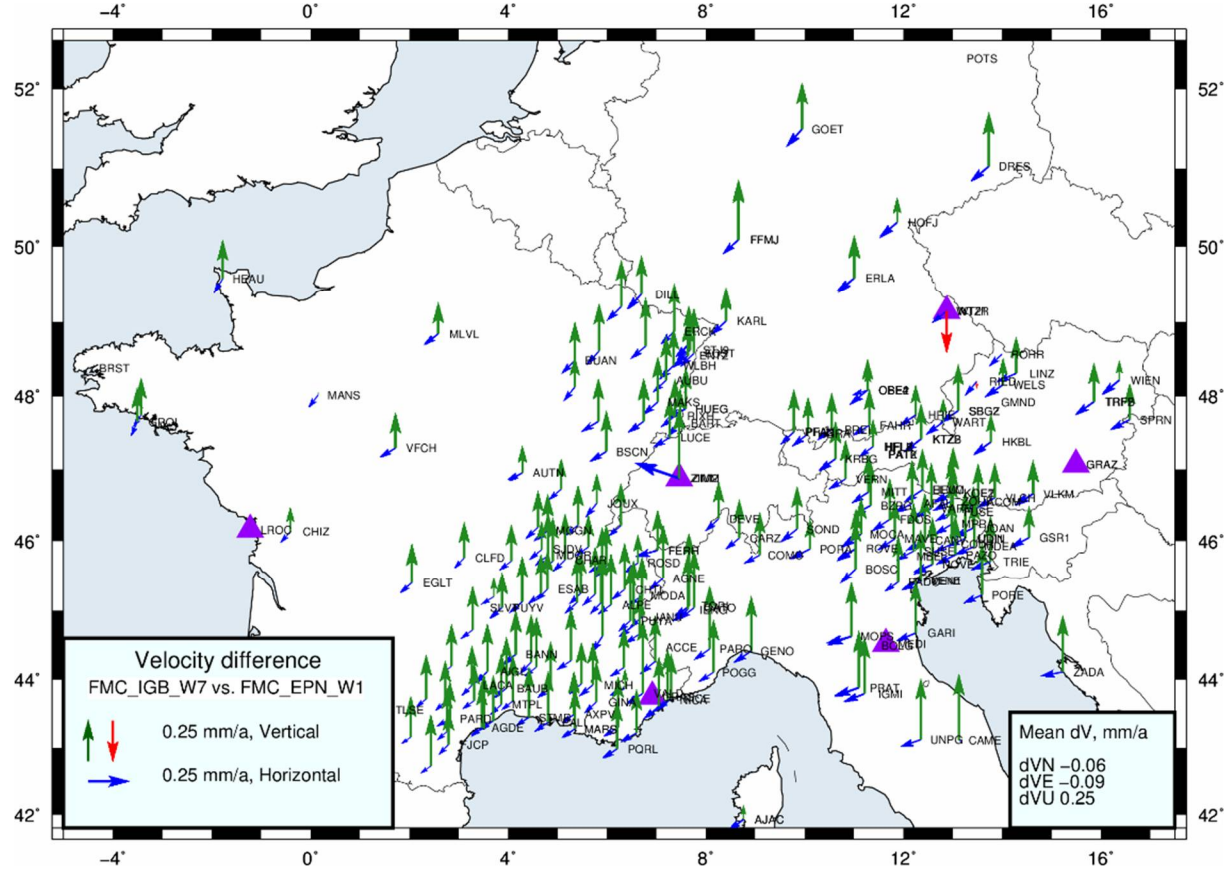


Figure 19. Datum effect on the stations velocities, comparison between IGB08 and EPN datums.

Table 8 provides the comparison of the a-priori station position and velocities for reference stations and a-posteriori station positions and velocities for the entire network. Comparing the solutions with different datum realizations with each other, a small variation in sub-millimeter level is observed. The largest variation of velocity is in the vertical component, which is the most difficult to be determined.

Table 8. Average differences between solutions based on different datums.

Comparison between solutions based on datums	Mean position difference, mm						Mean velocity difference, mm/a					
	For reference sites ¹			For entire network			For reference sites ¹			For entire network		
	dN	dE	dU	dN	dE	dU	dVn	dVe	dVu	dVn	dVe	dVu
IGb08 - IGS61P26	-0.32	0.29	1.00	0.75	-0.19	1.29	-0.08	0.11	0.21	0.11	-0.04	0.23
IGS16P26 - EPN	-0.17	-0.34	-0.71	-0.89	-0.63	-1.77	-0.05	-0.17	-0.13	-0.18	-0.05	0.02
EPN - IGb08	0.25	-0.07	-0.22	0.13	0.83	0.48	0.06	0.03	-0.09	0.06	0.09	-0.25

¹Reference stations: GRAS, GRAZ, LROC, MEDI, WTZR and ZIMM.

Station coordinates are defined for the epoch 2010.0.

Even the solution with applied IGB08 datum differs from the IGS16P26 or EPN solutions; the IGB08 datum is assumed as the most accurate and consistent, since this is the refinement of an IGS08 frame. The IGB08 datum was selected as the most appropriate and the multi-year solution based on it was further used for estimation of the surface-deformation model.

4 Horizontal and vertical velocity fields

The final station positions and velocities computed in the multi-year solution refer to the IGB08, epoch 2010. It includes 198 stations with 297 occupations (due to discontinuities summarized in the Annex B). The estimated velocities represent the superimposed plate motion together with the crustal deformation and possible local effects.

The Alpine region is characterized by complex tectonic settings composed of the collision of the Eurasian plate with a system of Mediterranean microplates (i.e. the Pannonian, Adriatic and Liguria plates) (Brückle et al., 2014; Cuffaro et al., 2010). For the European region, the Eurasian plate moves with approximately 26 mm/a in northeastward direction. Most of the tectonic processes in the Mediterranean are related to the kinematics of the Adriatic block (Serpelloni et al., 2005; Heidbach and Drewes, 2003), forming the mountains belts around it: the Alps, Apennines and Dinarides (Figure 20).

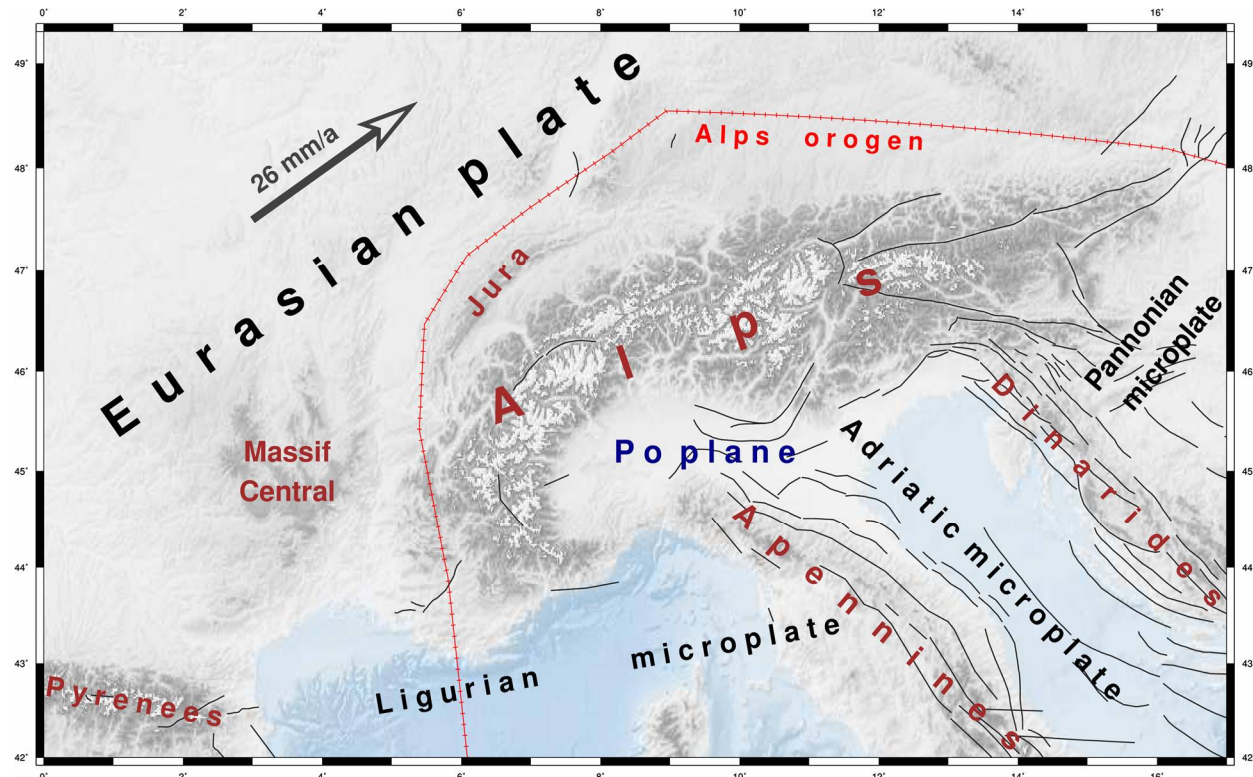


Figure 20. Tectonics of the Alpine region with their plates (i.e. Eurasian, Pannonian, Adriatic and Liguria). The red line represents the Alpine orogen (Bird, 2003). Black lines are the tectonic faults (Source: <http://diss.rm.ingv.it/share-edsf/>).

The topography is taken from the ETOPO1 model (Amante and Eakins, 2009. Source:

<https://www.ngdc.noaa.gov/mgg/global/global.html>.

Figure 20 illustrates a simplified picture of the tectonic settings in the Alpine region. The Eurasian plate is sharing the boundary with the Pannonian, Adriatic and Ligurian microplates. The tectonic fault lines and topographic features outline approximately the boundaries between tectonic microplates

and the Eurasian plate. The Adriatic microplate colliding with the Ligurian microplate forms the Apennines mountain ridge. Similarly, the collision of the Adriatic microplate with the Pannonian one forms the Dinarides. The Adriatic micro-plate moves northward towards the Alpine mountain range (Brückl and Hammer, 2014). The Po plane, located in the northern part of the Adriatic microplate, sharpens the southern boundary of the Alps. The extrusion of the Eastern Alps (the Austrian region) presents several tectonic interpretations and collected geophysical data are not sufficient to determine the plate boundaries unambiguously (Brückl and Hammer, 2014).

The boundaries of the Adriatic microplate with the Eurasian and Pannonian plates are seismically active, causing frequent earthquakes. In the Alps, the seismic release is well observed in southeastern part and a notable crustal deformation is determined in the western part, in the Austrian and Italian regions, (Serpelloni et al., 2005).

The velocity field in Figure 21 illustrates the dominance of the Eurasian plate motion. Therefore, it is barely possible to distinguish the intraplate motion or possible deformation in the microplates. Consequentially, the dominant signal should be removed and the deformation modeling should be based on the remaining signal (see Figure 29, section 4.3).

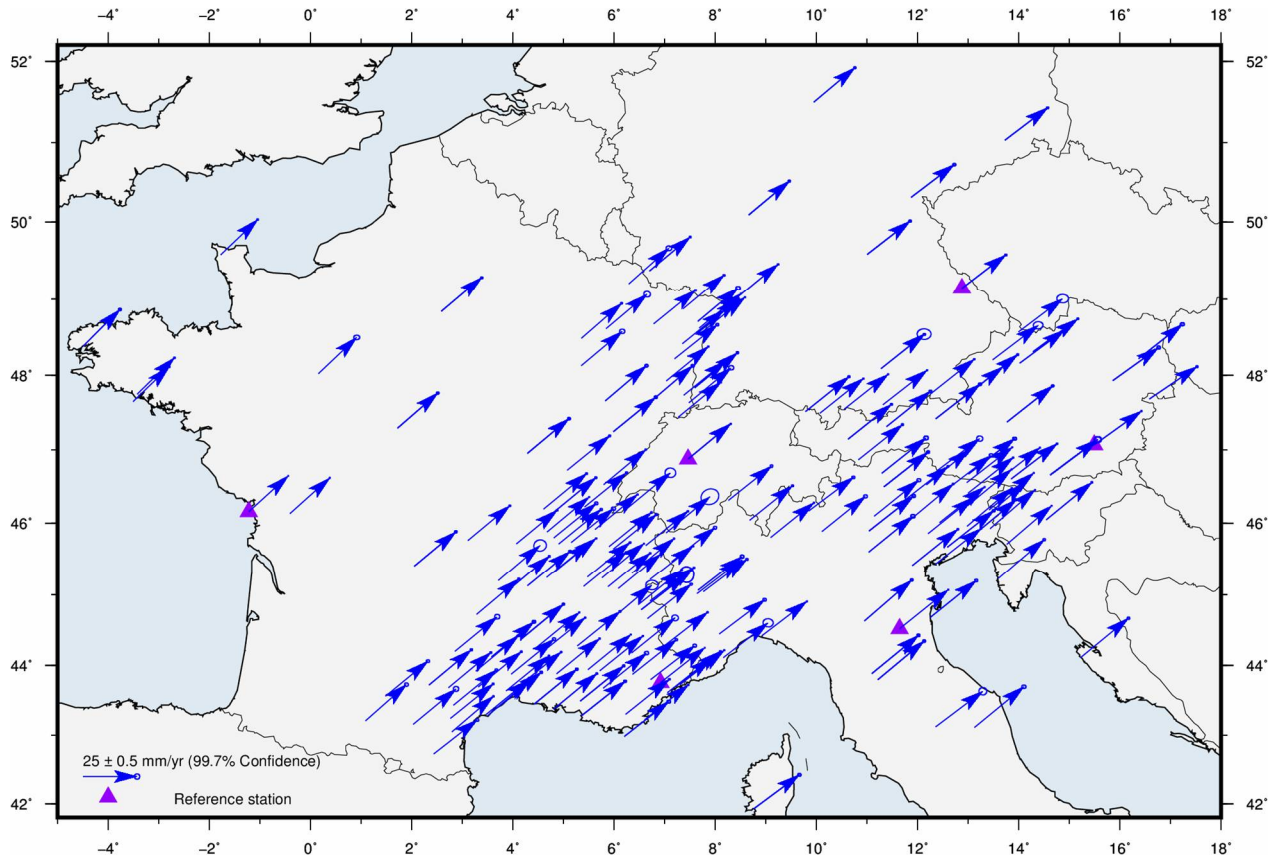


Figure 21. Horizontal velocity field. It is strongly correlated with the Eurasian plate motion. The formal errors of estimated station velocities are the rescaled.

The vertical velocity field (Figure 22) shows the uplift in the Alpine region. The Western Alps have an uplift rate of approximately 2.5 mm/a , while the Eastern Alps (Austrian region) show a slower vertical uplift rate of about $1.0\text{-}1.5 \text{ mm/a}$. At the coastal areas in Italy (near Venice) and in France (near Marseille) local subsidence zones are observed, the sinking rate is approximately -1.0 mm/a . The velocity of stations located at the stable part of the plate shows mostly local effects. The detailed description of the vertical velocity field along with the deformation field is provided in the Chapter 7.

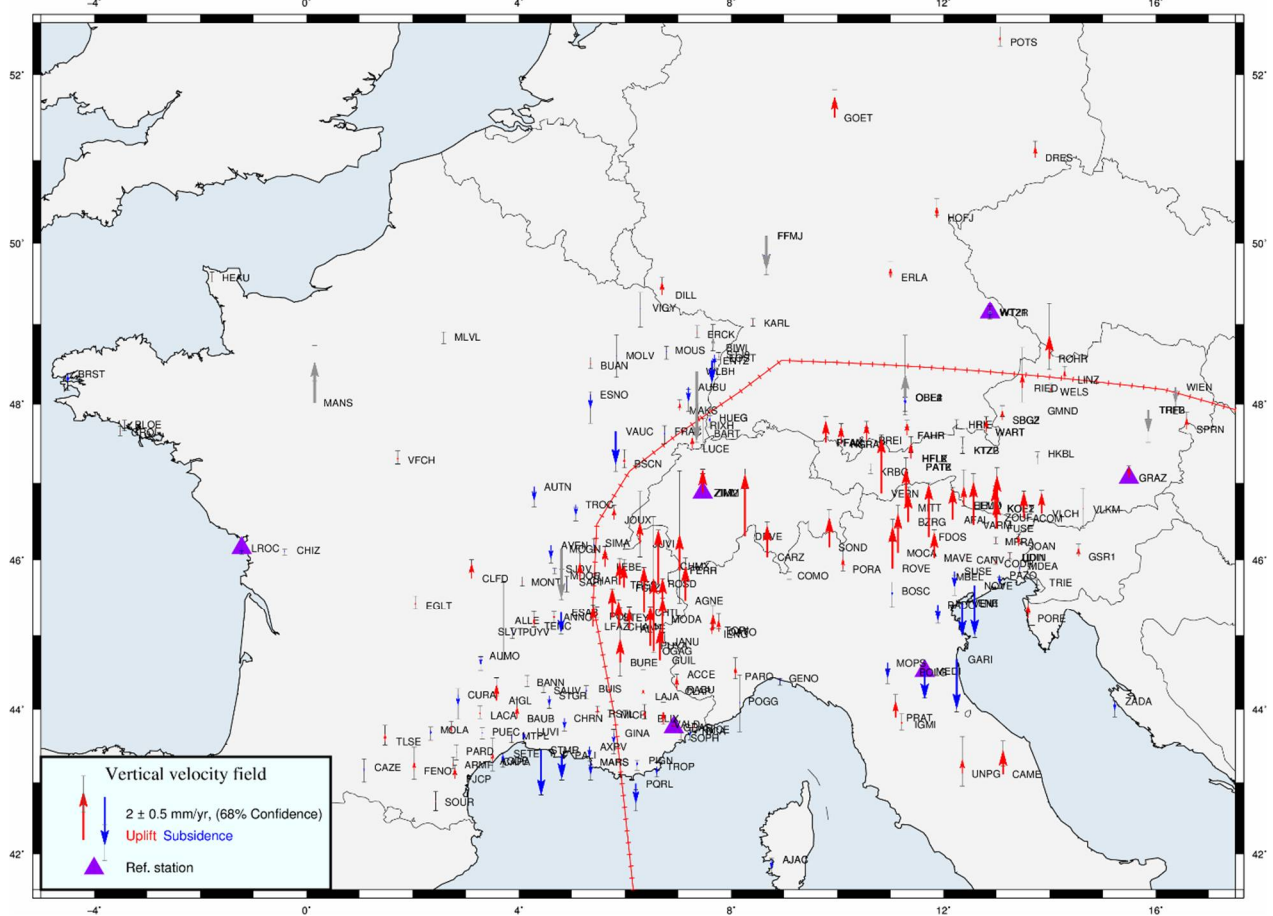


Figure 22. Vertical velocity field in the Alpine region. The red arrows represent uplift, while blue arrows represent subsidence. The error bars are taken from the covariance matrix of the SINEX file and scaled by factor of 17. The gray arrows are the outliers. The reference stations used for the datum definition are depicted by the triangles. The Alpine orogen (Bird, 2003) is outlined by the red curve.

4.1 Estimation of velocity uncertainties

The formal errors of the velocities estimated by the sequential least-square adjustment are generally too optimistic. This might have several causes. The degree of freedom is extremely large and the stochastics are possibly not correctly modeled. Correlations between the GNSS observations are not-well known and thus not considered. In order to assess realistic standard deviations for station positions and velocities, the standard deviation inferred from the station position time-series is used

to derive a scale factor for the formal errors produced by the least-square adjustment. In this study, the standard deviation of the station position time-series is computed and compared with the standard deviation contained in the covariance matrix (i.e. SINEX file), which is obtained in the multi-year solution. Based on this comparison, an empirical scale factor is estimated and then applied to the elements of the covariance matrix.

The experiment was performed using residual time-series and the standard deviation of coordinates from the SINEX file. The covariance matrix of estimates in the SINEX file is provided in Cartesian XYZ components. As it is convenient to present the uncertainty values in the ENU, the law of covariance propagation (eq. (2)) is applied.

The law of covariance propagation for transformation from Cartesian coordinate system to the local ENU system is defined as follows (Soler and Chin, 1985):

$$C_{enu} = RC_{xyz}R^T \quad (2)$$

where the covariance matrixes are:

$$C_{xyz} = \begin{bmatrix} \sigma_{xx}^2 & \sigma_{xy} & \sigma_{xz} \\ \sigma_{xy} & \sigma_{yy}^2 & \sigma_{yz} \\ \sigma_{xz} & \sigma_{yz} & \sigma_{zz}^2 \end{bmatrix} - \text{Covariance matrix in Cartesian coordinate system,} \quad (3)$$

$$C_{enu} = \begin{bmatrix} \sigma_{ee}^2 & \sigma_{en} & \sigma_{eu} \\ \sigma_{en} & \sigma_{nn}^2 & \sigma_{nu} \\ \sigma_{eu} & \sigma_{nu} & \sigma_{uu}^2 \end{bmatrix} - \text{Covariance matrix in local ENU coordinate system,} \quad (4)$$

and the transformation matrix R is:

$$R = \begin{bmatrix} -\sin\lambda & \cos\lambda & 0 \\ -\sin\varphi \cos\lambda & -\sin\varphi \cos\lambda & \cos\varphi \\ \cos\varphi \cos\lambda & \cos\varphi \sin\lambda & \sin\varphi \end{bmatrix}, \quad (5)$$

where φ – is the latitude of a station;

λ – is the longitude of a station.

Here it should be stated that in all cases the estimated precision was affected by the seasonal signals (annual and semiannual) as they are preserved in time-series. The RMS for station position time-series was computed for each station individually. The average values of precision for the entire network are provided in Table 9. It can be seen, that the precision provided in the SINEX file is rather too high (less than 1 mm for the coordinates).

To provide an estimate, that rescales the error components to realistic values, the ratio between the precision inferred from different sources is compared. The estimates of the scale factor are provided in the Table 9. The scale factor for each component differs from each other, but they are in the same order of magnitude.

Similarly, the scale factors were estimated using a set of selected reference stations (e.g. GRAS, GRAZ, LROC, MEDI, WTZR and ZIMM). The estimated scale factors using those stations show larger values than the results derived from the complete network (Table 9).

For the sake of completeness, the scales were additionally derived from an arbitrary set of stations with low RMS values (approximately 1 mm for horizontal components and 2.5 mm for the vertical one) of position time-series. In this case, the following stations were selected: ACOM, GENO, JOUX, KARL and KRBG.

In all three cases, the values of scale factors for the East component are larger than the North component and the scale factor for vertical component is the smallest.

Table 9. Average values of an estimated precision from different sources and the scale factors.

Average precision / scale factor	Entire network			Reference ¹ stations			Arbitrary ² set of stations		
	East	North	Up	East	North	Up	East	North	Up
CRD_PLT_rms, mm	1.54	1.13	2.71	1.18	1.06	2.32	1.13	1.04	2.41
CRD_SNX_std, mm	0.035	0.041	0.142	0.012	0.013	0.033	0.016	0.02	0.063
Scale factor	44	28	19	97	85	71	68	52	39

¹ Reference stations are: GRAS, GRAZ, LROC, MEDI, WTZR and ZIMM.

² Arbitrary set of stations is: ACOM, GENO, JOUX, KARL and KRBG.

Based on the empirical experiments described before, the scale factors derived from entire network (see Table 9) were applied to the covariance matrix elements for the East, North and Up components respectively for further use.

The dependency of the formal error convergence with the time-span of the time-series is well observed in the Figure 23. The large velocity uncertainties are mostly related to the stations with shorter observation interval (in the order of 2-4 years only) (Nguyen et al., 2016). With the increase of the observation time, the precision is improved. As it seen from Figure 23, after 6-7 years of observations, the velocity precision reach stable values of approximately 0.1-0.2 mm/a for horizontal components and 0.2-0.4 mm/a for vertical one.

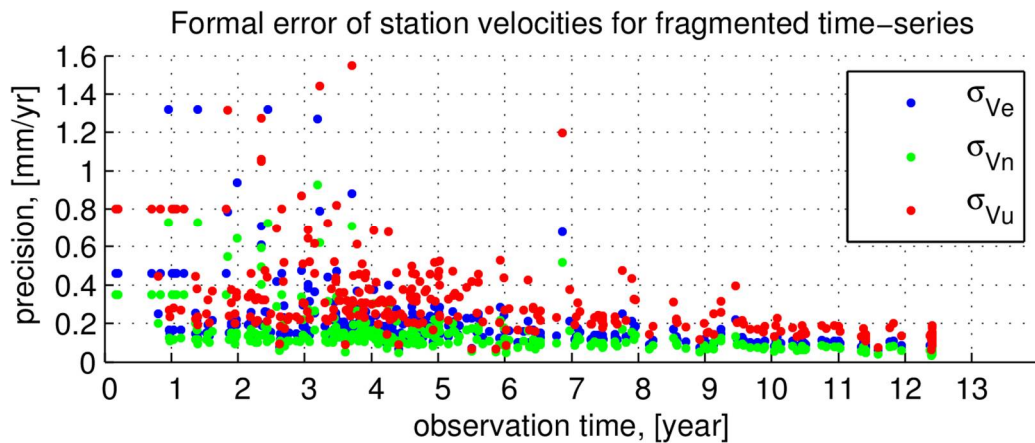


Figure 23. Dependency of the station velocity precision on the extension of observation period.

4.2 Estimation of the Eurasian plate motion.

To better identify surface-deformations in the studied area, the station velocities are reduced by the motion of the underlying tectonic plate, in this case the Eurasian plate (Figure 20). The resulting velocities are referred as residual velocities.

To estimate the residual velocities in the European region, it is possible to apply a Helmert transformation from the International Terrestrial Reference Frame (ITRF) to the European Terrestrial Reference Frame (ETRF) (Boucher and Altamimi, 2011). Indeed, this transformation provides appropriate results for the horizontal velocity component (Figure 24), but it introduces a notable bias in the vertical component (Figure 24). Hence, it is only useful at an earlier stage, when only a portion of the data is processed, but it is insufficient for reliable estimation of plate motion.

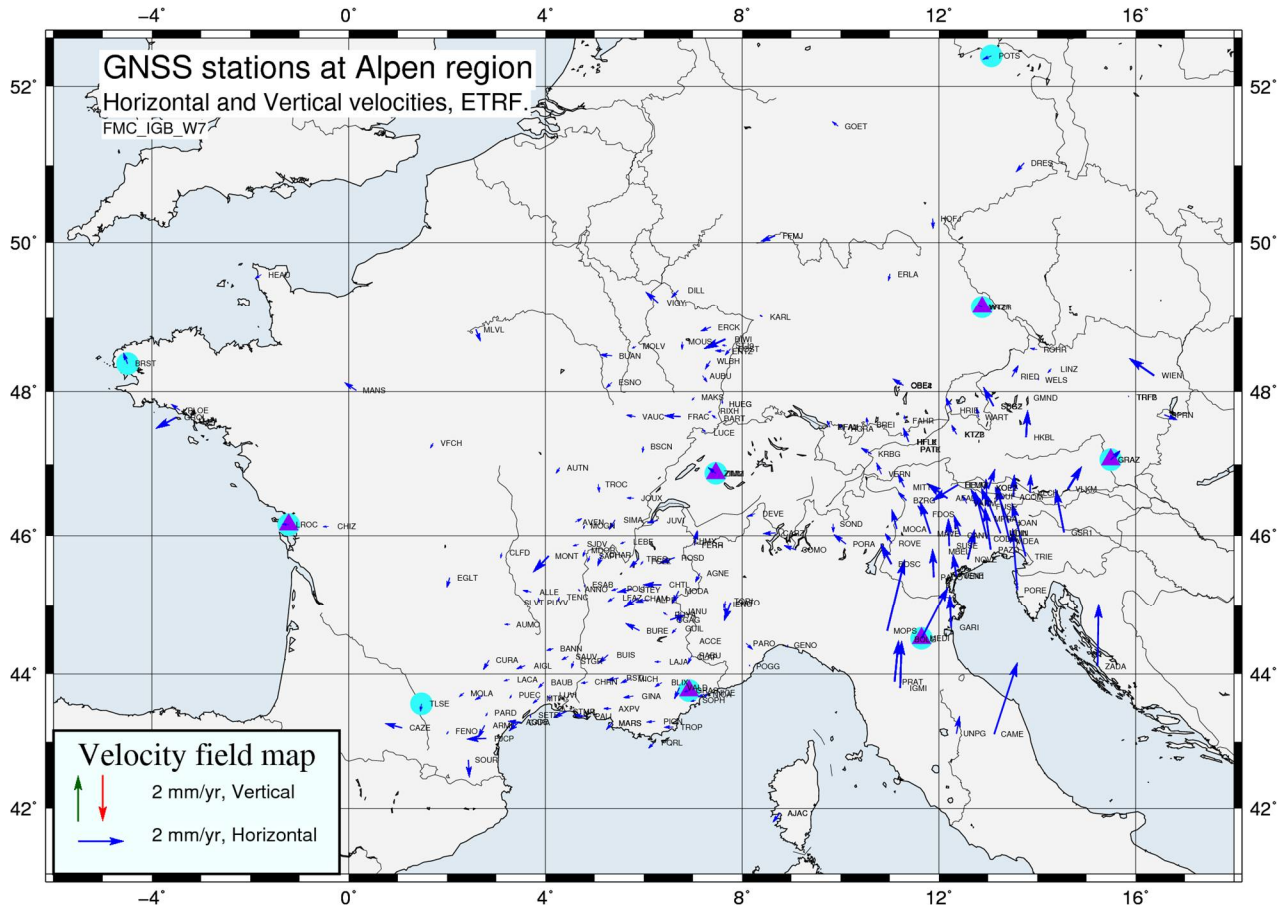


Figure 24. Horizontal residual velocities after ITRF/ETRF transformation.

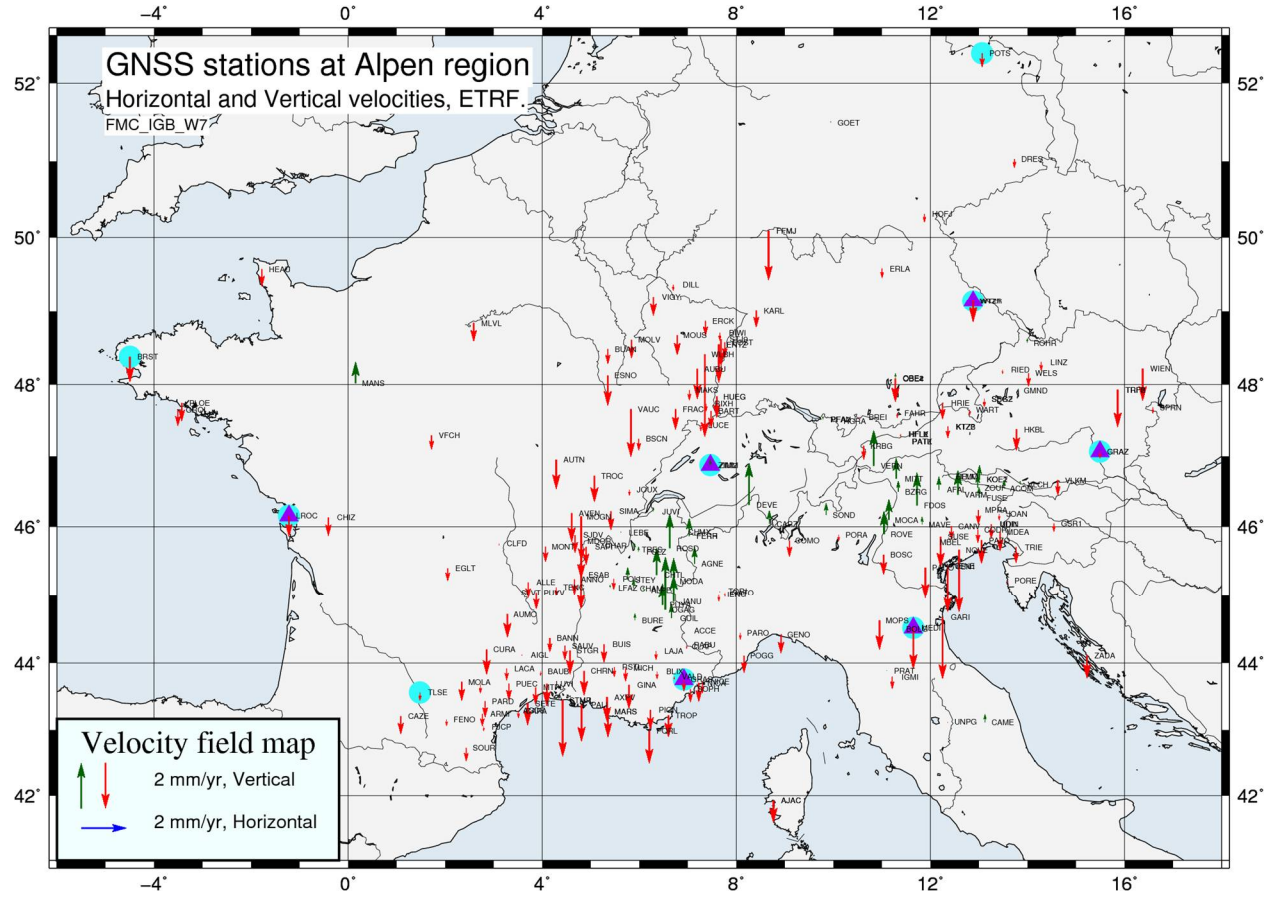


Figure 25. Vertical velocities after ITRF/ETRF transformation

As the ETRF is defined to be fixed to the stable part of the Eurasian plate, it can be assumed that this transformation removes the plate motion from the station coordinates. In practice, ETRF/ITRF transformation requires two consecutive transformations. At first, to propagate positions and velocities with respect to the central epoch, (the year 2000.0, since transformation parameters provided by Boucher and Altamimi (2011) are derived for this epoch), and secondly, to transform between the International and the European reference frames. This transformation can be applied to the coordinates obtained in this study because, as already mentioned, the ITRF2008 and the IGB08 are nominally identical.

The better and direct fundamental approach for the removal of the plate motion is the usage of the Euler pole. The estimation of the Euler pole for the Eurasia plate is performed in this study by the method provided by Drewes (1982), which is described in the section 4.2.1.

4.2.1 Estimation of the Euler pole

The method to describe the rigid tectonic plate motion relies on the Euler theorem. It assumes that the stations are located on a rigid spherical surface (tectonic plate), which experiences rotation around the Euler pole. Thus, the station velocities could be expressed as the motion with angular velocity ω around the common Euler pole Ω (Figure 26). The motion of the tectonic plates is known to be small with respect to the Earth radius.

During the time interval Δt the station moves with velocity v_i (horizontal displacement can be expressed as $\Delta\lambda_i$ and $\Delta\varphi_i$) from position $P_i(t)$ to position $P_i(t + \Delta t)$ forming the geocentric angle $\omega_K\Delta t$ with respect to the Euler pole $\Omega_K(\varphi_K, \lambda_K, \omega_K)$ axis.

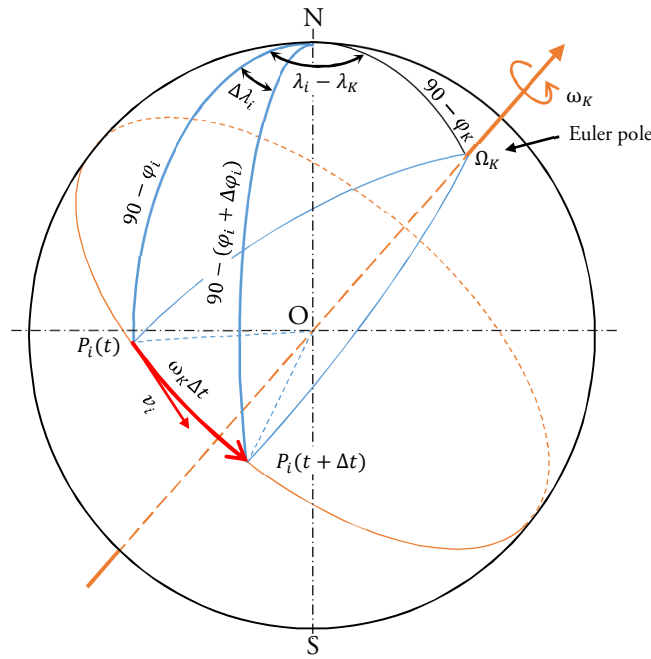


Figure 26. Illustration of the Euler pole. N is the North. O is the origin or the geocenter. The red arrows show the station velocity of the point P_i . The Euler pole is illustrated with orange color.

The method for the estimation of the Euler pole (Drewes, 1982) requires an approximate a-priori knowledge of the Euler vector for a given plate. For this purpose, the geophysical model NNR-NUVEL-1A (Jin and Zhu, 2004) is applied.

The estimated Euler pole $\widehat{\Omega}$ is equal to the sum of a-priori known value Ω_K and the estimated correction $d\widehat{\Omega}$:

$$\widehat{\Omega} = \Omega_K + d\widehat{\Omega} \quad (6)$$

$$\widehat{\Omega} = (\widehat{\varphi}, \widehat{\lambda}, \widehat{\omega})^T \quad - \text{is the estimated Euler pole;}$$

$\Omega_K = (\varphi_K, \lambda_K, \omega_K)^T$ – is an a-priori Euler pole;

$d\hat{\Omega} = (d\hat{\varphi}, d\hat{\lambda}, d\hat{\omega})^T$ – is the estimated Euler pole correction.

The estimation of the Euler pole correction $d\hat{\Omega}$, is performed by means of the least-squares adjustment:

$$d\hat{\Omega} = (\mathbf{A}^T \mathbf{P} \mathbf{A})^{-1} \mathbf{A}^T \mathbf{P} \mathbf{l} \quad (7)$$

where the design matrix \mathbf{A} is given by:

$$\mathbf{A} = \begin{bmatrix} -\sin\varphi_K \sin(\lambda_i - \lambda_K) \omega_K dt & (\cos\varphi_K + \cos(\lambda_i - \lambda_K)) \tan\varphi_i \sin\varphi_K \omega_K dt \\ -\cos\varphi_K \cos(\lambda_i - \lambda_K) \omega_K dt & -\sin(\lambda_i - \lambda_K) \tan\varphi_i \cos\varphi_K \omega_K dt \\ \cos\varphi_K \sin(\lambda_i - \lambda_K) dt & (\sin\varphi_K - \cos(\lambda_i - \lambda_K)) \tan\varphi_i \cos\varphi_K dt \end{bmatrix} \quad (8)$$

The observation vector \mathbf{l} is defined as following:

$$\mathbf{l} = \begin{bmatrix} v_{\varphi_i} - \cos\varphi_K (\sin(\lambda_i - \lambda_K)) \omega_K dt \\ v_{\lambda_i} - (\sin\varphi_K (\cos(\lambda_i - \lambda_K)) \tan\lambda_i \cos\lambda_K \omega_K dt) \end{bmatrix} \quad (9)$$

where \mathbf{P} – weighting matrix;

φ_K – latitude of the plate's Euler pole;

λ_K – longitude of the plate's Euler pole;

φ_i – latitude of an i -th station;

λ_i – longitude of an i -th station;

ω_K – angular velocity of the plate around the Euler pole;

v_{φ_i} – lateral velocity of i -th station;

v_{λ_i} – longitudinal velocity of i -th station;

dt – time interval.

For the precise estimation of the plate motion, only the stations located on the stable part of the Eurasian plate are used. The stations located inside the Alpine orogen (see Figure 20) are excluded. An additional iteration is performed after excluding those stations, whose residual velocity is not within the 1-sigma range (Figure 27).

Horizontal and vertical velocity fields

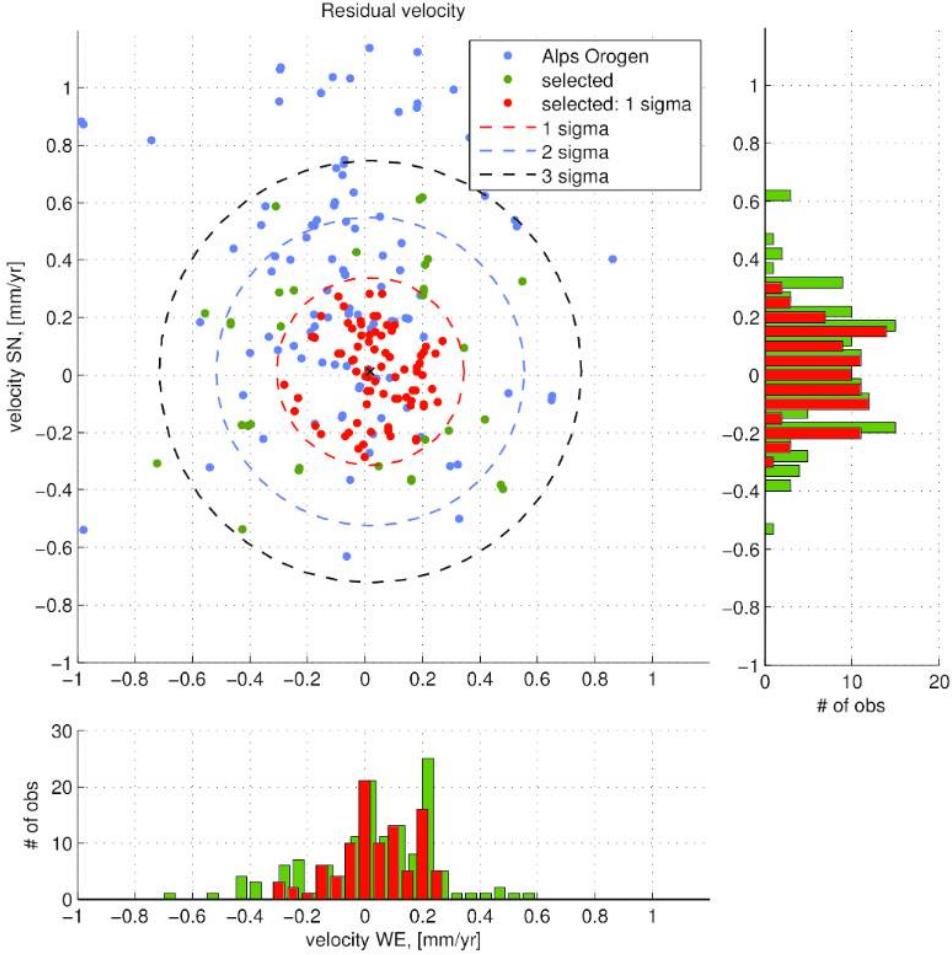


Figure 27. Statistics of horizontal residual velocities used for estimation of the Euler pole. The blue dots are station velocities located in the Alpine orogen and most of them are out of the scope of the figure due to the large velocity component in North direction (approximately 2-3 mm/a). The green and red dots and the histogram bars represent available station velocities from the stable part on the Eurasian plate.

Table 10 and Figure 28 show the coordinates and the rotation vector of the Euler pole estimated in this study and those contained in the model NNR-NUVEL-1A.

Table 10. Euler pole for the Eurasian plate.

Euler Pole	Latitude φ , deg	Longitude λ , deg	Angular velocity Ω , deg/Ma
NNR-NUVEL-1A	50.60	-112.30	0.2340
This study	55.95±5.60	-97.41±1.60	0.2636±0.0007

The difference between these values is explained by the different input data used in this study and the geophysical model, and the relatively small coverage of the network around the Alpen region with respect to the entire Eurasian plate. In addition, the objective of the current research is the study of the local deformation effects in mountains, thus, the surrounding velocity is minimized.

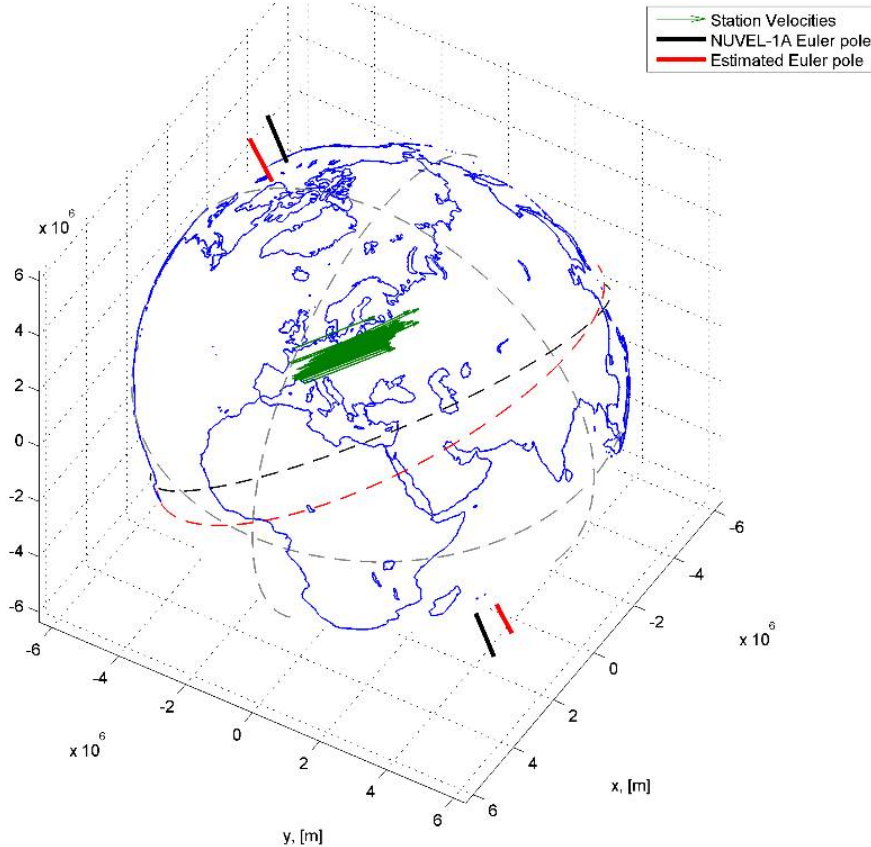


Figure 28. Illustration of the Euler pole for the Eurasian plate (for the European region). The green arrows are the stations velocities, scaled by factor of 10^8 for better demonstration. The black axis show the Euler pole provided by the NNR-NUVEL-1A model. The red axis corresponds to the Euler pole computed in this study.

4.3 Residual horizontal velocity field

Figure 29 shows the residual velocity field after removing the Eurasian plate motion from the station velocities. Now, it is possible to distinguish small intraplate motions in the Eastern Alps; and the relative tectonic plate motion: The Adriatic micro-plate collides with the Eurasian plate. The western Alpine orogen region shows almost no horizontal motion. Most of the reference stations show almost zero residual horizontal velocities, except for stations MEDI and GRAZ, which are moving at a rate of about 2.5 mm/a and 0.7 mm/a northeastwards, respectively.

The formal errors of the estimated station velocities are taken from the SINEX file and the corresponding velocity formal error in the East and North components were rescaled by factor of 44 and 28 accordingly (see section 4.1).

The detailed discussion on, the residual horizontal velocity and surface-deformation fields is provided in the section 5.3.

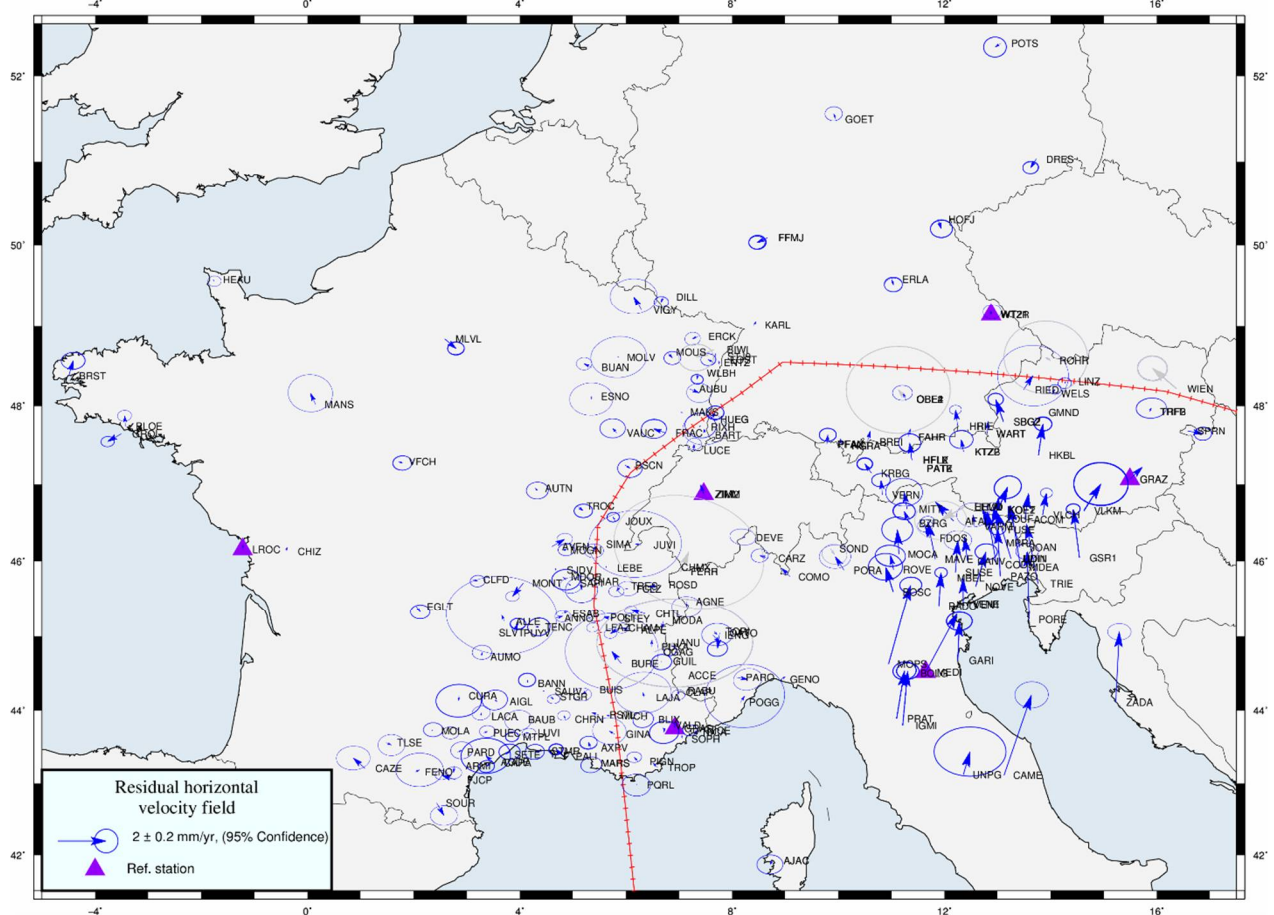


Figure 29. Residual horizontal velocity field after removing the Eurasian plate motion from the station velocities. The uncertainty ellipses are taken from the covariance matrix of the solution (SINEX) file and rescaled. The gray color arrows are the outliers. The red line outlines boundary of the Alpine orogen (Bird, 2003)

4.4 Validation of the horizontal and vertical velocity fields

The performance the estimated velocity field was verified by the comparison with three different external solutions: the EPN (e.g. EPN_A_IGb08_C1920) (Bruyninx et al., 2012), Swisstopo (Brockmann et al., 2014) and France (Nocquet et al., 2016). The first two solutions were computed with similar strategies using the Bernese GNSS software, while the last one was computed using GAMIT (Herring et al., 2010). The details of the external velocity fields are provided in the Table 11. In all three cases, a statistically reliable comparison was possible, since a sufficient number of common stations was available and the reference frames are consistent.

The residual horizontal velocities for the EPN and Swisstopo solutions were obtained using the previously estimated Euler pole (section 4.2.1) from the network ALPNET (current study, Figure 1). The results of (Nocquet et al., 2016) mainly cover the French Alps and already provide the residual horizontal velocities, without total velocity components. The Euler pole of that study was obtained

from station velocities in the Western Alps using 16 stations only. It significantly differs from the Euler pole estimated in the current study.

Table 11. The external velocity fields used for comparison.

Solution	Source	Number of common stations
EPN	ftp://epncc.oma.be/pub/station/coord/EPN/EPN_A_IGb08.SNX.Z (Bruyninx et al., 2012)	51
Swisstopo	http://pnac.swisstopo.admin.ch/divers/dens_vel/ch08_hor_i08.vel http://pnac.swisstopo.admin.ch/divers/dens_vel/ch08_ver_i08.vel (Brockmann et al., 2014)	50
France	http://www.nature.com/article-assets/npg/srep/2016/160627/srep28404/extref/srep28404-s1.pdf (Nocquet et al., 2016)	45

Figure 30 illustrates the comparison of the station velocities obtained in this study (Figure 21 and Figure 22) with the three different external sources. In Figure 30, the horizontal axis corresponds to the results estimated in this study and the vertical axis corresponds to the results in the external one. The RMS of the difference between both solutions is computed to quantify the velocity discrepancies. In all three cases, the distribution of the results is similar. The formal error velocity difference is nearly 0.2 mm/a and 0.45 mm/a for the horizontal and vertical components, respectively. The best agreement is observed with the Swisstopo solution with a deviation of about 0.15 mm/a and 0.36 mm/a for horizontal and vertical components, respectively. In the two first cases, the RMS of the velocity difference in the North component is smaller by approximately 15%, than for the East component.

Using the comparison provided in the Figure 30, it is possible to conclude, that the estimated accuracy of the station velocities in this study is approximately $0.15\text{--}0.25 \text{ mm/a}$ for the horizontal components and $0.4\text{--}0.5 \text{ mm/a}$ for the vertical one. Those values are in agreement with the results presented in section 4.1 (Figure 23). Also, those results are in agreement with a recent study performed by Brockmann (2016).

Horizontal and vertical velocity fields

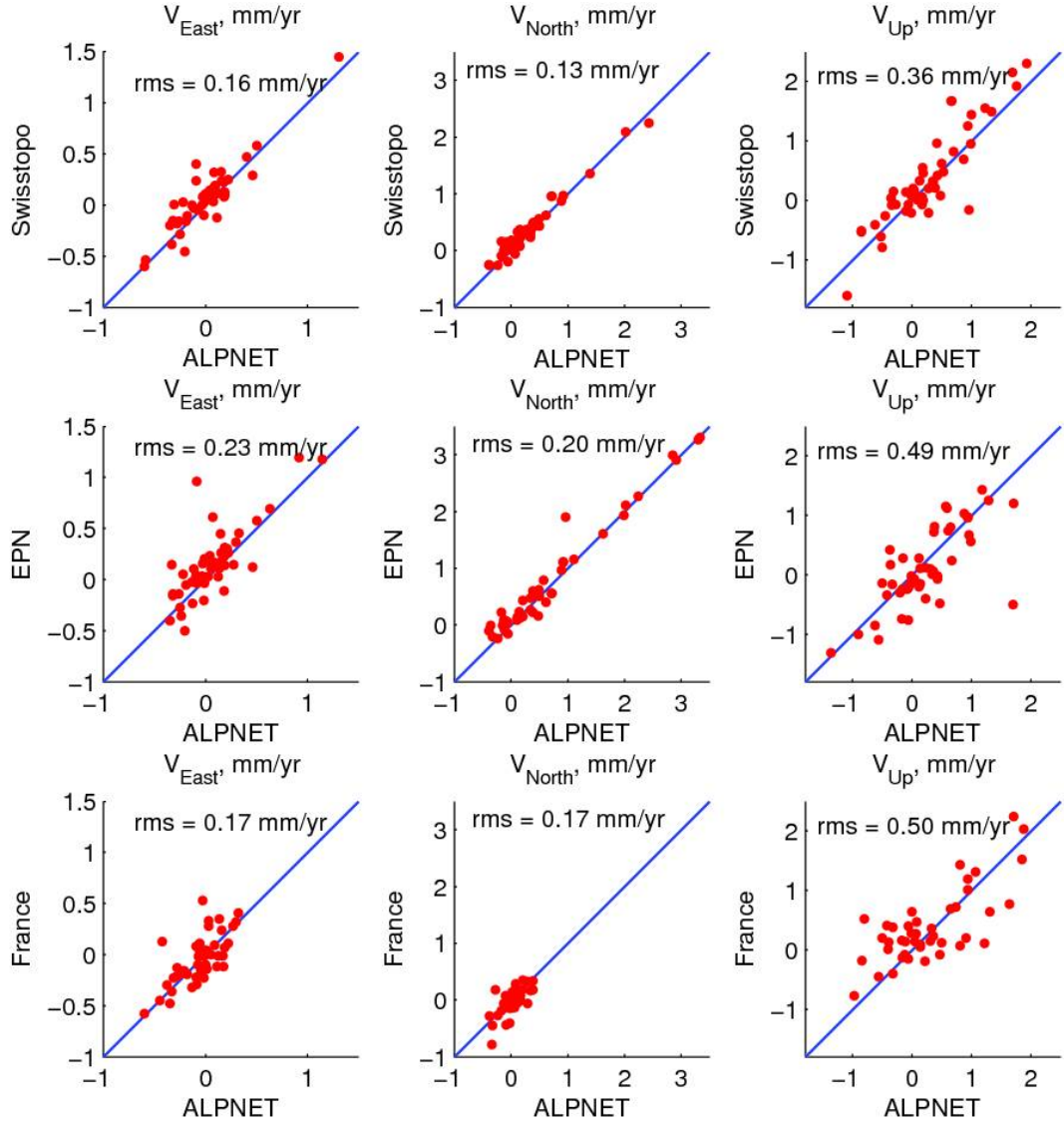


Figure 30. Validation of estimated velocities. Comparison of station velocities obtained in this study with those published by the Swisstopo (Brockmann et al., 2014), EPN (ftp://epncb.oma.be/pub/station/coord/EPN/EPN_A_IGb08.SNX.Z, Bruyninx et al., 2012) and France (Nocquet et al., 2016).

5 Horizontal surface-deformation field

The station velocities described in Chapter 4 are interpolated to a continuous surface deformation model using the least-square collocation (LSC) approach. This method was extensively developed by Moritz (1972, 1973, 1976) for gravimetric data and further applied for the computation of deformation model based on discrete station velocities (e.g. Heidbach and Drewes, 2003; Drewes and Heidbach 2005, 2012, Sánchez and Drewes, 2016). The gravimetric measurements are often taken as discrete measurements along the path, while networks of permanent GNSS stations usually do not have any regular grid, which is the case for the current study. The application of this method to randomly distributed measurement points is possible, if the network is dense enough to reveal certain spatial features (e.g. mountain uplift, relative tectonic plate motion, etc.). The fundamental principle of the LSC is the correlation of physical parameters (e.g. station velocities) in adjacent points. Therefore, a correlation (covariance) function has to be given or be determined empirically.

In this study, empirical covariance functions are used. Their determination is described in section 5.1 and their use in the LSC approach is presented in section 5.2. The resulting deformation field model is provided in section 5.3.

5.1 Empirical covariance function

In practice, an empirical covariance function is often known a-priori or derived from observations. In this case, the observations l are the station velocities (after a trend motion of the Eurasian plate has been removed). For their interpolation at regular grid points, observations located within a certain radius from the regular grid point are selected.

For the estimation of the velocity components at a grid point, observations within region of interest (ROI) with a certain radius (for instance, 150 km and 250 km for horizontal and vertical velocity fields, respectively) are selected. For a given ROI, the distances (baselines) between points are sorted by their length and grouped into several classes Δ (Figure 31b). Criterion for the allocation to a certain class Δ_k is the baseline length (in other words, the classes with short baselines, medium baselines, etc.). The classes are separated from each other by 2δ . The zero class Δ_0 ($d = 0$) represents the auto-correlation or auto-covariance $C_{ss}(0)$ and has the largest value (Figure 31b). In practice, it is convenient to group covariances into 7-10 classes, but with a separation distance 2δ less than 50 km. The larger the separation distance 2δ the stronger the averaging of the discrete covariances (Jiang et al., 2014). The selected radius of the ROI is mainly dictated by the size of the spatial features and coverage of the network. The increase of the radius of the ROI may lead to negative values of discrete covariances for classes with large baselines. For the estimation of the empirical covariance function, the observation l_i is referred to a residual velocity and had properties of a stochastic signal (e.g. stationarity and isotropy).

In Figure 31a it can be seen that the covariance function of the observations C_{ll} comprises the covariance function of the stochastic signal C_{ss} and the contributing noise C_{nn} . Under the assumption of uncorrelated noise, only the auto-covariance of the observation $C_{ll}(0)$ is contaminated by the noise fraction $C_{nn}(0)$, (Figure 31b and eq. (10)). Thus, if noise is minimized or totally removed, the collocation acts similar like a filter (Mikhail and Ackerman, 1976).

$$C_{ll}(0) = C_{ss}(0) + C_{nn}(0) \quad (10)$$

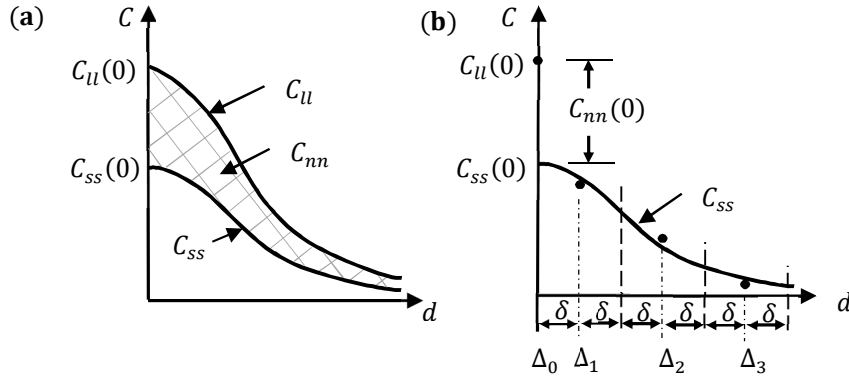


Figure 31. Empirical covariance function.

The cross-covariance $C_{ll}(\Delta_k)$ and auto-covariance $C_{ll}(0)$ are computed as follows:

$$C_{ll}(\Delta_k) = \frac{1}{n_k} \sum_{i < j}^k l_i l_j, \quad (11)$$

$$C_{ll}(0) = \frac{1}{n} \sum_{i=1..n} l_i^2, \quad (12)$$

- where n_k – is the number of points in the class Δ_k .
- n – is the total number of points.
- l_i, l_j – are the observation values at the points i and j .
- i, j – are the indexes of points.
- Δ_k – is a class of points with separation distance 2δ between point pairs.
- k – is the class number.

After estimating the discrete empirical covariances in eq. (11) and (12), they are approximated by a continuous function $C(d)$ as shown in eq. (13). In geodesy, the exponential function eq. (13) is often used as an empirical covariance function (Moritz, 1976). The drawback of the exponential function is the non-zero first derivative at distance d , which is equal to zero. However, the function itself does not experience any rapid decay with the growing distance. Nevertheless, the exponential function allows to interpolate data points that have large separation distances (e.g. 10-100 km).

$$C(d) = C_0 \exp(-a \cdot d), \quad (13)$$

- where C_0 – is the covariance function coefficient, equal to $C_{ss}(0)$;

- a – is a function parameter responsible for the slope decay;
- d – is the distance.

5.2 Least-Squares Collocation

The least-squares collocation method is a combination of a well-established technique based on least-squares adjustment with those of interpolation and filtering. The interpolation is a process for the estimation of unknown values at specified locations (for example, at grid points) using measurements of adjacent points. Filtering is a process of noise reduction.

In theory, the observation v (in this case, the station velocity) is composed of the trend v_t (e.g. large-scale variations: like the tectonic plate motion), stochastic component v_s (referred as signal and used for estimation of the empirical covariance function) and the observation error (noise) v_n (see eq. (14)).

$$v = v_t + v_s + v_n \quad (14)$$

Figure 32 illustrates the one-dimensional case of the LSC. The horizontal axis denotes the spatial distance r with observations taken at points r_i . The vertical axis denotes the observable V . For the i -th observation value, the circles with error bar are the observation x_i with noise n_i and a corresponding element of the noise covariance matrix C_{nn} . The estimate of the observation \hat{v} is composed of the estimate for the trend function v_t and the estimate for the stochastic signal v_s . The covariance matrix C_{ss} represents the correlation between the signal v_s and the estimate of the interpolation at grid point v_s .

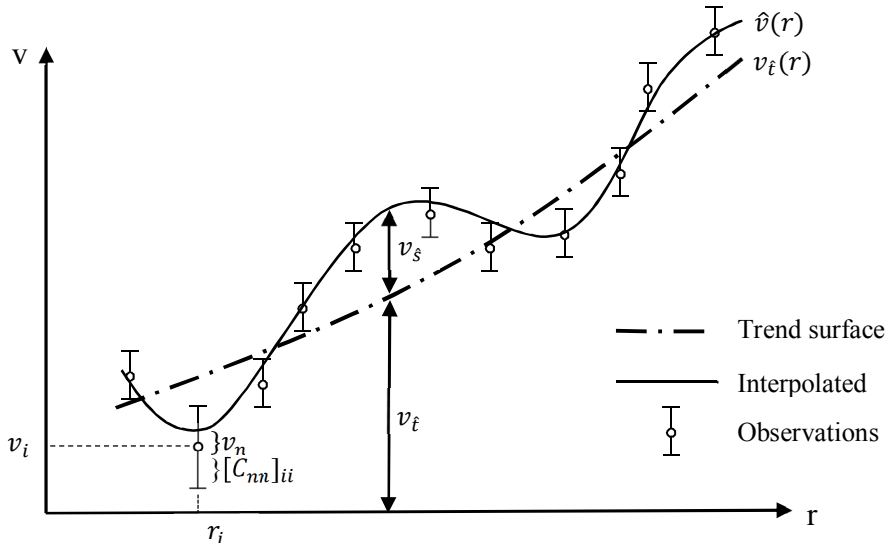


Figure 32. Interpolation of measurements with the LSC for one dimensional case.

In case of interpolating the residual horizontal velocity field, the trend function v_t (plate motion) is removed and the residual velocities are assumed to be signal v_s .

The procedure of least-squares collocation is defined as follows (Mikhail and Ackerman, 1976):

$$\mathbf{v}_{\hat{s}} = \mathbf{C}_{\hat{s}\hat{s}} \mathbf{C}_{ss}^{-1} \mathbf{v}_s \quad (15)$$

- where \mathbf{v}_s – is the vector of the stochastic signal;
 $\mathbf{v}_{\hat{s}}$ – is the estimated or interpolated value at a grid point;
 $\mathbf{C}_{\hat{s}\hat{s}}$ – is the non-symmetric covariance matrix between signals \mathbf{v}_s and the interpolated value $\mathbf{v}_{\hat{s}}$;
 \mathbf{C}_{ss} – is the symmetrical covariance matrix between signals \mathbf{v}_s .

The covariance matrices $\mathbf{C}_{\hat{s}\hat{s}}$ and \mathbf{C}_{ss} in the eq. (15) are built from the empirical covariance functions. Details are given in the eq. (16) and are described by Mikhail and Ackerman (1976) and illustrated in the Figure 31. For the three-dimensional case the eq. (15) is written in the following way:

$$\begin{bmatrix} \mathbf{v}_e \\ \mathbf{v}_n \\ \mathbf{v}_u \end{bmatrix}_{\hat{s}} = \begin{bmatrix} \boldsymbol{\sigma}_{e_{\hat{s}}e} & \boldsymbol{\sigma}_{e_{\hat{s}}n} & \boldsymbol{\sigma}_{e_{\hat{s}}u} \\ \boldsymbol{\sigma}_{n_{\hat{s}}e} & \boldsymbol{\sigma}_{n_{\hat{s}}n} & \boldsymbol{\sigma}_{n_{\hat{s}}u} \\ \boldsymbol{\sigma}_{u_{\hat{s}}e} & \boldsymbol{\sigma}_{u_{\hat{s}}n} & \boldsymbol{\sigma}_{u_{\hat{s}}u} \end{bmatrix} \begin{bmatrix} \boldsymbol{\Sigma}_{ee} & \boldsymbol{\Sigma}_{en} & \boldsymbol{\Sigma}_{eu} \\ \boldsymbol{\Sigma}_{en} & \boldsymbol{\Sigma}_{nn} & \boldsymbol{\Sigma}_{nu} \\ \boldsymbol{\Sigma}_{eu} & \boldsymbol{\Sigma}_{nu} & \boldsymbol{\Sigma}_{uu} \end{bmatrix}^{-1} \begin{bmatrix} \mathbf{v}_e \\ \mathbf{v}_n \\ \mathbf{v}_u \end{bmatrix}_s \quad (16)$$

- where $\mathbf{v}_{e_{\hat{s}}}, \mathbf{v}_{n_{\hat{s}}}, \mathbf{v}_{u_{\hat{s}}}$ – are the estimates of the three components at the grid point.
 $\mathbf{v}_{e_s}, \mathbf{v}_{u_s}, \mathbf{v}_{u_s}$ – are each a $1 \times n$ row vector with the signal.
 $\boldsymbol{\sigma}_{e_{\hat{s}}e}, \boldsymbol{\sigma}_{e_{\hat{s}}n}, \boldsymbol{\sigma}_{e_{\hat{s}}u}$ – are each a $1 \times n$ row vector of covariances between the interpolated $\mathbf{v}_{e_{\hat{s}}}$ and the signal values $\mathbf{v}_{e_s}, \mathbf{v}_{u_s}, \mathbf{v}_{u_s}$, respectively;
 $\boldsymbol{\sigma}_{n_{\hat{s}}e}, \boldsymbol{\sigma}_{n_{\hat{s}}n}, \boldsymbol{\sigma}_{n_{\hat{s}}u}$ – are each a $1 \times n$ row vector of covariances between the interpolated $\mathbf{v}_{n_{\hat{s}}}$ and the signal values $\mathbf{v}_{e_s}, \mathbf{v}_{u_s}, \mathbf{v}_{u_s}$, respectively.
 $\boldsymbol{\sigma}_{u_{\hat{s}}e}, \boldsymbol{\sigma}_{u_{\hat{s}}n}, \boldsymbol{\sigma}_{u_{\hat{s}}u}$ – are each a $1 \times n$ row vector of covariances between the interpolated $\mathbf{v}_{u_{\hat{s}}}$ and the signal values $\mathbf{v}_{e_s}, \mathbf{v}_{u_s}, \mathbf{v}_{u_s}$, respectively.
 $\boldsymbol{\Sigma}_{ee}, \boldsymbol{\Sigma}_{nn}, \boldsymbol{\Sigma}_{uu}$ – are each an $n \times n$ square symmetric matrix of auto-covariances of the given signal values $\mathbf{v}_{e_s}, \mathbf{v}_{u_s}, \mathbf{v}_{u_s}$, respectively.
 $\boldsymbol{\Sigma}_{en}, \boldsymbol{\Sigma}_{eu}, \boldsymbol{\Sigma}_{nu}$ – are each an $n \times n$ square matrix of cross-covariances of the given signal.

In order to exploit the precision of the estimated velocities, the noise covariance matrix \mathbf{C}_{nn} is added to the observation covariance matrix \mathbf{C}_{ss} . In this way eq. (15) may be written as:

$$\mathbf{v}_{\hat{s}} = \mathbf{C}_{\hat{s}\hat{s}} (\mathbf{C}_{ss} + \mathbf{C}_{nn})^{-1} \mathbf{v}_s \quad (17)$$

The covariance between observed station velocities is assumed to be equal to zero, since their correlation is several orders of magnitude less than the variance of interpolated velocities (Figure 32). The estimated precision of estimated signal is given by:

$$\mathbf{E}_{\hat{s}\hat{s}} = \mathbf{C}_{\hat{s}\hat{s}} - \mathbf{C}_{\hat{s}\hat{s}} (\mathbf{C}_{ss} + \mathbf{C}_{nn})^{-1} \mathbf{C}_{\hat{s}\hat{s}}^T, \quad (18)$$

- where $\mathbf{C}_{\hat{s}\hat{s}}$ – is a diagonal matrix built using eq. (12).

For the LSC of the vertical surface-deformation field, Egli et al. (2007) provide a similar approach to the LSC method defined by Mikhail and Ackermann (1982), which was covered in section 5.2. By

definition, a trend (large-scale variation) function \boldsymbol{v}_t is well distinguished from the observations \boldsymbol{v} (in this case, the station velocities). The difference between the actual observations and the trend function is comprised of the stochastic signal \boldsymbol{v}_s (small-scale variation) and a noise. The estimation of the trend function can be done by collocation in a separate step using eq. (19). For instance, for the vertical velocity field, the trend function $\boldsymbol{v}_{\hat{t}}$ and the stochastic signal $\boldsymbol{v}_{\hat{s}}$ can be estimated in two consecutive steps:

$$\boldsymbol{v}_{\hat{t}} = \mathbf{C}_{\hat{t}\hat{t}}(\mathbf{C}_{tt} + \mathbf{C}_{ss} + \mathbf{C}_{nn})^{-1}\boldsymbol{v} \quad (19)$$

and

$$\boldsymbol{v}_{\hat{s}} = \mathbf{C}_{\hat{s}\hat{s}}(\mathbf{C}_{ss} + \mathbf{C}_{nn})^{-1}(\boldsymbol{v} - \boldsymbol{v}_{\hat{t}}) \quad (20)$$

And the associated precision of the trend $\mathbf{E}_{\hat{t}\hat{t}}$ and the stochastic signal $\mathbf{E}_{\hat{s}\hat{s}}$ is given by:

$$\mathbf{E}_{\hat{t}\hat{t}} = \mathbf{C}_{\hat{t}\hat{t}} - \mathbf{C}_{\hat{t}t}(\mathbf{C}_{tt} + \mathbf{C}_{ss} + \mathbf{C}_{nn})^{-1}\mathbf{C}_{\hat{t}t}^T \quad (21)$$

and

$$\mathbf{E}_{\hat{s}\hat{s}} = \mathbf{C}_{\hat{s}\hat{s}} - \mathbf{C}_{\hat{s}s}(\mathbf{C}_{ss} + \mathbf{C}_{nn})^{-1}\mathbf{C}_{\hat{s}s}^T \quad (22)$$

where the covariances $\mathbf{C}_{\hat{t}\hat{t}}$ and $\mathbf{C}_{\hat{s}\hat{s}}$ can be built using the eq. (11), (12) and (13) presented in the section 5.1.

5.3 The resulting surface-deformation model

In the following study, at the step of the daily solution estimation, all GNSS stations were considered as belonging to the Eurasian plate exclusively. This assumption is based on the tectonic plate boundary model PB2002 (Bird, 2003). The partial inclusions of microplates (i.e. the Adria, Liguria and Pannonia) were assumed to be rigidly fixed with the Eurasian plate.

The horizontal surface-deformation field is computed on a regular grid with 0.25° spacing interval using eq. (16) and illustrated in the Figure 33. The grid size of 0.25° was chosen as appropriate since it corresponds to the mean baselines length (i.e. in the order of 20 km) in the most densely covered region in the network, which is the French Alps. A larger grid size would average out the results and this should be avoided. The ROI with 150 km radius provides an overlap between adjacent grid points and allow a certain degree of smoothing. A larger radius of ROI would average out small scale features (less than 150 km). For the areas with poor station coverage, a different strategy was used: the nearest 10 stations are used for the LSC. This is a compromise to derive a more reliable empirical covariance function (section 5.1). Outliers with discrepancy of more than 0.5 mm/a with respect to the velocities of the surrounding stations are excluded from the collocation. These outliers are considered to be affected by local deformation and do not represent the entire velocity field. For instance, station WIEN (Figure 35) is affected by a tunnel construction (Haslinger and Stangl, 2007) and it has velocity of

about 1.5 mm/a northwestwards, while the surrounding stations show 0.5 mm/a northeastwards. The stations HELM, WIEN, FERR, FERH, OGAG, SOND, OBE2, ROHR, BIWI, BI2I were considered as outliers in the estimation of horizontal surface-deformation field (outliers are shown with gray arrows in the Figure 33).

According to (Mikhail and Ackerman, 1982), if the correlation between observations (i.e. the North and East components of velocities) is negligible, the elements of the observation vector (North, East and Up components) can be treated as independent. The collocation is performed separately for each component (1D-case) or simply by setting the off-diagonal elements of matrix \mathbf{C}_{ss} in eq. (16) equal to zero. A significant correlation between the North and East velocities appears only at some regions of a local velocity field (for example, in the North-East of Italy, (Figure 35)). Since the empirical covariance function is isotropic (independent from direction), it cannot handle a reliable estimation of correlation between the North and East velocity components in the ROI with spare network coverage. Thus, the collocation in this study is performed without correlation term to provide consistent results. In Figure 33, the horizontal surface-deformation field shows the effect of the interaction between the tectonic plates in the Alpine orogen.

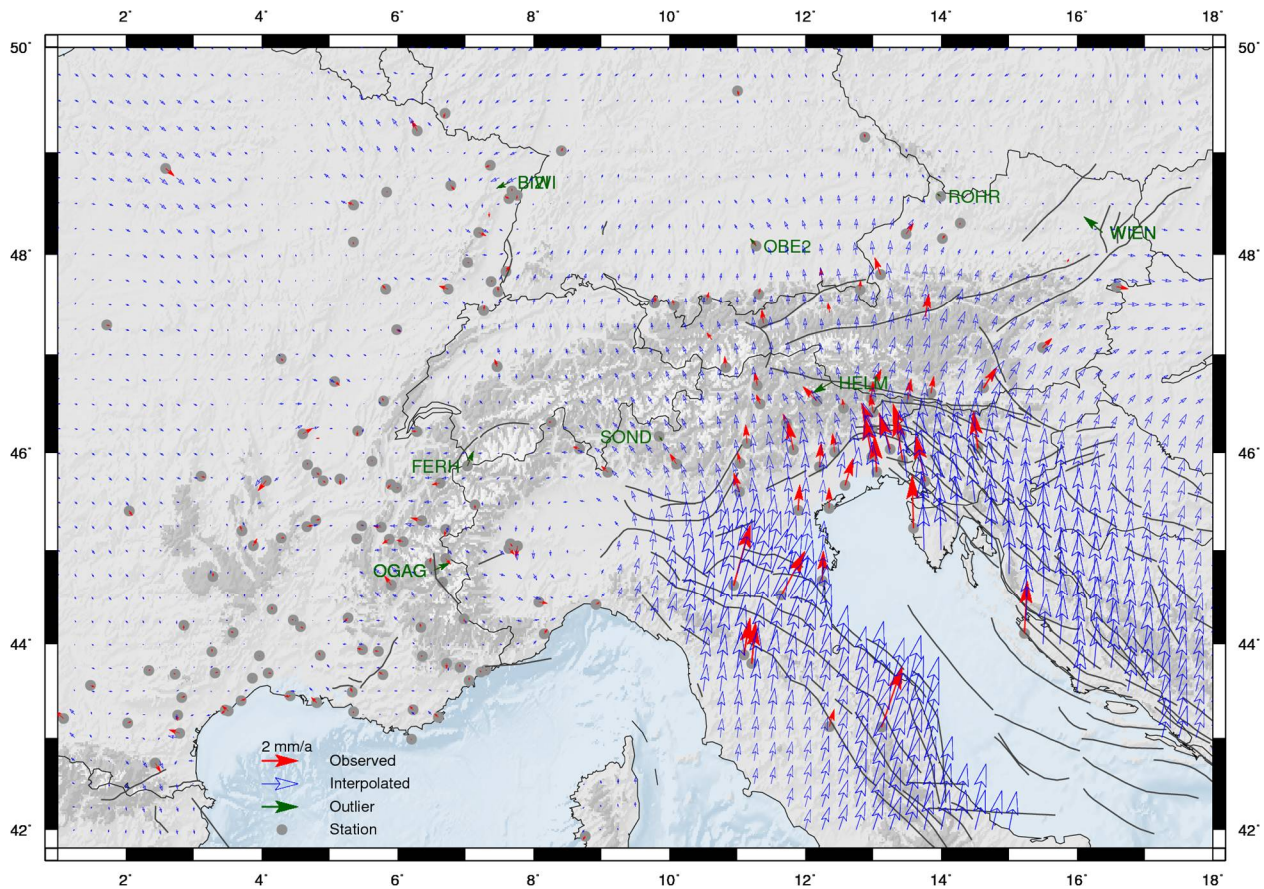


Figure 33. Horizontal components of the deformation field. Blue arrows represent the deformation field. Red arrows correspond to the input velocities. Uncertainty ellipses are not shown to avoid overloading of illustration. Dark gray lines are the tectonic faults (source: <http://diss.rm.ingv.it/share-edsf/>). The deformation field is represented with topography (ETOPO1) to illustrate the dependency of deformation with the local topography features.

The scale of deformation is changing gradually from the Western to the Eastern Alps. The largest deformation is observed on the eastern side of the boundary between the Adriatic and Liguria plates (forming the Apennines). Even though the Apennines are represented by 6 stations only, and the station velocities provide only a general picture of the local deformation. The precision of the estimated surface-deformation is shown in the Figure 36.

The results for the Western and part of Central Alps are illustrated with larger scale for the deformation and velocities in Figure 34. The Western Alps topography has a ‘concave-convex’-like structure, with the Po plane at the concave side. The motion of the Po plane and the concave part of the Western Alps is observed as the counter-clockwise rotation with the center approximately in the middle of vortex (Figure 34) in the Po plane (Bokelmann et al., 2013). The station velocities at this region are nearly tangential to the longitudinal axis of the mountain range. A slow deformation of about 0.2 mm/a in the western direction is seen in the convex part of the Western Alps. The two outliers (e.g. stations CHMX and OGAG) evident as they do not fit to the local deformation pattern. Probably these outliers are consequence of a local disturbance that does not fit to the general deformation field

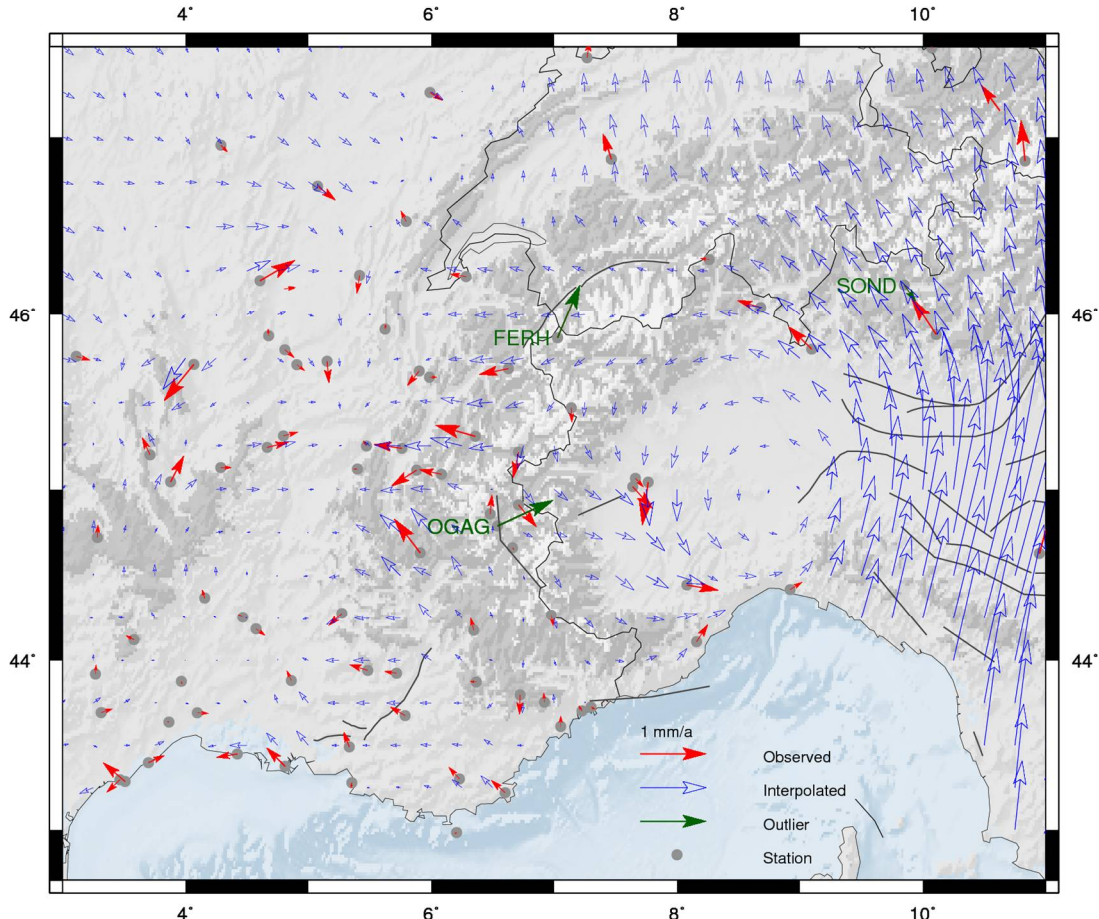


Figure 34. Surface-deformation field and residual horizontal velocity field of the Western and Central Alps. Blue arrows represent the deformation field. Red arrows correspond to the input velocities. Dark gray lines are the tectonic faults (source: <http://diss.rm.ingv.it/share-edsf/>). Topography represented by the ETOPO1 model.

Horizontal surface-deformation field

A recent study of Nocquet et al. (2016) on the Western Alps claims that there is almost no deformation in this region. The region in the east-southern part of France including the Massif Centrale mountains is also determined as stable. In the current study, the resulting residual station velocities and surface-deformation of the Western Alps show a certain spatial correlation with each other and a well-observed correlation with the local topography. Nevertheless, the residual station velocities are less than 0.5 mm/a for most of the stations.

Figure 35 shows the surface-deformation field for the Eastern and Central Alps. The Austrian Alpine regions shows similar gradual trends of approximately 0.5 mm/a northwards, but also diverge from each other. The stations in the western part of the Austrian Alps tend to move northwestwards, while the stations in the eastern part seems to move eastwards. The Italian Alps and the Friuli region show velocities up to 2 mm/a . This region shows the relative plate motion between the Eurasian plate and the Adriatic microplate.

Along the Swiss Alps, a sparse station coverage exists and the main source for deformation field are the stations in the neighboring countries. Presumably, the surface-deformation in Swiss Alps is relatively homogeneous with smooth transition to the surrounding regions. The results of the residual velocity field of the Central Alps provided by Brockmann et al. (2014) are in agreement with this study (see section 4.4).

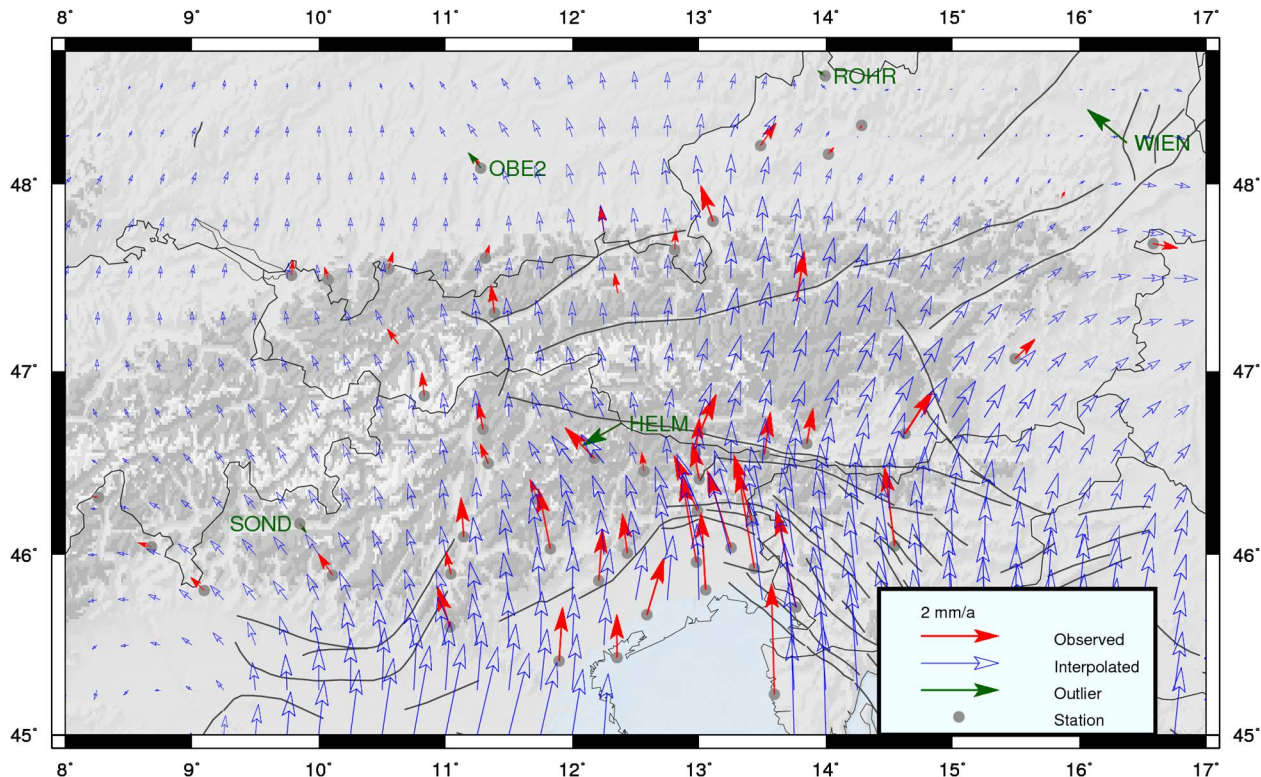


Figure 35. Surface-deformation field and residual horizontal velocity field of the Eastern and Central Alps. Blue arrows represent the deformation field. Red arrows correspond to the input velocities. Dark gray lines are the tectonic faults (source: <http://diss.rm.ingv.it/share-edsf/>). Topography represented by the ETOPO1 model.

The horizontal surface-deformation field including error ellipses is illustrated in the Figure 36. The precision of the deformation rate is estimated according to eq. (18) (Mikhail and Ackerman, 1976). The large uncertainty 0.5-1.0 mm/a occurs at the boundaries between tectonic plates and at low-station-coverage regions of a network (e.g. the Apennines and Dinarides). Large uncertainty of deformation field at Po plane is due to low-station-coverage of network and large variation of station velocities.

In the Western Alps, with dense coverage of GNSS-stations, the uncertainty of the surface-deformation field has reasonable values of approximately 0.2-0.4 mm/a, which are slightly worth than the precision of the station velocities. The same applies to the stable part of the observed Eurasian plate. As it is seen from Figure 36, the estimated precision of the surface-deformation field is highly correlated with the precision of the velocity field.

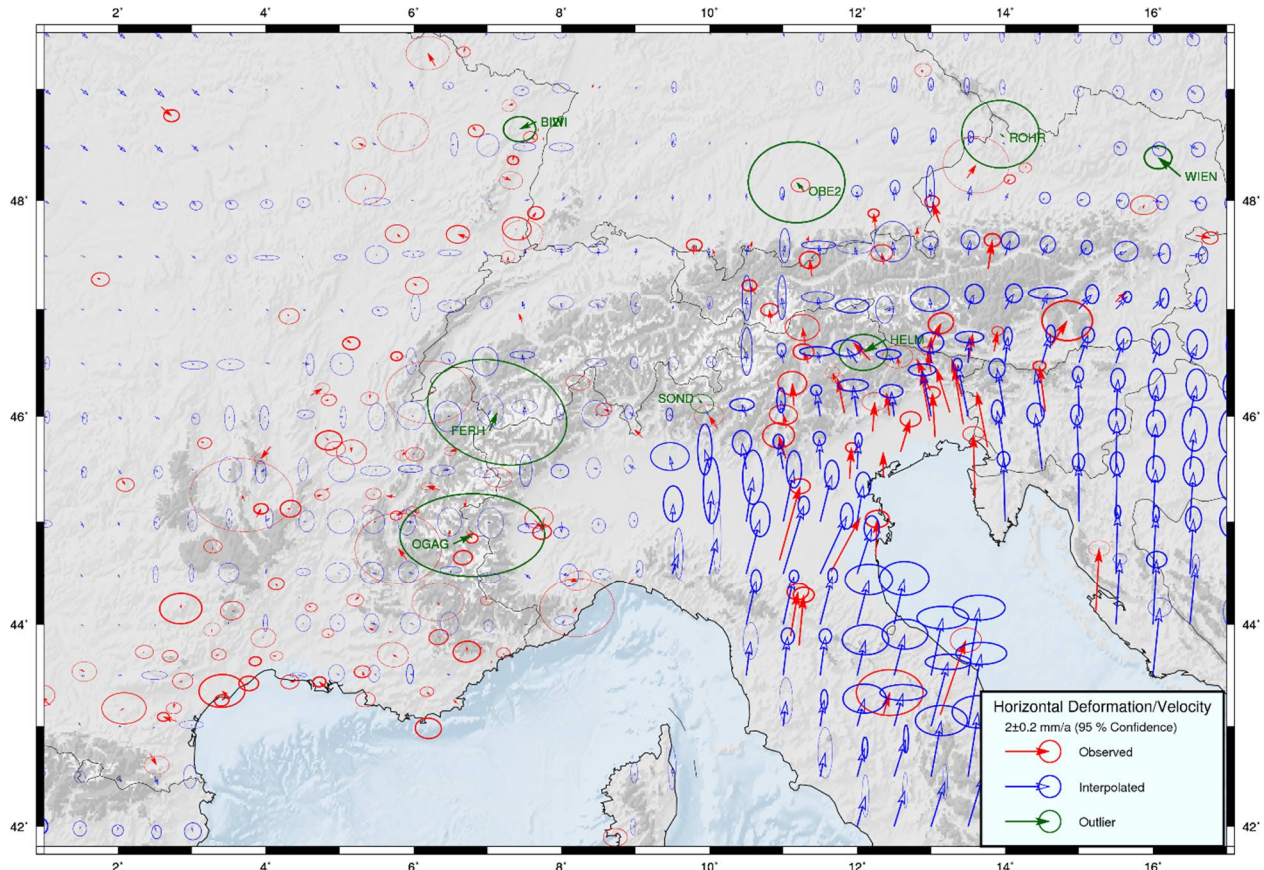


Figure 36. Estimated precision of the deformation field. The velocity and deformation fields are shown with their uncertainty ellipses to illustrate their correlation. Here, the deformation field is represented on 0.5° grid to avoid figure overloading. Topography represented by the ETOPO1 model.

6 Strain field

The strain field represents the zones with compression and extension (dilatation) on the surface of the plates (Means, 1979). In this study, the strain field is computed from the deformation field and not from the original observations. But one has to keep in mind that the deformation field is derived from the original observations using the LSC technique. The velocities of the grid points are used for the estimation of the velocity gradients, and those gradients are used for the computation of the strain components. The strain components are the principal (compression/dilatation) strain and the shear strain.

Even though the deformation field is available in three components only horizontal component is used. Thus, the obtained strain field is a horizontal projection of surface-deformation. The method for the strain field computation is described in section 6.1 and the resulting strain field model is provided in the section 6.2.

6.1 Computation of the strain field

The computation of the strain field is performed by the method described by Calais (2010). This method relies on the following assumptions:

- Local 2-dimentional Cartesian frame (horizontal components only);
- Infinitely small displacement (stations (or grid point) separated by distance in *km* level have velocities in *mm/a* level).

For the one-dimensional case the strain can be illustrated as follows (Figure 37). Under the applied force P , the solid rod will elongate and the points A and B will be displaced.

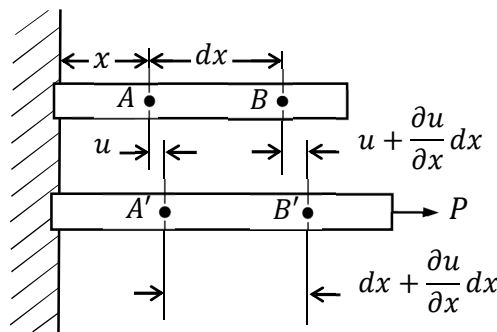


Figure 37. Strain. One-dimensional case. Example for a solid rod extended under an applied force P .

Considering the separation distance dx between points A and B to be small, their displacement can be described as follows:

$$u(x + dx) = u(x) + \frac{\partial u}{\partial x} dx \quad (23)$$

The strain is the ratio of distance change (between points A and B) to the original distance. Hence, the infinitesimal strain is a spatial gradient of the displacement:

$$e_x = \frac{A'B' - AB}{AB} = \frac{\left(dx + \frac{\partial u}{\partial x} dx \right) - dx}{dx} = \frac{\partial u}{\partial x} \quad (24)$$

This method can be applied to the station velocities for the two-dimensional case. Thus, the relative station velocities are referred as the displacement δX per unit time-interval (i.e. one year). Hence, the unit of a strain (deformation) is *strain/a*.

Similarly to the eq. (23), the velocity v of two points separated by a distance δX can be expressed as a function of the position X :

$$v(X + \delta X) = v(X) + \frac{\partial v}{\partial X} \delta X \quad (25)$$

where δX – is a separation distance;

$\frac{\partial v}{\partial X}$ – is a velocity gradient.

For two components (x and y), the eq. (25) becomes:

$$\begin{cases} v_x(X + \delta X) = v_x(X) + \frac{\partial v_x}{\partial x} \delta x + \frac{\partial v_x}{\partial y} \delta y \\ v_y(X + \delta X) = v_y(X) + \frac{\partial v_y}{\partial x} \delta x + \frac{\partial v_y}{\partial y} \delta y \end{cases} \quad (26)$$

where $X = \begin{bmatrix} x \\ y \end{bmatrix}$ – is a vector of coordinates;

$\delta X = \begin{bmatrix} \delta x \\ \delta y \end{bmatrix}$ – is a vector of separation distance between two points.

The velocity gradient tensor is a matrix, which elements of which are the spatial derivatives. Therefore, eq. (25) and (26) with velocity gradient tensor ∇V can be rewritten as:

$$v(X + \delta X) = v(X) + \nabla V \delta X, \quad \text{with } \nabla V = \begin{bmatrix} \frac{\partial v_x}{\partial x} & \frac{\partial v_x}{\partial y} \\ \frac{\partial v_y}{\partial x} & \frac{\partial v_y}{\partial y} \end{bmatrix} \quad (27)$$

Given two sites (i and j) separated by the distance δX , eq. (27) becomes:

$$v_i - v_j = v_{ij} = \nabla V \delta X \quad (28)$$

with $v_i = v(X + \delta X)$;

$v_j = v(X)$.

For three stations (where, the point 1 is a reference), the eq. (28) becomes in matrix form:

$$\mathbf{V} = \mathbf{AF} \quad (29)$$

with

$$\begin{bmatrix} v_{x_{12}} \\ v_{y_{12}} \\ v_{x_{13}} \\ v_{y_{13}} \end{bmatrix} = \begin{bmatrix} x_{12} & y_{12} & 0 & 0 \\ 0 & 0 & x_{12} & y_{12} \\ x_{13} & y_{13} & 0 & 0 \\ 0 & 0 & x_{13} & y_{13} \end{bmatrix} \begin{bmatrix} \partial v_x / \partial x \\ \partial v_x / \partial y \\ \partial v_y / \partial x \\ \partial v_y / \partial y \end{bmatrix} \quad (30)$$

where \mathbf{V} – is the vector of observations (velocity differences between stations);

\mathbf{A} – is the design matrix (position differences);

\mathbf{F} – is the vector of velocity gradients.

The least-squares adjustment solution of eq. (29) gives:

$$\mathbf{F} = (\mathbf{A}^T \mathbf{C}_v^{-1} \mathbf{A})^{-1} \mathbf{A}^T \mathbf{C}_v^{-1} \mathbf{V} \quad (31)$$

where \mathbf{C}_v^{-1} – is a weighting matrix.

At the strain was computed from the interpolated results and the estimated precision of the surface-deformation was relatively homogeneous for adjacent grid points (see Figure 36), the covariance matrix was assumed to be an identity matrix, $\mathbf{C}_v^{-1} = \mathbf{I}$, which simplifies the process.

The strain rate and rotation tensor are defined as follows:

$$\nabla \mathbf{V} = \frac{1}{2} [\nabla \mathbf{V} + \nabla \mathbf{V}^T] + \frac{1}{2} [\nabla \mathbf{V} - \nabla \mathbf{V}^T] \quad (32)$$

According to the tensor theory, a second-rank tensor can be decomposed into a symmetric (strain rate \mathbf{E}) and anti-symmetric (rigid rotation \mathbf{W}) tensor. In extended form, eq. (32) may be written as:

$$\nabla \mathbf{V} = \begin{bmatrix} \frac{\partial v_x}{\partial x} & \frac{1}{2} \left(\frac{\partial v_x}{\partial y} + \frac{\partial v_y}{\partial x} \right) \\ \frac{1}{2} \left(\frac{\partial v_x}{\partial y} + \frac{\partial v_y}{\partial x} \right) & \frac{\partial v_y}{\partial y} \end{bmatrix} + \begin{bmatrix} 0 & \frac{1}{2} \left(\frac{\partial v_x}{\partial y} - \frac{\partial v_y}{\partial x} \right) \\ -\frac{1}{2} \left(\frac{\partial v_x}{\partial y} - \frac{\partial v_y}{\partial x} \right) & 0 \end{bmatrix} \quad (33)$$

or

$$\nabla \mathbf{V} = \begin{bmatrix} e_{xx} & e_{xy} \\ e_{xy} & e_{yy} \end{bmatrix} + \begin{bmatrix} 0 & \omega \\ -\omega & 0 \end{bmatrix} = \mathbf{E} + \mathbf{W} \quad (34)$$

The tensor is independent of the coordinate system. To estimate the principal strain components $e_{1,2}$, the reference system must be rotated in such way that the shear strain e_{xy} becomes equal to zero. This is done by the diagonalization of the strain rate tensor \mathbf{E} . The estimated eigenvalues are equal to the principal strain rates and the eigenvectors are the principal axes of strain rate tensor. By convention, the positive strain is defined as an extension:

$$\det(\mathbf{E} - \lambda \mathbf{I}) = 0 \quad (35)$$

$$\det \begin{bmatrix} e_{xx} - \lambda & e_{xy} \\ e_{xy} & e_{yy} - \lambda \end{bmatrix} = 0 \quad (36)$$

Solving eq. (36), the eigenvalues λ are equal to the principal strain components $e_{1,2}$:

$$\lambda = e_{1,2} = \frac{e_{xx} - e_{yy}}{2} \pm \sqrt{\left(\frac{e_{xx} - e_{yy}}{2}\right)^2 + e_{xy}^2} \quad (37)$$

The direction θ of the e_1 component, (direction of e_2 is orthogonal to the direction of e_1) is given by:

$$\tan 2\theta = \frac{2e_{xy}}{e_{xx} - e_{yy}} \quad (38)$$

The maximum shear strain $e_{xy,max}$ is defined as follows:

$$e_{xy,max} = \sqrt{\left(\frac{e_{xx} - e_{yy}}{2}\right)^2 + e_{xy}^2} \quad (39)$$

While the maximum shear strain angle θ_s ($\theta_s = \theta \pm 45^\circ$) is defined by:

$$\tan 2\theta_s = \frac{e_{yy} - e_{xx}}{2e_{xy}} \quad (40)$$

The implementation on the strain computation was made using the deformation field (that was determined over the regular grid with 0.25° spacing interval (see sections 5.2 and 5.3). Figure 38 illustrates the scheme for the estimation of the strain using eq. (30) between tree points. Here, the point 1 was a reference point and the 4th corner point was not used. The estimated strain components were referred to the center of the grid cell. This procedure was applied to the entire grid of the deformation field on cell-by-cell basis. The resulting strain field is provided in the section 6.2.

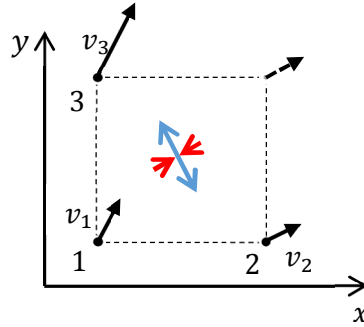


Figure 38. Example of strain estimation over a regular grid. Black arrows represent the deformation field.

6.2 Results of the strain field computation

The results of the strain (in fact, strain rate) field computation are illustrated in the Figure 39. The computation of the strain field assumes very small deformation rates (at mm/a level) over large distances (in km level) between grid points. The small-scale effects (e.g. slow landslides, local subsidence, ground water use, etc.) are revealed due to a large local variation of the velocity (more than $0.3 mm/a$) of neighboring points and due to the dense grid (0.25° spacing) of the deformation field. The important information of the strain field is the large-scale features (e.g. surface-deformation, mountain building, etc.) (Sanchez and Drewes, 2016). The areas with large strain are often seismically active (e.g. the Northern Italy).

Along with the principal strain components (compression and dilation) shown with arrows on the Figure 39, the first strain invariant (sum of strain components) is also shown as a color-coded overlay. Additionally, the strain invariant is spatially filtered by the median filter with a diameter of $100 km$. This filter size allows to remove the high spatial frequency noise and short-scale local effects.

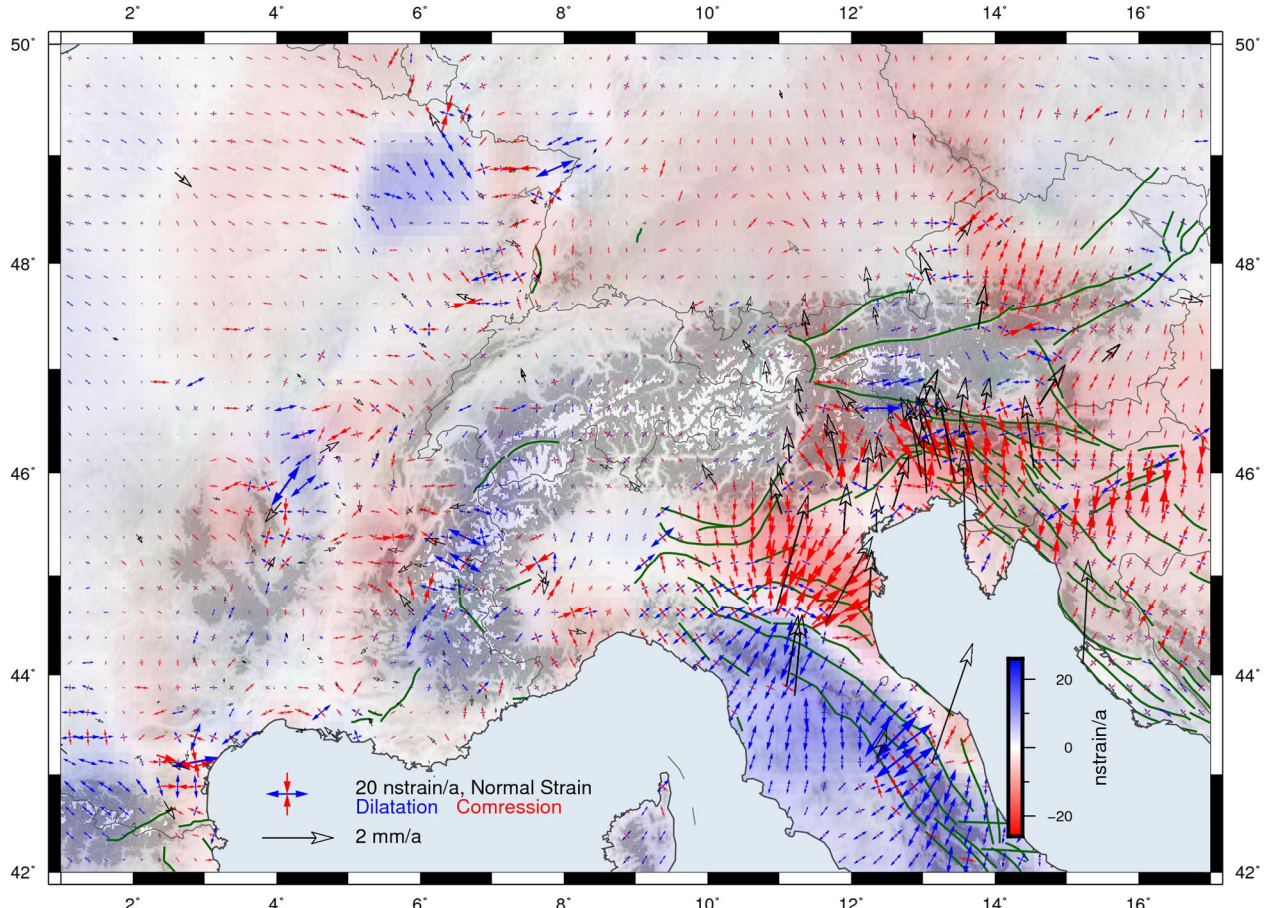


Figure 39. Principal strain. Blue shades - dilatation, red shades - compression. Black arrows represent the horizontal velocity field from the GNSS. Dark-green lines are the tectonic faults (Source: <http://diss.rm.ingv.it/share-edsf/>). The topography is taken from the ETOPO1 model (Source: <https://www.ngdc.noaa.gov/mgg/global/global.html>).

Around the Alpine mountains, a compression with a magnitude in the range of 5-10 $nstrain/a$ is observed (Figure 39). The highest compression rate of approximately -20 $nstrain/a$ is observed on the flat part of Northern Italy, where the Adriatic micro-plate collides with the Eurasian plate forming the Alps. The central part of the Alps does not reveal a significant strain due to the low coverage of GNSS stations and the smoothly interpolated deformation field model. Nevertheless, this picture is derived with six stations only. Only an improved coverage with more GNSS sites would improve the resolution.

Along the centerline of the French Alps, a lateral dilatation of about 10 $nstrain/a$ is observed (Figure 39). Those values are in agreement with Calais et al. (2002) and Sue et al. (2007). In the Austrian Alps, a dilatation of 10-20 $nstrain/a$ is revealed alongside the tectonic faults. The largest dilatation rate of nearly 25 $nstrain/a$ is observed in the Apennines. Even a low-station-coverage at the Pannonian microplate (see Chapter 4), a compressional strain of about 10-20 $nstrain/a$ is observed.

Another component of the strain is the shear strain, it is illustrated in Figure 40. It shows how separate segments of the surface-crust slide along each other.

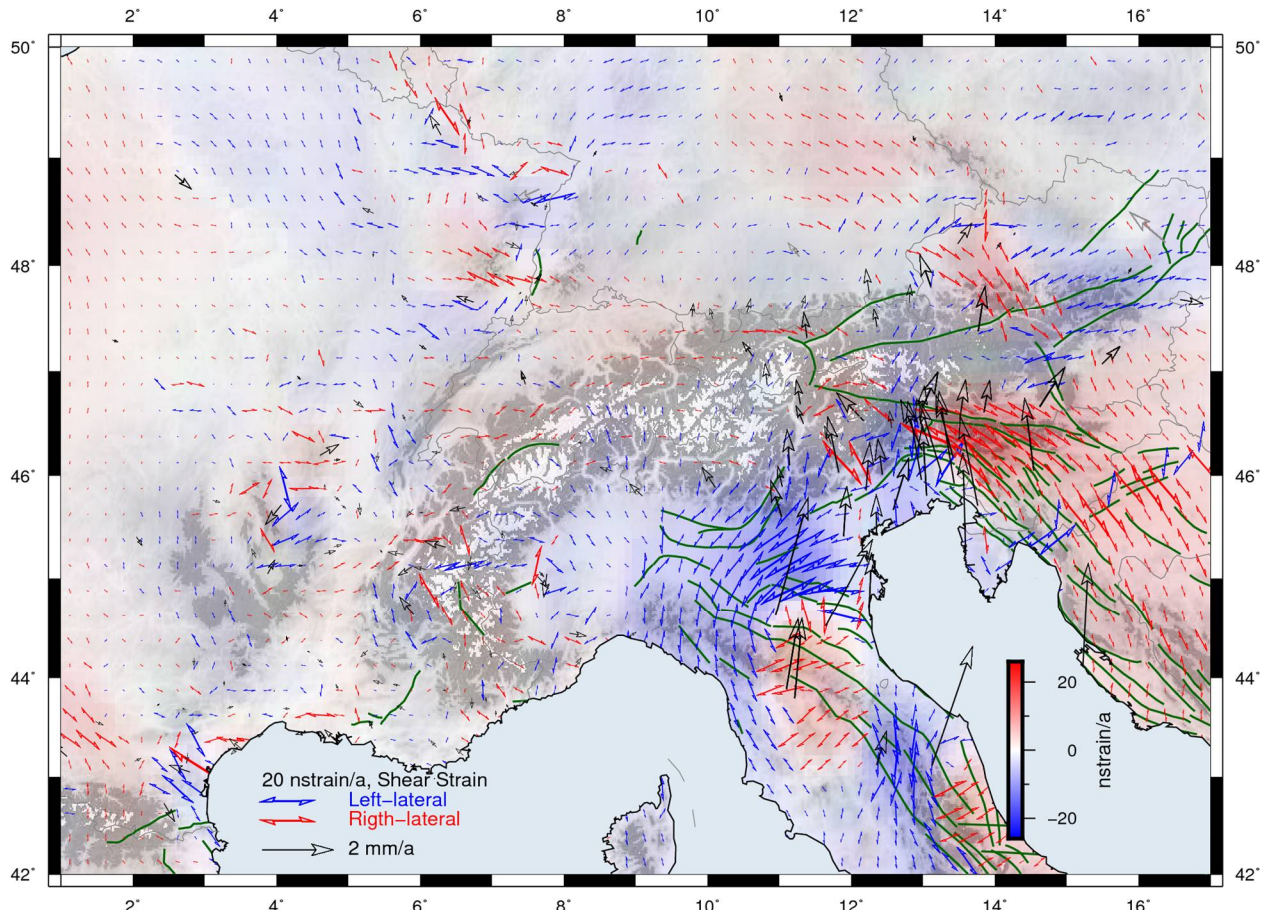


Figure 40. Shear strain. Blue and red shades represent the left-lateral and right-lateral shear, respectively. For illustration purpose, the left-lateral shear considered as negative and the right-lateral as positive. The black arrows represent the horizontal velocity field. Dark-green lines are the tectonic faults (Source: <http://diss.rm.ingv.it/share-edsf/>). The topography is taken from the ETOPO1 model (Source: <https://www.ngdc.noaa.gov/mgg/global/global.html>).

Strain field

The largest shear of about 20 $nstrain/a$ is observed in the southeastern part of the Alps. The sharp boundaries between the left-lateral and right-lateral shear zones and a ‘calm’ area reveal the triple-junction (Möller et al., 2011) between the Eurasian, the Adriatic and the Pannonia plates. According to Brückl and Hammer (2014), the approximate location of the triple junction is 46.6°N and 13.7°E, which is well correlated with the computed strain model (Figure 40).

The region of the Apennines has a poor network coverage to provide a reliable result; however, this is a highly active seismic region. The Western Alps and surroundings do not reveal any specific pattern of the shear strain. The Dinarides, that also have a sparse network density, show the compressional strain rate of about 10-20 $nstrain/a$ which is characterized by a right-lateral shear.

The resulting principal and shear strain fields show that the main tectonic activity is ongoing on the plate boundaries. The Eastern France with relatively network coverage shows small local variations in the strain components in a range of 5-10 $nstrain/a$. Locally, near the Pyrenees, near the Massif Central, and along the Rhine river enlarged strain values of about 20 $nstrain/a$ are observed. The better resolution of the strain field requires a denser coverage of observations (GNSS stations).

Validation of the strain field estimated in this study can be done by comparison with external studies. The advantage of the strain field, that it is computed using the relative velocities (see eq. (30)). Thus, the possibility of the incorrect plate motion removal is not a concern. However, the strain is often computed between stations, while in this study it is computed between grid points. For instance, Calais et al. (2002) have detected the same dilatation along the Central Alps at a strain rate of 2-3 $nstrain/a$, while in this study the rates are approximately 10-15 $nstrain/a$. This is mainly due to denser network coverage in this study, than in the network studied by Calais et al. (2002).

Based on a dense network covering the Swiss and Central Alps, Tesauro et al. (2006) determined compressional strain rates of about 5-10 $nstrain/a$ in the northwest direction. In this study, it was not possible to estimate any signal along this region, as the station coverage is very poor along the Central Alps.

In the studies of Caporali et al. (2009) and by Serpelloni et al. (2005, 2006), a dense GNSS network in Italy was used and a compressional strain rate of 20-30 $nstrain/a$ in the Friuli region was estimated. Similar dilatation strain rates along the Apennines were found. Those values are in agreement with this study (see Figure 38).

7 Vertical surface-deformation field

The vertical surface-deformation field is computed by the method of LSC and refined using kriging interpolation (Schwanghart and Kuhn, 2010; Niemeier, 2008). The procedure for the estimation of the vertical deformation field is similar to the procedure applied for the estimation of the horizontal surface-deformation field (see sections 5.2 and 5.3). In case of the vertical velocity field, the number of outliers was larger.

In general, there are three main components for mountain uplift: the plate tectonics, glacial isostatic adjustment (GIA) and erosion. Figure 41 illustrates those effects on the mountain building process.

The plate tectonics is triggered by the deep-seated processes in the Earth mantle. The Alpine mountain belt is a contractional orogen, it is created by collision of the Eurasian plate and Adriatic microplate (Mey et al., 2016).

Deglaciation is the loss of the ice masses. Therefore, the loading of the mountain is reduced, causing an isostatic uplift of the mountains. This process may be understood as a visco-elastic rebound ongoing since the last glacial maximum (LGM), dated as approximately 22,000 years ago.

The erosion, at some point, is similar to the deglaciation process, but it is much slower (geological time-scale) and the eroded rock masses are redistributed to the surroundings with lower elevation. Due to erosion, the rock masses are removed from the surface of the mountains, then they are transported by rivers, glaciers and wind and finally, they are deposited in the major delta valleys and sedimentary basins. In the mountains, this causes the bedrock uplift and surface height lowering. While at the surrounding regions, it causes the bedrock subsidence and regional surface height increase due to accumulation of sediment layers (Nocquet et al., 2016).

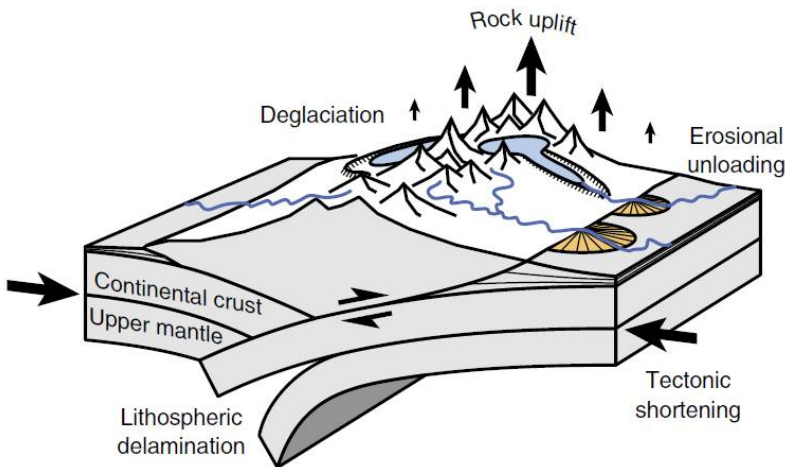


Figure 41. Processes contributing to rock uplift in a contractional orogen. (source: May et al., 2016).

For the estimation of the continuous vertical surface-deformation field, two interpolation methods were applied. At first, the deformation field was interpolated to a uniform grid with 0.25° spacing using LSC. For the estimation of the vertical deformation at grid points the velocities of stations within

250 km radius were used. If the local network coverage was insufficient, the nearest 10 stations were used. This is mainly applied to the outer part around the Alpine mountain belt and it would be equal if the size of ROI is increased to about 400-500 km. In a second step, kriging approach was applied to produce a smooth interpolation. In this case, the grid size was delimited to 0.1°.

In the mountain regions, landslides may occur. To monitor and predict possible landslides the GNSS observations are used as well. For instance, in the Italian Alps several stations (e.g. ACCE, AGNE, CLAP, CARZ, DEVE, OATO, PARO, SOND) of the studied network are explicitly located at unstable areas where landslides may occur. Even without a-priori knowledge, those stations are detected with slow downhill motion: the subsidence and horizontal velocity direction are in agreement with the local topography. For instance, station CLAP (Clapiere) installed on the side of the hill, which is gradually sliding. Other cases for local subsidence could be due to tunnel constructions (e.g. WIEN (Wien)), excavation of natural deposits, settling of buildings' foundation (e.g. CHMX (Chamonix)), ground water use, earthquakes, etc. (see Figure 22). The local vertical uplift outliers do not occur as often as the subsidence outliers. Usually, the uplift outliers are due to earthquakes (e.g. BOLG (Bologna) is excluded from combination due to strong nonlinearity of the time-series causing the frequent velocity changes (see Figure 13)). In addition, for the reliable estimation of the vertical velocity component, the time-interval of observation should be at least 3-4 years without equipment change or discontinuities (see Figure 23). A shorter observation interval is usually insufficient for reliable estimation of the vertical station velocity. After analyzing the vertical residual components, equipment changes often cause a small bias (in mm level) in the station position time-series, even with available information on the antenna patterns and antenna eccentricity used for corrections.

The vertical surface-deformation illustrated in Figure 42 shows the vertical motion in the Alps with a magnitude approximately 1-2 mm/a. The several spots located in the central belt show an uplift in the range of 2-2.5 mm/a. It is very likely, that the complete central Alpine belt is raising at rate of approximately 2.5 mm/a. Among the stations located in the mountain regions, it is observed that the stations located on the top (or at least at upper part) of the mountains (e.g. VERN (Vernagtferner), FDOS (Fort Dossaccio)) show higher uplift rates than stations located at the foot of the mountains or in the canyons (or moraines) between the mountains.

In the current study, the eastern part of the Austrian Alps has a low network coverage. Thus, the result at this zone presents a larger uncertainty, than the dense covered areas (e.g. the French Alps). In general, the results are in agreement with the recent studies of local GNSS networks in France (Nocquet et al., 2016) and in the Swiss Alps (Egli et al., 2007; Brockmann et al., 2014). In the study by Nocquet et al. (2016) the RENAG and ORPHEON GNSS networks were mainly used for the analysis along with the determination of contribution to the vertical uplift for each component (deglaciation, erosion and tectonics). In the aforementioned studies in the Swiss Alps, the analysis of GNSS data was combined with leveling measurements.

In Figure 42, it is possible to observe the subsidence zones: in Italy near Venice and Ferrara, and in France near Marseille, both approximately with rate of -1.5 mm/a. In those areas, the local topography

is flat, and the terrain has a smooth transition into a shallow ocean. The subsidence at those two areas agrees with the results provided by the coastal GNSS project, SONEL (<http://www.sonel.org/>, Santamaría-Gómez et al., 2012). The network SONEL combines the results from tide-gauges, GNSS, DORIS (Doppler Orbitography and Radiopositioning Integrated by Satellite), leveling, satellite-altimetry, etc. to perform studies at coastal areas.

Stations located at basins of large rivers are often affected by local subsidence, this is apparently due to loading effect of accumulated sedimentation. This is probably the reason for the local subsidence zone, identified in the valley of Eastern France near the boundary of Switzerland and Germany.

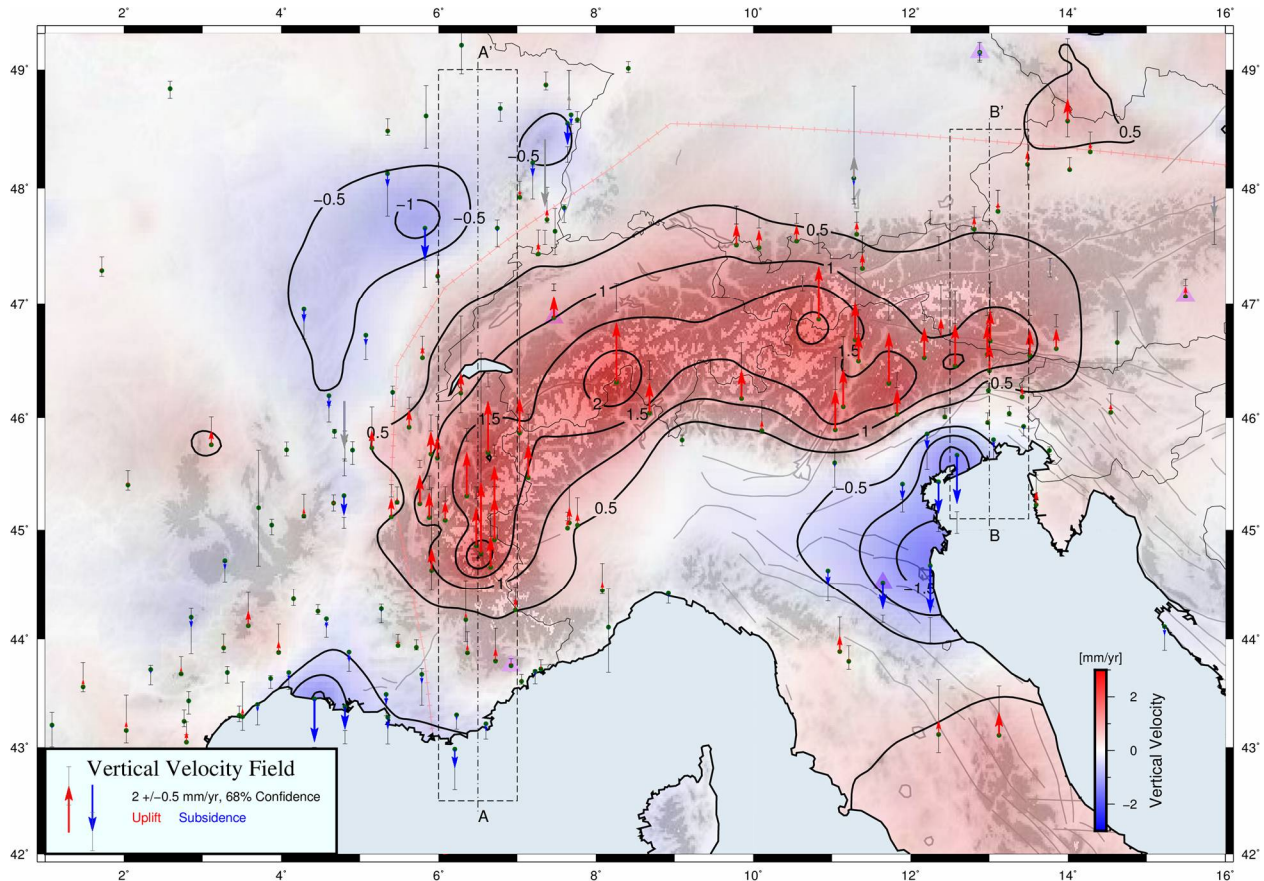


Figure 42. Vertical deformation model based on the station velocities directly. Station velocities are shown with arrows.

The precision of the vertical velocity field (Figure 43) derived from GNSS observations is usually worse than for the horizontal velocity field (Figure 36) due to the coupling with uncertainty sources for the height component like: phase ambiguities, clocks, antenna offsets, biases, atmosphere parameters etc. In practice, it is observed, that even using antenna PCV corrections is insufficient to fully absorb (to resolve) discontinuities in station time-series. The discontinuities caused by an antenna/radom change often propagate into the time-series of neighboring stations due to tight constraints.

The stations with good continuous operation, over 8-12 years, (e.g. station provided by EPN, FReDNet networks) have a formal error of the velocity in the range of 0.1-0.2 mm/a. The velocities

of stations from RENAG networks have a larger uncertainty, approximately $0.3\text{-}0.5 \text{ mm/a}$, due to shorter observation periods (around 5-7 years).

Figure 43 illustrates the estimated precision of the vertical surface-deformation field. It was estimated using the LSC method applying eq. (18). The precision of the estimated vertical surface-deformation shows the dependency of the velocity variation between neighboring stations. At the borders (outside of the Alp orogen and the Adriatics) the estimated precision is very optimistic, less than 0.1 mm/a . On the other hand, the Po plane (with the poor network coverage) and the Eastern Alps show a large uncertainty of approximately $0.5\text{-}0.8 \text{ mm/a}$. The estimated uncertainty of vertical surface-deformation field in the Alpine region, excluding the most eastern part, show formal error of about $0.4\text{-}0.6 \text{ mm/a}$.

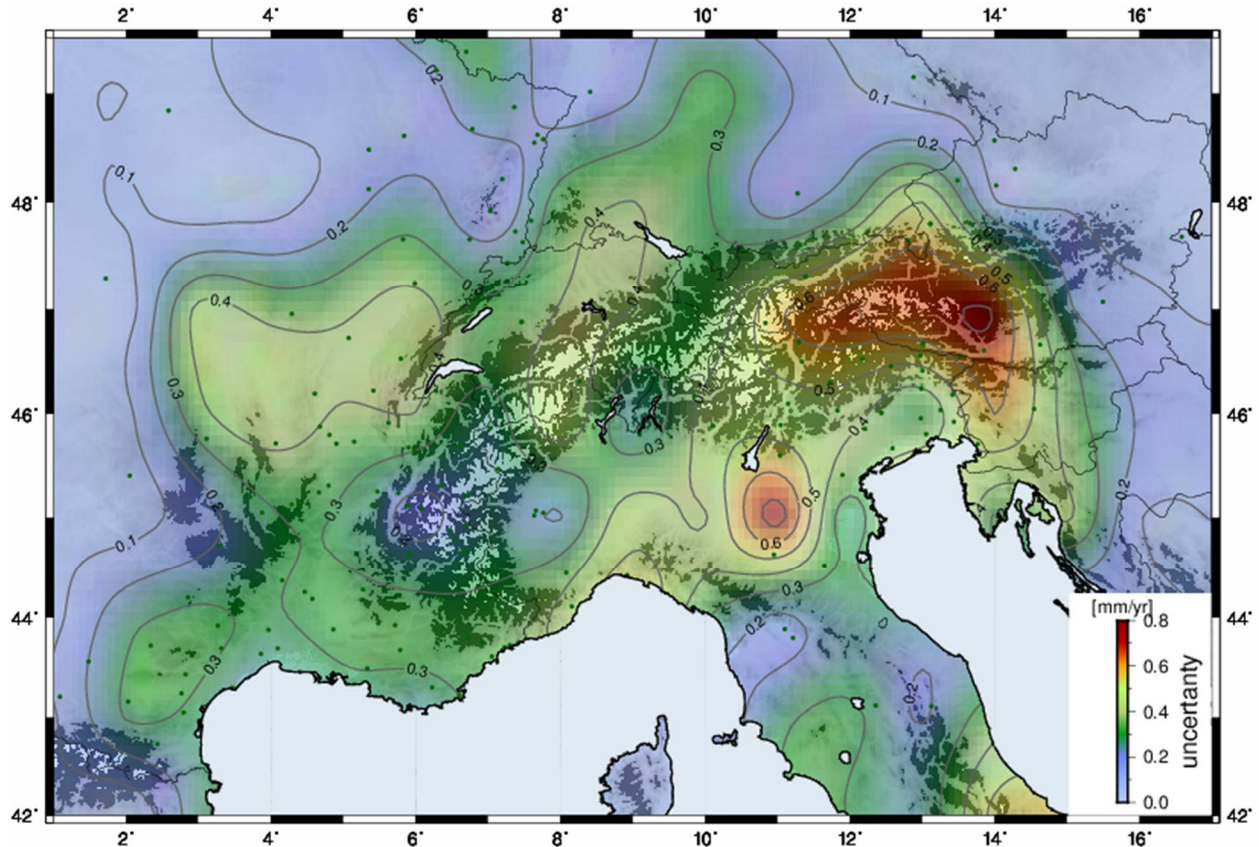


Figure 43. Estimated precision of vertical velocity field. The green dots are the GNSS sites.

To validate these results, an alternative procedure is used for the estimation of the vertical surface deformation model. This procedure is based on splitting the total observation signal in a trend function and a stochastic signal. The results are presented in the section 7.1

Observing the resulting vertical velocity field of the valley located to the west from the Alps (French region) (Figure 22 or Figure 42), it is possible to notice, that the variation of the estimated station velocities is less than 0.2 mm/a , while the estimated precision of vertical velocities is approximately $0.3\text{-}0.4 \text{ mm/a}$. This leads to the conclusion that the estimated scale factor for the precision of the

vertical velocity component (see section 4.1) can be validated from the variation of the station velocities themselves. Thus, the scale factor for vertical velocities can be considered as slightly oversized.

In the study performed by Serpelloni et al. (2013), the network coverage in the Alpine region is similar to this study, but much denser in Italy and the resulting vertical velocity field is similar. However, for the Eastern Alps, the vertical velocity field by Serpelloni shows a subsidence, while in this study an uplift is identified there (Figure 42).

From the results of LSC in both, vertical and horizontal components, a correlation with the local topography is observed. In order to illustrate this, the Figure 44 shows two cross-section profiles along 6.5°E and 13°E meridians crossing the Alps. Width of the cross-section is 1° (Figure 42). For both profiles, the vertical surface-deformation component shows a good positive correlation with the local topography. The mean topography (green line) is smoothed by 5 *arc-minutes* moving average.

In the Eastern Alps, one can see that the vertical velocity is higher in the southern part, than in northern one. The north component of the velocity along the 13°E meridian captures the plate boundary region, where the Adria micro-plate collides with the European plate. A rather strong velocity gradient of nearly 2 mm/a over the 500 km span in the Friuli region leads to the large generated stress (large compressional strain component is observed in the Figure 39), which is released with frequent earthquakes.

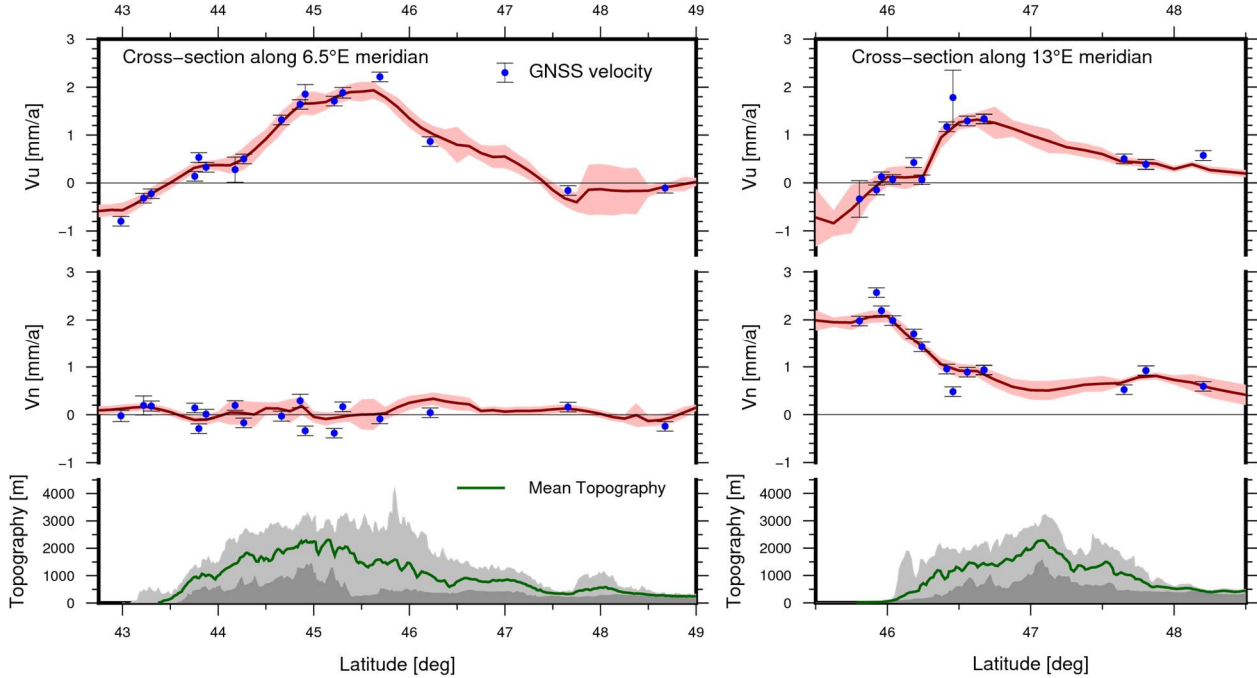


Figure 44. Cross-section profiles of the deformation field and local topography at the Western and Eastern Alps. The blue dots with error bar are the observed station velocities with 1-sigma (68% confidence). The solid red lines represents vertical and north deformation profiles with their uncertainty. The profiles have width of 1° . Mean topography is shown by the green line, maximum and minimum elevation are shaded with the gray color. The mean topography profile is additionally smoothed by 5 *arc-minute* moving average.

The vertical surface-deformation field shown in Figure 42 was estimated without application on any trend function. Moreover, the spatial distribution pattern of the estimated deformation (Figure 43) seems to be misleading. It has improved accuracy at the boundaries, then at the densely-covered areas. As an alternative, another surface-deformation field with applied trend function was estimated in the section 7.1.

7.1 Alternative solution for a vertical surface-deformation field.

An alternative solution for the vertical deformation field is provided in Figure 45. In this solution, the trend function (Figure 45c) was additionally estimated using the eq. (19). Per definition (eq. (14)), a trend (large-scale variation) function is well distinguished from the measurements (station velocities) (see Figure 32). The difference between the actual measurements and the trend function comprises the stochastic signal (short-scale variation) and noise.

The estimation of the trend and the stochastic components is done sequentially by the LSC method. Inhomogeneous isotropic covariance functions (of the form in eq. (13)) were used for both the trend and the stochastic component. The correlation length was selected to be 200 *km* for the trend function and 100 *km* for the stochastic signal. Afterwards, the estimated trend (Figure 45c) was removed from the measurements.

The stochastic component (Figure 45e) shows a variation one order of magnitude lower than the values for the trend. The precision of the signal and the trend function were estimated using eq. (21) and (22) and the precision of the surface-deformation is the sum of these two estimates. The precision of the stochastic signal (Figure 45f) is approximately 0.2 *mm/a*. It presents values in a range of 0.25-0.35 *mm/a* at the margins of the studied area. These values are much more reliable than those estimated with the previous method (compare Figure 42 and Figure 45b). The estimated precision of the trend function (Figure 45d) near to the stations is better than 0.2 *mm/a*. Locally, in the Po plane and the Apennines the uncertainty is larger due to a lack of stations. The difference in precision of signal and trend function is due to different ROI sizes (e.g. 100 and 200 *km* accordingly). The large uncertainty of approximately 0.5 *mm/a* is observed in the Po plane due to insufficient observations and in the Western Alps due to the inhomogeneous station velocities. In general, the estimated precision of the vertical surface-deformation is about 0.4 *mm/a* (Figure 45b).

Comparing the two vertical surface-deformation field models (Figure 42 and Figure 45a), it is possible to observe only minor differences and the results itself are in agreement. The principal difference between those models is their estimated precision (Figure 43 and Figure 45b). In the second model, the assessment of the precision is more realistic and has a more reliable spatial distribution. The estimated error is larger in the spare covered areas (e.g. Po plane, Apennines) and at the margin areas.

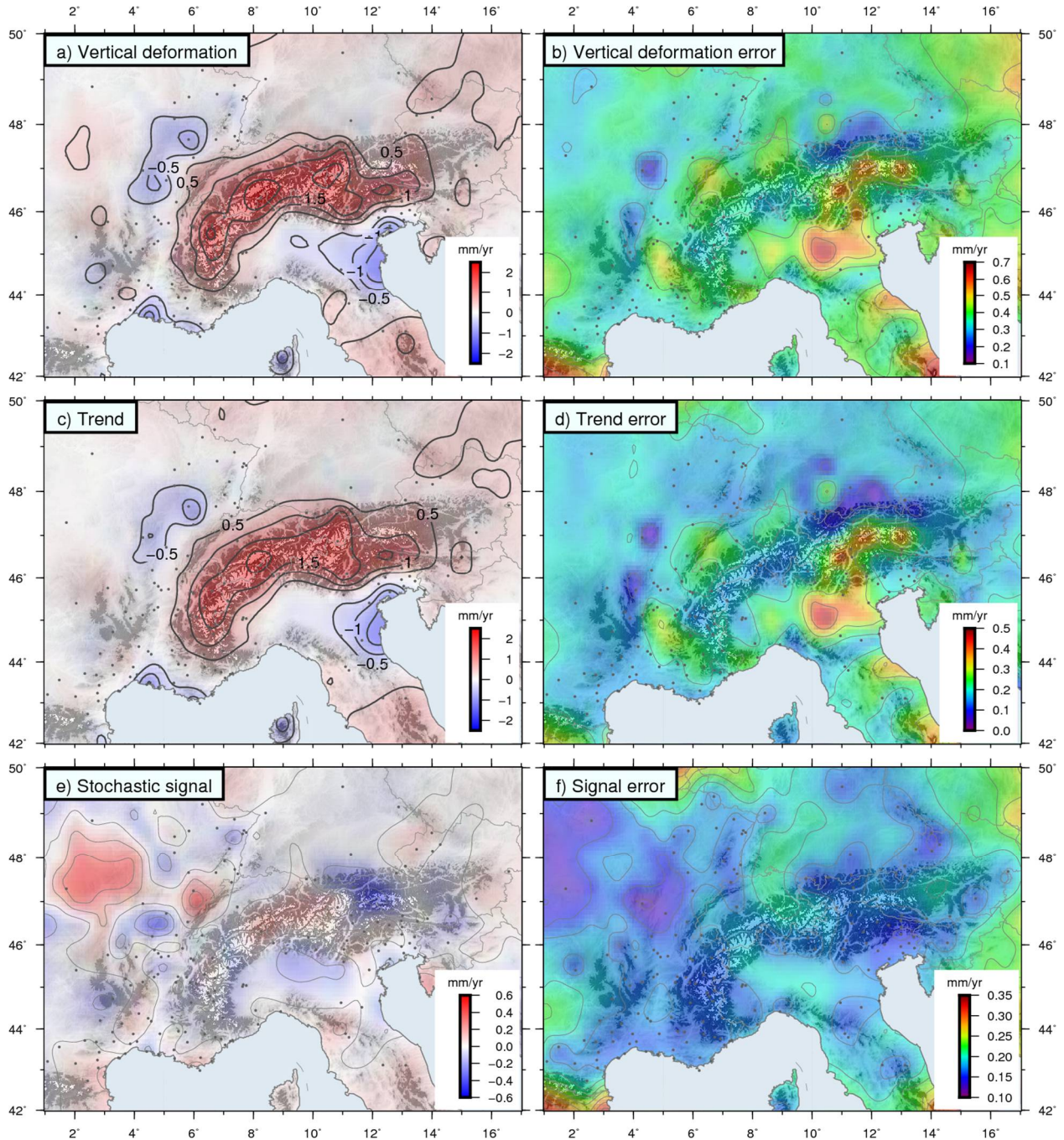


Figure 45. Vertical surface-deformation model based on the separate analysis of the trend function and a stochastic signal. The topography is shown to illustrate the results in order to determine the dependency to the local tectonic/geological features. The dots are the GNSS stations. (a) Vertical surface-deformation field. (b) Estimated precision of the vertical surface-deformation field. (c) The empirically estimated trend function of vertical surface-deformation field. (d) The estimated precision of the trend function. (e) The stochastic signal. (f) The estimated precision of the stochastic signal.

8 Conclusions

Based on a GNSS (GPS and GLONASS) network of 210 stations covering a period of 12.4 years a velocity field of the Alpine region was estimated. High-precision processing of the GNSS data follows the standards applied for the computation of the EUREF reference frame. Special care was given to the handling of the metadata, ambiguity resolution, clusterization, etc. for the daily processing. The advantage of the current study with respect to previous studies like Nocquet et al. (2016), Serpelloni et al. (2013), Caporali et al. (2009) that it covers the entire Alpine region and the processing network was performed by the double-difference technique.

The multi-year solution was estimated from the normal equation files using the minimum constrained condition. For that purpose, the set of most appropriate available IGB08 reference stations was determined. Along with multi-year combination, the residual time-series analysis was performed to identify discontinuities and resolve them. The velocities of the stations were determined from a time-series of a station positions. On a large time-span of observation (e.g. 12.4 years in the current study) inevitably occurs the discontinuities in the time-series, that strongly interfere at velocity determination process. The most of discontinuities in station position time-series were resolved using the available stations meta-data. The most of remaining discontinuities (i.e. more than 5 mm) were additionally identified and resolved for stations with good continuity of observations. The discontinuities are provided in the Annex B. The consistency of the multi-year solution was verified by the analysis of the station position time-series.

The precision of station velocities provided by least-squares adjustment was overestimated. Thus, the empirical estimation of scale factors (for East, North and Up components) was determined by analysis of the time-series. The estimated velocity field was determined with a precision of approximately 0.1-0.3 mm/a for the horizontal and approximately 0.2-0.5 mm/a for the vertical components, respectively. Those values are provided applying the variance scale factor.

The residual horizontal velocity field was computed using the empirically determined Euler pole for the Eurasian plate. The comparison of the estimated velocity field with three external studies leads to conclusion that the precision of estimated horizontal velocities is about 0.2 mm/a and precision of vertical velocities is approximately 0.3-0.5 mm/a. Those values indirectly show the validity of the empirically estimated variance scale factors.

The surface-deformation fields were estimated using the least-squares collocation method. The horizontal surface-deformation reveals the ongoing tectonic processes around the Adriatic microplate. The collision of the Eurasian plate and the Adriatic microplate is a main cause of the seismic activity in the Eastern Alps and Northern Italy. In the Eastern Alps a slow stretching (less than 0.5 mm/a along the EW axis) of the Alpine mountain belt along its longitudinal axis was determined. From the Western Alps to the Eastern Alps the continues increase of northward velocities from nearly zero to approximately 1.0 mm/a is observed.

The Central Alps show a northwestward velocity at less than 0.5 mm/a ; and the Western Alps move northeastwards at rate of about 1.0 mm/a . The Western Alps have a weak eastward velocity of less than 0.2 mm/a . The Western Alps can be characterized as ‘calm’ in terms of horizontal motion. Nevertheless, the dense GNSS network allowed to observe the week signal in the Western Alps and a counter clock-wise rotation of the Po plane along with the ‘inner’ concave part of the Western Alps. In general, the motion patterns are well segmented by some of the tectonic lines.

The estimated strain field helps to determine the collision behavior of the microplates at the Adriatic-Alpine region. The maximum compression strain rates of $20\text{--}25 \text{ nstrain/a}$ are revealed at the boundary of the Adriatic micro-plate and the Eurasian plate. The tensile strain at approximately 10 nstrain/a is locally observed in the middle of the Western Alps and at the Eastern Alps near the triple junction zone of the Eurasian plate with the Pannonian and the Adriatic microplates. The shear strain also reveals the boundaries of this triple junction. The comparison of the obtained strain rate field with external studies allows to quantify the precision of the strain rate field. For the densely-covered areas the precision is approximately within $\pm 5 \text{ nstrain/a}$.

The determined results of the continuous vertical surface-deformation model reveal the general uplift of the Alpine belt at a rate of $2\text{--}2.5 \text{ mm/a}$ with small variation of velocities along the longitudinal axis. The Western Alps provide stable and precise results of uplift at $2.5 \pm 0.3 \text{ mm/a}$. The velocity precision of this station is rather loose, but the time-series are relatively ‘stable’ and continuous. Even with the lower network coverage at the Central Alps the vertical deformation field has a good continuity with the Western Alps and with eastern part up to the Austrian boundary region. At the Eastern Alps, where mountains experience the complex deformation caused by multiple collision boundaries, the resulting vertical uplift show the transition of vertical velocity from 2.0 mm/a to almost zero uplift (at the far eastern corner of Alpine ridge).

Additionally, three local subsidence areas are observed. Two areas at coast regions reaching negative rates of $1.0\text{--}1.5 \text{ mm/a}$: at the Adriatic (e.g. near Venice) smoothly propagating to the Po plane; and in France, near Marseille. In both cases a subsidence occurs at flat terrain coastal areas with shallow ocean. Another local subsidence of approximately -0.5 mm/a is observed in the region to the north-west of Alps. This is likely due to accumulation of the sediments at river basins.

As possible future improvements of the results obtained in this study, I suggest: to use the redundant baselines between the possible reference stations; to refines the station meta-data for identifying further discontinuities; to exclude stations with bad continuity and short temporal coverage (since they are more likely introduce the additional noise/disturbance into the network); to densify the network, especially in the Swiss and Austrian Alps; to apply the VMF at the step of ambiguity-fixed solution estimation; and to switch the reference frame from the ITRF2008 (IGb08) to the latest ITRF2014 (Altamimi et al., 2016) frame.

Acknowledgment

I would like to express my very great appreciation to my research supervisors for their patient guidance, enthusiastic encouragement and useful critiques of this research work. Without their precious support, it would not be possible to conduct this research. I would like to offer my special thanks to Dr.-Ing. Christof Völksen for providing the deep insight into GNSS data processing and the critical evaluation of the results. I am particularly grateful for the supervision given by Dr.-Ing. Laura Sánchez in analysis of the large geodetic network and for dedication to this work. I wish to acknowledge the help provided by Prof. Dr.-Ing. habil. Florian Seitz and for the patience in this long-lasting research.

I would also like to extend my thanks to all personnel of the Projekt Erdmessung und Glaziologie and Deutsches Geodätisches Forschungsinstitut for their hosting and creating a warm working climate.

This master thesis is a final stage of the studies under the Master's Course in Earth Oriented Space Science and Technology (ESPACE) program at the Technical University of Munich (TUM) with the financial help provided by the German Academic Exchange Service (DAAD) scholarship. I wish to thank all the professors and coordinators who are involved into the collaboration of such wonderful study program, that exists only thanks to their own initiative.

The analysis of result and illustrations was performed using Matlab and Bash-shell (Linux). The time-series and maps were compiled with Generic Mapping Tools (GMT, Wessel et al., 2013) software, version 5.2 <http://gmt.soest.hawaii.edu/>. The Earth topography and bathymetry provided by ETOPO1 model, (source: <https://www.ngdc.noaa.gov/mgg/global/global.html>). (Amante and Eakins, 2009). The tectonic fault lines and subduction zones are provided by database <http://diss.rm.ingv.it/share-edsf/>. (Basili et al., 2013).

Bibliography

- Altamimi, Z., Collilieux X., Métivier L. 2011. ITRF2008: an improved solution of the international terrestrial reference frame. *J. Geod.* 85, pp. 457. doi:10.1007/s00190-011-0444-4.
- Altamimi, Z., Rebischung P., Métivier L., Xavier C. 2016. ITRF2014: A new release of the International Terrestrial Reference Frame modeling nonlinear station motions, *J. Geophys. Res. Solid Earth*, 121, pp. 6109-6131. doi:10.1002/2016JB013098.
- Amante C., Eakins B.W. 2016.ETOPO1 1 Arc-Minute Global Relief Model: Procedures, Data Sources and Analysis. NOAA Technical Memorandum NESDIS NGDC-24. National Geophysical Data Center, NOAA. doi:10.7289/V5C8276M
- Aoudia A., Amodio A., Troisi C., Manzino A., Luchetta A., Völksen C., Drewes H., Zivcic M., Van der Voerd J., Fosson J.P., Carraro C., Zampedri G., Walpersdorf A., Laffi R., Fioroni M., Barzaghi R., Sabadini R., Paselli L., Sguero D. 2007. ALPS GPSQUAKENET. Alpine Integrated GPS Network: Real-Time Monitoring and Master Model for Continental Deformation and Earthquake Hazard. Intergared III B Project –Alpine Space.
- Bada G., Horváth F., Dövényi P., Szafián P., Windhoffer G., Cloetingh S. 2007. Present-day stress field and tectonic inversion in the Pannonian basin. *Science Direct. Global and Planetary Change* 58, pp. 165–180.
- Basili R., Kastelic V., Demircioglu M. B., Garcia Moreno D., Nemser E. S., Petricca P., Sboras S. P., Besana-Ostman G. M., Cabral J., Camelbeeck T., Caputo R., Danciu L., Domac H., Fonseca J., García-Mayordomo J., Giardini D., Glavatovic B., Gulen L., Ince Y., Pavlides S., Sesetyan K., Tarabusi G., Tiberti M. M., Utkucu M., Valensise G., Vanneste K., Vilanova S., Wössner J. 2013. The European Database of Seismogenic Faults (EDSF) compiled in the framework of the Project SHARE. <http://diss.rm.ingv.it/share-edsf>. doi: 10.6092/INGV.IT-SHARE-EDSF.
- Bird P. 2003. An updated digital model of plate boundaries, *Geochem. Geophys. Geosyst.*, 4, 1027, doi:10.1029/2001GC000252, 3.
- Böhm J., Werl B., Schuh H. 2006. Troposphere mapping functions for GPS and very long baseline interferometry from European Centre for Medium-Range Weather Forecasts operational analysis data, *J. Geophys. Res.*, 111, B02406, doi:10.1029/2005JB003629.
- Bokelmann G., Qorbani E., Bianchi I. 2013. Seismic anisotropy and large-scale deformation of the Eastern Alps. *Science Direct. Earth and Planetary Science Letters* 383. pp. 1–6.
- Boucher C., Altamimi Z. 2011. Specifications for reference frame fixing in the analysis of a EUREF GPS campaign. Version 8.
- Brockmann E. 2016. Densifying Velocity Fields in Europe: Advantages of the classical Approach. Bundesamt für Landestopografie Swisstopo.
- Brockmann E., Ineichen D., Marti U., Schaer S., Schlatter A. 2014. Determination of the Swiss Alpine Uplift using GNSS and Levelling. Bundesamt für Landestopografie swisstopo.
- Brückle E., Hammer C. 2014. Eduard Suess' conception of the Alpine orogeny related to geophysical data and models. *Austrian J. of Earth Sciences*. Volume 107/1. Vienna.
- Bruyninx C., Habrich H., Kenyeres A., Söhne W., Stangl G., Völksen C. 2013. EUREF Permanent Network. International GNSS Service 2012 Technical Report, R. Dach and Y. Jean (eds), Astronomical Institute University of Bern, pp. 101-107, doi: 10.7892/boris.80303.

Bibliography

- Bruyninx C., Habrich H., Söhne W., Kenyeres A., Stangl G., Völksen C. 2012. Enhancement of the EUREF Permanent Network Services and Products "Geodesy for Planet Earth", IAG Symposia Series, Vol. 136, pp. 27-35, doi: 10.1007/978-3-642-20338-1_4.
- Calais E. 2010. Kinematics of the lithosphere from geodetic measurements. Strain analysis Lecture notes. Dept. of Earth and Atmospheric Sciences. Purdue University.
- Calais E., Nocquet J.-M., Jouanne F., Tardy M. 2002. Current strain regime in the Western Alps from continuous GPS measurements, 1996-2001. *Geology*.
- Caporali A., Aichhorn C., Barlik M., Becker M., Fejes I., Gerhatova L., Ghitau D., Grenerczy G., J. Hefty J., Krauss S., Medak D., Milev G., Mojzes M., Mulic M., Nardo A., Pesec P., Rus T., Simek J., Sledzinski J., Solaric M., Stangl G., Stopar B., Vespe F., Virag G. 2009. Surface kinematics in the Alpine–Carpathian–Dinaric and Balkan region inferred from a new multi-network GPS combination solution. *Tectonophysics* 474: pp. 295–321.
- Chen G., Herring T.A. 1997. Effects of atmospheric azimuthal asymmetry on the analysis of space geodetic data, *J. Geophys. Res.*, 102(B9): pp. 20489-20502, doi: 10.1029/97JB01739.
- Cuffaro M., Riguzzi F., Scrocca D., Antonioli F., Carminati E., Livani M., Doglioni C. 2010. On the geodynamics of the northern Adriatic plate. *Rend. Acc. Lincei* 21 (Suppl. 1): S253–S279. doi: 10.1007/s12210-010-0098-9.
- Dach, R., Hugentobler U., Frizez P., Meindl M. (Eds). 2007. Bernese GPS Software Version 5.0. User manual, Astronomical Institute, University of Bern.
- Dach, R., Lutz S., Walser P., Frizez P. (Eds). 2015. Bernese GNSS Software Version 5.2. User manual, Astronomical Institute, University of Bern, Bern Open Publishing. doi:10.7892/boris.72297; ISBN: 978-3-906813-05-9.
- Dow, J. M., Neilan R. E., Rizos C. 2009. The International GNSS Service in a changing landscape of Global Navigation Satellite Systems. *Journal of Geodesy*, 83(3–4): pp. 91–198. doi:10.1007/s00190-008-0300-3.
- Drewes H. 1982. A geodetic approach for the recovery of global kinematic plate parameters. DGFI, Munich, *Bull. Geod.* 56. pp. 70-79.
- Drewes H., Heidbach O. 2005. Deformation of the South American crust estimated from finite element and collocation methods. In: Sansò F (Ed.) *A Window on the Future of Geodesy*, IAG Symposia 128: pp. 544-549, Springer, doi: 10.1007/3-540-27432-4_92.
- Drewes H., Heidbach O. 2012. The 2009 horizontal velocity field for South America and the Caribbean. Kenyon S, Pacino MC, Marti U (Eds.), *Geodesy for Planet Earth*, IAG Symposia, 136: pp. 657-664, doi: 10.1007/978-3-642-20338-1_81.
- Egli R., Geiger A., Wiget A., Kahle H.-G. 2007. A modified least-squares collocation method for the determination of crustal deformation: first results in the Swiss Alps. *Geophys. J. Int.* 168, pp. 1–12.
- Grenerczy G., Kenyeres A., Frejes I. 2000. Present crustal movement and strain distribution in Central Europe inferred from GPS measurements. *J. of Geophysical Res.*, Vol. 105, No B9, pp. 21,835–21,842. Budapest.
- Grenerczy G., Stella G., Stein S., Kenyeres A. 2005. Tectonic implications of the GPS velocity field in the northern Adriatic region. *Geophysical Research Letters*, vol. 32, l16311, doi: 10.1029/2005gl022947.
- Haslinger C., Krauss S., Stangl G. 2007. The Intra-Plate Velocities of GPS Permanent Stations of the Eastern Alps. *Vermessung & Geoinformation*. pp. 66 – 72.
- Haslinger C., Stangle G. 2007. The First Austrian Velocity Field derived from GPS. Graz.
- Heidbach O., Drewes H. 2003. 3-D finite element model of major tectonic processes in the Eastern Mediterranean, *Geol. Soc. Spec. Publs.*, 212: pp. 261-274. doi: 10.1144/GSL.SP.2003.212.01.17.

- Herring T.A., King R.W., McClusky S.C. 2010. Introduction to GAMIT/GLOBK, Release 10.4, Massachusetts Institute of Technology. http://www-gpsg.mit.edu/~simon/gtgk/Intro_GG.pdf.
- Jiang G., Xu C., Wen Y., Xu X., Ding K., Wang J. 2014. Contemporary tectonic stressing rates of major strike-slip faults in the Tibetan Plateau from GPS observations using Least-Squares Collocation. *Tectonophysics*. 615-616, pp. 85-95.
- Jin S., Zhu W. 2004. A revision of the parameters of the NNR-NUVEL-1A plate velocity model. *Journal of Geodynamics* 38, pp. 85-92.
- Means W.D. 1979. Stress and Strain. Basic Concepts for Continuum Mechanics for Geologists. Springer-Verlag, New York.
- Métois M., D'Agostino N., Avallone A., Chamot-Rooke N., Rabaute A., Duni L., Kuka N., Koci R., Georgiev I. 2015. Insights on continental collisional processes from GPS data: Dynamics of the peri-Adriatic belts. *J. of Geophysical Research: Solid Earth*. AGU Publications. doi: 10.1002/2015JB012023.
- Mey J., Scherler D., Wickert A.D., Egholm D. L., Tesauro M., Schildgen T. F., Strecker M. R. 2016. Glacial isostatic uplift of the European Alps. *Nature Communications*. doi: 10.1038/ncomms13382.
- Mikhail E., Ackerman F. 1976. Observations and least squares. IEP-A Dun-Donnelley. New York.
- Möller G., Brückl E., Weber R. 2/2011. Active tectonic deformation at the transition from the European and Pannonian domain monitored by a local GNSS network. *Vermessung & Geoinformation*.
- Moritz H. 1973. Stepwise and Sequential Collocation. The Ohio State University. Sci. Rep. No. 10.
- Moritz H. 1972. Advanced Least-Squares Methods. The Ohio State University Research Foundation. Report No. 175.
- Moritz H. 1976. Covariance functions in Least-Squares Collocation. The Ohio State University. Rep. No. 240.
- Nguyen H.N., Vernant P., Mazzotti S., Khazaradze G., Asensio E. 2016. 3D GPS velocity field and its implications on the present-day post-orogenic deformation of the Western Alps and Pyrenees. *Solid Earth Discuss.*, doi: 10.5194/se 2016-78.
- Niemeier W. 2008. Ausgleichungrechnung. Statistische Auswertemethoden. 2 Aufgabe. de Gruyter Lehrbuch. Berlin.
- Nocquet, J.-M., Sue C., Walpersdorf A., Tran T., Lenôtre N., Vernant P., Cushing M., Jouanne F., Masson F., Baize S., Chéry J., van der Beek P. A. 2016. Present-day uplift of the western Alps. *Sci. Rep.* 6, 28404; doi:10.1038/srep28404.
- Ostini L., Dach R., Schaer, S., Hugentobler U. 2008. FODITS: A new tool of the Bernese GPS software. Bern.
- Pelzer H. 1985. Geodätische Netze in Landes- und Ingenieurvermessung II: Vorträge d. Kontaktstudiums / hrsg. von Hans Pelzer. Witter. Stuttgart.
- Petit G., Luzum B. (eds.). 2010. IERS Conventions (2010). (IERS Technical Note; 36) Frankfurt am Main: Verlag des Bundesamts für Kartographie und Geodäsie, 179 pp.
- Rebischung P., Griffiths J., Ray J., Schmid R., Collilieux X., Garayt B. 2011. IGS08: the IGS realization of ITRF2008. *GPS Solut.* 16: pp. 483–494. doi: 10.1007/s10291-011-0248-2.
- Rodriguez-Solano C. J., Hugentobler U., Steigenberger P., Lutz S. 2012. Impact of Earth radiation pressure on GPS position estimates. *Journal of Geodesy*, 86(5): pp. 309–317. doi: 10.1007/s00190-011-0517-4.
- Sánchez L., Drewes H. 2016. Crustal deformation and surface kinematics after the 2010 earthquakes in Latin America. *Journal of Geodynamics* 102, pp. 1-23, doi: 10.1016/j.jog.2016.06.005.
- Santamaría-Gómez A., Gravelle M., Collilieux X., Guichard M., Martin Miguez B., Tiphaneau P., Wöppelmann G. 2012. Mitigating the effects of vertical land motion in tide gauge records using a state-of-the-art GPS velocity field. *Global and Planetary Change*, Vol. 98-99, pp. 6-17.

Bibliography

- Schmid R., Dach R., Collilieux X., Jäggi A., Schmitz M., Dilssner F. 2016. Absolute IGS antenna phase center model igs08.atx: status and potential improvements. *J. Geod.* 90(4): pp. 343-364, Springer, doi: 10.1007/s00190-015-0876-3.
- Schmid R., Steigenberger P., Gendt G., Ge M., Rothacher M. 2007. Generation of a consistent absolute phase center correction model for GPS receiver and satellite antennas. *J. Geod.* 81(12), pp. 781-798, doi: 10.1007/s00190-007-0148-y.
- Schwanghart, W., Kuhn, N. J. 2010. TopoToolbox: a set of Matlab functions for topographic analysis. *Environmental Modelling & Software*, 25, pp. 770-781. doi: 10.1016/j.envsoft.2009.12.002.
- Seitz F., Herbert A., Franz L. 2014. Position measurements at five permanent GPS stations in the Bavarian Alps as part of the Geodetic Alpine Integrated Network (GAIN) of the ALPS-GPSQUAKENET project. Deutsches Geodätisches Forschungsinstitut, München, doi: 10.1594/PANGAEA.834193.
- Serpelloni E., Adziei M., Baldi P., Casula G. and Galvani A. 2005. Crustal velocity and strain-rate fields in Italy and surrounding regions: new results from the analysis of permanent and non-permanent GPS networks. *Geophys. J. Int.* 161, pp. 861–880. doi: 10.1111/j.1365-246X.2005.02618.x.
- Serpelloni E., Adziei M., Baldi P., Casula G., Galvani A. 2006. GPS measurement of active strains across the Apennines. *Annals of Geophysics*, Supplement to Vol. 49, N. 1.
- Serpelloni E., Faccenna C., Spada G., Dong D., and Williams S. D. P. 2013. Vertical GPS ground motion rates in the Euro-Mediterranean region: New evidence of velocity gradients at different spatial scales along the Nubia-Eurasia plate boundary, *J. Geophys. Res. Solid Earth*, 118, 6003–6024, doi: 10.1002/2013JB010102.
- Soler T., Chin M. 1985. On transformation of covariance matrices between local cartesian coordinate systems and commutative diagrams. NGS. NOAA. Rockville.
- Steigenberger, P., Böhm J., Tesmer V. 2009. Comparison of GMF/GPT with VMF1/ECMWF and implications for atmospheric loading. *Journal of Geodesy*, 83(10), pp. 943–951. doi: 10.1007/s00190-009-0311-8.
- Sue C., Delacou B., Champagnac J.D., Allanic C., Burkhard M. 2007. Aseismic deformation in the Alps: GPS vs. seismic strain quantification. *Terra Nova* 19, issue 3, pp. 182-188.
- Tesauro M., Hollenstein C., Egli R., Geiger A., Kahle H.G. 2006. Analysis of central western Europe deformation using GPS and seismic data. *Journal of Geodynamics* 42, pp. 194–209. Zurich. Elsevier.
- Umnig E., Brückl E., Maras J., Weber R. 2015. Monitoring Tectonic Processes in Eastern Austria based on GNSS-derived site velocities. *Vermessung & Geoinformation*. p. 198 – 207.
- Wessel, P., Smith W. H. F., Scharroo R., Luis J., Wobbe F. 2013. Generic Mapping Tools: Improved Version Released, *EOS Trans. AGU*, 94(45), pp. 409-410. doi: 10.1002/2013EO450001.

Annex A. Velocity field table

Residual horizontal velocities $V_{e,res}$ and $V_{n,res}$ are the residual station velocities after removal of the Eurasian plate motion using the Euler pole $\Omega(\varphi, \lambda, \omega) = [55.95^\circ, -97.41^\circ, 0.2636^\circ/Ma]^T$ (see section 4.2.1). The time-period t_{obs} is the time-spam of useful observations used for the velocity determination and is not strictly the period between first and last epochs.

Site	Long. deg	Lat. deg	Height m	$V_{e,res}$ mm/a	σ_{V_e}	$V_{n,res}$ mm/a	σ_{V_n}	V_u mm/a	σ_{V_u}	Start	End	t_{obs} year
ACOM	13.51	46.55	1774.7	0.16 ± 0.07		1.09 ± 0.05		1.08 ± 0.12		2005.0 - 2016.4		11.4
AFAL	12.17	46.53	2284.1	-0.76 ± 0.08		0.79 ± 0.06		1.29 ± 0.14		2005.0 - 2016.4		11.4
AGDE	3.47	43.30	65.8	-0.20 ± 0.13		-0.19 ± 0.10		0.05 ± 0.22		2007.7 - 2016.2		8.6
AGNE	7.14	45.47	2354.6	0.01 ± 0.25		-0.22 ± 0.18		1.42 ± 0.48		2007.2 - 2015.0		7.8
AIGL	3.58	44.12	1618.8	-0.11 ± 0.21		0.06 ± 0.17		0.64 ± 0.38		2004.0 - 2016.4		12.3
AJAC	8.76	41.93	98.8	-0.11 ± 0.22		-0.17 ± 0.16		-0.37 ± 0.38		2004.0 - 2016.4		12.0
ALLE	3.71	45.20	1084.9	-0.12 ± 0.94		0.26 ± 0.67		-0.02 ± 1.62		2012.5 - 2014.5		2.0
ALPE	6.08	45.09	1892.2	-0.33 ± 0.11		0.07 ± 0.09		0.82 ± 0.20		2006.8 - 2016.4		9.6
ANNO	4.67	45.24	465.6	0.32 ± 0.13		0.08 ± 0.10		0.00 ± 0.23		2007.5 - 2015.0		7.5
ARMI	2.77	43.24	101.5	-0.03 ± 0.14		-0.29 ± 0.10		0.09 ± 0.24		2007.6 - 2015.0		7.4
AUBU	7.20	48.22	1151.8	0.40 ± 0.21		-0.17 ± 0.16		-0.58 ± 0.43		2008.5 - 2016.4		7.9
AUMO	3.28	44.72	1115.6	0.01 ± 0.17		0.19 ± 0.12		-0.36 ± 0.28		2008.6 - 2015.0		6.4
AUTN	4.29	46.95	353.6	0.09 ± 0.19		-0.10 ± 0.14		-0.56 ± 0.31		2005.4 - 2016.4		10.9
AVEN	4.61	46.19	740.8	0.53 ± 0.13		0.31 ± 0.10		-0.54 ± 0.23		2007.5 - 2015.0		7.5
AXPV	5.33	43.49	229.4	-0.08 ± 0.15		0.21 ± 0.11		-0.42 ± 0.24		2004.0 - 2016.4		12.3
BANN	4.16	44.37	357.6	-0.04 ± 0.15		0.13 ± 0.11		0.05 ± 0.23		2004.0 - 2016.4		12.4
BART	7.48	47.63	321.0	-0.00 ± 0.37		0.26 ± 0.27		-0.01 ± 0.61		2011.2 - 2015.0		3.8
BAUB	3.97	43.88	211.0	0.01 ± 0.23		-0.04 ± 0.17		0.47 ± 0.39		2007.9 - 2013.3		5.4
BI2I	7.66	48.71	237.8	-0.74 ± 0.30		-0.33 ± 0.23		0.42 ± 0.51		2007.5 - 2010.5		3.0
BIWI	7.66	48.71	237.1	-0.74 ± 0.29		-0.33 ± 0.23		0.42 ± 0.51		2010.5 - 2014.4		3.9
BLIX	6.37	43.87	1077.1	-0.09 ± 0.17		0.01 ± 0.14		0.33 ± 0.31		2009.3 - 2016.4		7.1
BOSC	11.03	45.60	910.2	-0.32 ± 0.29		1.04 ± 0.23		-0.17 ± 0.52		2006.2 - 2014.0		7.6
BREI	10.55	47.55	1888.0	0.11 ± 0.08		0.43 ± 0.06		0.67 ± 0.13		2005.7 - 2016.1		10.4
BRST	-4.50	48.38	65.8	0.18 ± 0.20		0.62 ± 0.14		-0.33 ± 0.33		2009.5 - 2016.4		6.9
BSCN	5.99	47.25	359.5	0.19 ± 0.21		-0.12 ± 0.16		0.23 ± 0.36		2005.4 - 2016.4		10.9
BUAN	5.35	48.49	416.3	-0.31 ± 0.13		0.15 ± 0.11		0.11 ± 0.22		2007.9 - 2015.7		7.8
BUIS	5.27	44.28	445.8	-0.20 ± 0.15		-0.19 ± 0.11		-0.15 ± 0.26		2008.5 - 2015.0		6.5
BURE	5.91	44.63	2614.6	-0.39 ± 0.79		0.51 ± 0.65		0.97 ± 1.44		2004.7 - 2008.0		3.2
BZRG	11.34	46.50	329.1	-0.20 ± 0.19		0.50 ± 0.14		1.18 ± 0.32		2004.0 - 2016.4		12.3
CAME	13.12	43.11	498.7	1.14 ± 0.28		3.33 ± 0.22		0.99 ± 0.53		2004.0 - 2009.9		5.9
CANV	12.44	46.01	965.9	-0.13 ± 0.08		1.01 ± 0.06		0.10 ± 0.14		2005.0 - 2016.4		11.4
CAPA	3.51	43.29	71.1	-0.33 ± 0.42		0.28 ± 0.30		0.33 ± 0.70		2012.4 - 2015.0		2.6
CARZ	8.68	46.04	1165.3	-0.35 ± 0.15		0.11 ± 0.11		1.30 ± 0.26		2005.8 - 2015.0		9.2
CAZE	1.09	43.21	306.2	-0.49 ± 0.29		0.43 ± 0.20		-0.15 ± 0.50		2010.4 - 2015.0		4.6
CHAM	5.88	45.11	1874.6	-0.38 ± 0.11		-0.24 ± 0.08		1.07 ± 0.19		2004.0 - 2014.9		10.9

Annex A. Velocity field table

Site	Long. deg	Lat. deg	Height m	$V_{e,res}$ mm/a	σ_{V_e} mm/a	$V_{n,res}$ mm/a	σ_{V_n} mm/a	V_u mm/a	σ_{V_u} mm/a	Start	End	t_{obs} year
CHAR	5.15	45.73	266.8	0.03 ± 0.27		-0.33 ± 0.22		0.74 ± 0.46		2005.0 - 2009.3		4.4
CHIZ	-0.41	46.13	113.2	0.06 ± 0.08		0.17 ± 0.06		-0.08 ± 0.12		2004.0 - 2016.4		12.4
CHRN	4.86	43.88	103.0	-0.07 ± 0.11		0.15 ± 0.08		-0.42 ± 0.18		2004.0 - 2015.8		11.8
CHTL	6.36	45.30	850.3	-0.60 ± 0.10		0.17 ± 0.07		1.88 ± 0.18		2004.0 - 2016.4		12.4
CLFD	3.11	45.76	473.6	0.21 ± 0.13		-0.06 ± 0.10		0.61 ± 0.21		2006.8 - 2016.4		9.6
CODR	12.98	45.96	91.9	-0.38 ± 0.09		2.19 ± 0.07		0.13 ± 0.15		2007.4 - 2016.4		9.0
COMO	9.10	45.80	292.3	-0.35 ± 0.09		0.34 ± 0.07		-0.01 ± 0.15		2006.0 - 2016.4		10.4
CURA	2.86	44.20	1014.6	-0.01 ± 0.38		-0.21 ± 0.28		-0.43 ± 0.64		2011.9 - 2015.0		3.1
DEVE	8.26	46.31	1679.4	-0.13 ± 0.22		0.02 ± 0.14		2.56 ± 0.39		2005.8 - 2015.2		9.5
DILL	6.70	49.37	227.6	-0.07 ± 0.12		-0.22 ± 0.09		0.52 ± 0.20		2004.9 - 2016.4		11.4
DRES	13.73	51.03	203.1	-0.24 ± 0.13		-0.36 ± 0.10		0.43 ± 0.21		2004.0 - 2016.4		11.5
EGLT	2.05	45.40	667.0	0.16 ± 0.16		-0.23 ± 0.12		0.14 ± 0.27		2005.4 - 2016.4		10.9
ENTZ	7.64	48.55	204.3	-0.19 ± 0.13		0.11 ± 0.10		-0.90 ± 0.20		2004.9 - 2016.4		11.5
EOST	7.76	48.58	213.3	-0.04 ± 0.09		-0.19 ± 0.07		0.08 ± 0.14		2007.3 - 2016.4		9.1
ERCK	7.36	48.87	296.1	-0.24 ± 0.13		-0.10 ± 0.11		0.11 ± 0.23		2009.3 - 2016.4		7.1
ERLA	11.00	49.59	337.8	0.07 ± 0.15		-0.22 ± 0.12		0.38 ± 0.25		2004.0 - 2016.4		12.3
ESAB	4.80	45.31	207.7	0.22 ± 0.10		0.06 ± 0.07		-0.84 ± 0.15		2005.1 - 2015.0		9.9
ESNO	5.35	48.12	441.0	-0.01 ± 0.37		-0.12 ± 0.27		-0.56 ± 0.62		2011.9 - 2015.0		3.1
FAHR	11.31	47.61	1674.3	0.10 ± 0.08		0.34 ± 0.06		0.51 ± 0.14		2005.6 - 2016.1		10.5
FCLZ	5.99	45.64	1358.2	0.11 ± 0.17		0.00 ± 0.12		0.91 ± 0.33		2004.0 - 2011.9		7.9
FDOS	11.72	46.30	1889.3	-0.19 ± 0.13		0.51 ± 0.10		2.16 ± 0.23		2006.2 - 2016.2		10.1
FENO	2.03	43.16	396.2	0.18 ± 0.40		0.09 ± 0.28		0.37 ± 0.69		2011.9 - 2015.0		3.1
FERH	7.03	45.87	2400.3	0.34 ± 1.27		0.81 ± 0.96		1.48 ± 2.67		2009.4 - 2012.6		3.2
FFMJ	8.66	50.09	178.2	-0.42 ± 0.14		-0.19 ± 0.11		-1.39 ± 0.22		2004.0 - 2016.4		11.3
FJCP	2.79	43.05	322.7	-0.59 ± 0.11		0.20 ± 0.08		0.44 ± 0.19		2004.2 - 2015.2		11.0
FRAC	6.75	47.66	425.4	-0.48 ± 0.21		0.16 ± 0.16		-0.16 ± 0.36		2007.5 - 2015.0		7.4
FUSE	13.00	46.41	581.9	-0.18 ± 0.11		0.95 ± 0.07		1.17 ± 0.18		2007.7 - 2016.4		8.7
GARI	12.25	44.68	47.7	0.07 ± 0.22		1.62 ± 0.16		-2.05 ± 0.36		2009.9 - 2016.4		6.6
GENO	8.92	44.42	155.5	0.18 ± 0.08		0.11 ± 0.06		-0.16 ± 0.14		2004.0 - 2016.4		12.4
GINA	5.79	43.68	382.0	-0.22 ± 0.28		0.13 ± 0.23		-0.40 ± 0.52		2004.0 - 2009.0		5.0
GOET	9.95	51.50	214.9	-0.08 ± 0.15		0.22 ± 0.12		0.86 ± 0.24		2007.0 - 2015.5		8.6
GRAS	6.92	43.75	1319.3	-0.01 ± 0.06		0.14 ± 0.04		0.14 ± 0.08		2004.8 - 2016.4		11.6
GRAZ	15.49	47.07	538.3	0.50 ± 0.10		0.49 ± 0.05		0.43 ± 0.09		2005.9 - 2016.4		9.6
GROI	-3.51	47.65	93.2	-0.56 ± 0.11		-0.32 ± 0.09		0.06 ± 0.19		2004.5 - 2014.5		10.1
GSR1	14.54	46.05	351.7	-0.26 ± 0.12		2.02 ± 0.09		0.34 ± 0.20		2004.0 - 2016.4		12.4
GUIL	6.66	44.66	1171.1	0.02 ± 0.17		-0.03 ± 0.13		1.31 ± 0.31		2007.9 - 2016.4		8.5
HEAU	-1.78	49.58	188.6	0.06 ± 0.11		-0.06 ± 0.09		0.04 ± 0.19		2004.0 - 2014.8		10.8
HELM	12.38	46.72	2451.3	-1.00 ± 0.44		-0.57 ± 0.33		0.77 ± 0.72		2012.8 - 2016.1		3.4
HFL2	11.39	47.31	2384.0	-0.09 ± 0.19		0.71 ± 0.15		0.61 ± 0.32		2008.2 - 2011.7		3.5
HFLK	11.39	47.31	2384.2	-0.09 ± 0.19		0.72 ± 0.15		0.61 ± 0.32		2004.0 - 2008.2		4.1
HGRA	10.07	47.49	1764.1	-0.09 ± 0.09		0.32 ± 0.07		0.75 ± 0.15		2005.6 - 2016.1		10.5
HKBL	13.77	47.38	1919.5	0.19 ± 0.15		1.28 ± 0.12		-0.20 ± 0.25		2004.0 - 2016.4		11.1
HOFJ	11.88	50.31	614.9	0.15 ± 0.19		-0.39 ± 0.15		0.43 ± 0.31		2007.2 - 2016.4		9.1
HRIE	12.25	47.75	1615.2	-0.09 ± 0.10		0.67 ± 0.08		0.02 ± 0.17		2005.6 - 2015.4		9.8

Annex A. Velocity field table

Site	Long. deg	Lat. deg	Height m	$V_{e,res}$ mm/a	σ_{V_e} mm/a	$V_{n,res}$ mm/a	σ_{V_n} mm/a	V_u mm/a	σ_{V_u} mm/a	Start	End	t_{obs} year
HUEG	7.60	47.83	278.3	0.19 ± 0.15		0.27 ± 0.11		-0.17 ± 0.24		2004.0	- 2016.4	12.2
IENG	7.64	45.02	316.6	0.30 ± 0.08		-0.33 ± 0.05		0.36 ± 0.12		2004.0	- 2016.4	12.4
IGMI	11.21	43.80	95.1	0.21 ± 0.19		2.25 ± 0.14		0.12 ± 0.34		2006.9	- 2016.4	9.4
JANU	6.71	44.91	2583.9	0.27 ± 0.11		-0.33 ± 0.08		1.85 ± 0.18		2005.8	- 2016.1	10.3
JOAN	13.42	46.18	1190.5	-0.47 ± 0.07		1.71 ± 0.05		0.42 ± 0.12		2007.5	- 2016.4	8.9
JOUX	5.80	46.53	845.5	-0.08 ± 0.10		0.16 ± 0.08		0.46 ± 0.17		2004.0	- 2014.9	10.8
JUVI	6.28	46.22	556.5	-0.24 ± 0.78		0.04 ± 0.57		0.87 ± 1.32		2012.1	- 2014.0	1.8
KARL	8.41	49.01	182.9	0.09 ± 0.09		0.14 ± 0.07		0.04 ± 0.14		2004.0	- 2016.4	12.4
KOE2	13.01	46.67	756.0	0.41 ± 0.23		0.93 ± 0.19		1.34 ± 0.42		2008.2	- 2016.4	8.2
KOET	13.01	46.67	756.1	0.40 ± 0.23		0.93 ± 0.19		1.33 ± 0.42		2005.5	- 2008.2	2.7
KRBG	10.63	47.15	2258.0	-0.28 ± 0.13		0.38 ± 0.10		0.13 ± 0.20		2004.0	- 2016.4	12.3
KTZ2	12.36	47.42	1847.8	-0.09 ± 0.20		0.51 ± 0.15		0.22 ± 0.32		2008.0	- 2016.4	8.4
LACA	2.73	43.68	1315.6	-0.07 ± 0.14		0.04 ± 0.10		0.26 ± 0.25		2005.4	- 2014.6	9.1
LAJA	6.35	44.18	851.7	-0.05 ± 0.48		0.19 ± 0.35		0.28 ± 0.87		2011.9	- 2014.8	3.0
LEBE	5.62	45.92	940.6	0.01 ± 0.10		0.07 ± 0.07		0.74 ± 0.16		2005.4	- 2016.4	11.0
LFAZ	5.40	45.12	1071.2	-0.05 ± 0.10		-0.00 ± 0.08		0.81 ± 0.17		2005.0	- 2016.4	11.4
LINZ	14.28	48.31	335.0	-0.04 ± 0.11		-0.08 ± 0.09		0.37 ± 0.19		2005.5	- 2016.4	10.9
LROC	-1.22	46.16	57.9	0.02 ± 0.07		0.20 ± 0.03		-0.20 ± 0.06		2004.0	- 2016.4	12.4
LUCE	7.27	47.44	741.6	0.04 ± 0.12		0.26 ± 0.10		0.47 ± 0.21		2007.8	- 2016.4	8.6
LUVI	4.10	43.69	71.0	0.17 ± 0.12		-0.01 ± 0.08		-0.32 ± 0.20		2007.5	- 2014.8	7.3
MAKS	7.03	47.92	1237.2	0.09 ± 0.10		-0.03 ± 0.07		0.30 ± 0.15		2007.4	- 2016.4	9.1
MANS	0.16	48.02	168.0	-0.22 ± 0.38		0.47 ± 0.32		1.70 ± 0.68		2004.0	- 2008.1	4.0
MARS	5.35	43.28	61.8	-0.02 ± 0.18		-0.07 ± 0.13		-0.50 ± 0.32		2004.6	- 2016.4	11.8
MAVE	11.83	46.03	1466.0	-0.31 ± 0.12		1.55 ± 0.09		1.04 ± 0.20		2006.4	- 2015.0	8.6
MDEA	13.44	45.92	165.7	-0.43 ± 0.08		2.57 ± 0.06		-0.15 ± 0.13		2005.1	- 2016.4	11.3
MDOR	4.81	45.80	330.6	0.14 ± 0.24		-0.12 ± 0.17		-0.17 ± 0.41		2009.9	- 2013.9	4.1
MEDI	11.65	44.52	50.0	1.31 ± 0.07		2.43 ± 0.05		-1.15 ± 0.10		2004.0	- 2016.4	12.4
MICH	5.72	43.92	628.1	-0.18 ± 0.09		0.03 ± 0.06		0.08 ± 0.14		2004.0	- 2016.4	12.4
MITT	11.29	46.69	2356.3	-0.12 ± 0.31		0.69 ± 0.24		1.62 ± 0.52		2007.2	- 2016.2	6.5
MLVL	2.59	48.84	160.5	0.46 ± 0.14		-0.40 ± 0.11		-0.03 ± 0.22		2005.4	- 2016.4	10.7
MOCA	11.14	46.10	1147.1	-0.07 ± 0.26		1.01 ± 0.21		1.61 ± 0.46		2006.7	- 2010.6	3.9
MODA	6.71	45.21	1182.3	-0.08 ± 0.09		-0.38 ± 0.07		1.71 ± 0.16		2004.0	- 2016.4	12.4
MOGN	4.80	46.15	233.0	0.17 ± 0.14		0.02 ± 0.10		-2.03 ± 0.23		2004.8	- 2015.0	10.2
MOLA	2.34	43.72	596.2	0.06 ± 0.17		0.05 ± 0.12		-0.18 ± 0.28		2007.5	- 2015.0	7.5
MOLV	5.84	48.61	330.4	0.05 ± 0.47		0.01 ± 0.35		-0.03 ± 0.82		2011.5	- 2015.0	3.5
MONT	4.07	45.72	435.6	-0.45 ± 0.12		-0.55 ± 0.08		0.03 ± 0.19		2007.5	- 2015.0	7.5
MOPS	10.95	44.63	92.2	0.91 ± 0.19		3.30 ± 0.13		-0.62 ± 0.31		2007.8	- 2016.3	7.9
MOUS	6.78	48.68	298.0	0.20 ± 0.14		-0.24 ± 0.11		-0.11 ± 0.24		2007.5	- 2014.0	6.5
MPRA	12.99	46.24	808.6	-0.60 ± 0.08		1.42 ± 0.05		0.06 ± 0.13		2005.0	- 2016.4	11.4
MTPL	3.86	43.64	120.3	-0.02 ± 0.11		0.01 ± 0.08		-0.11 ± 0.18		2004.0	- 2013.9	9.9
NICA	7.23	43.70	256.5	-0.05 ± 0.12		0.08 ± 0.09		-0.17 ± 0.20		2004.0	- 2015.0	10.9
NICE	7.30	43.73	427.3	0.06 ± 0.09		-0.03 ± 0.06		0.14 ± 0.14		2004.0	- 2016.4	12.4
NOVE	12.59	45.67	47.9	0.43 ± 0.19		1.44 ± 0.14		-2.08 ± 0.30		2009.4	- 2016.4	7.0
OATO	7.77	45.04	658.8	-0.09 ± 0.17		-0.65 ± 0.13		0.50 ± 0.31		2005.8	- 2015.0	9.2

Annex A. Velocity field table

Site	Long. deg	Lat. deg	Height m	$V_{e,res}$ mm/a	σ_{V_e} mm/a	$V_{n,res}$ mm/a	σ_{V_n} mm/a	V_u mm/a	σ_{V_u} mm/a	Start	End	t_{obs} year
OBE2	11.28	48.09	641.4	-0.33 ± 0.88		0.39 ± 0.74		0.96 ± 1.55		2004.0 - 2007.7		3.7
OBE4	11.28	48.08	650.5	-0.15 ± 0.17		0.27 ± 0.13		-0.29 ± 0.28		2012.7 - 2016.4		3.7
OGAG	6.54	44.79	1356.5	0.84 ± 1.32		0.39 ± 0.75		3.03 ± 2.80		2011.5 - 2016.4		4.8
PADO	11.90	45.41	64.7	0.09 ± 0.10		1.39 ± 0.08		-0.67 ± 0.17		2004.0 - 2016.4		12.4
PALI	4.81	43.38	60.4	-0.28 ± 0.12		0.28 ± 0.09		-0.97 ± 0.19		2007.9 - 2016.4		8.4
PARD	2.82	43.43	622.8	0.18 ± 0.19		0.07 ± 0.14		-0.06 ± 0.32		2007.9 - 2015.9		8.0
PARO	8.08	44.45	849.8	0.47 ± 0.24		-0.08 ± 0.19		0.38 ± 0.44		2009.0 - 2015.0		6.0
PAZO	13.05	45.81	50.1	-0.12 ± 0.15		1.98 ± 0.11		-0.34 ± 0.23		2007.9 - 2016.2		8.2
PFA2	9.78	47.52	1090.1	0.04 ± 0.14		0.39 ± 0.11		0.88 ± 0.24		2008.8 - 2016.4		7.6
PFAN	9.78	47.52	1090.3	0.04 ± 0.15		0.39 ± 0.11		0.88 ± 0.24		2004.2 - 2007.9		3.7
PIGN	6.23	43.30	234.5	-0.16 ± 0.13		0.18 ± 0.09		-0.22 ± 0.21		2007.5 - 2015.0		7.5
PLOE	-3.43	47.75	73.9	-0.04 ± 0.12		0.43 ± 0.09		-0.04 ± 0.21		2006.9 - 2016.4		9.5
POGG	8.16	44.11	855.6	0.17 ± 0.68		0.26 ± 0.54		-0.10 ± 1.20		2006.1 - 2013.0		6.9
POLI	5.47	45.25	280.1	-0.05 ± 0.14		0.08 ± 0.10		0.20 ± 0.24		2007.5 - 2015.0		7.5
PORA	10.11	45.89	1927.3	-0.37 ± 0.27		0.56 ± 0.20		0.42 ± 0.45		2008.7 - 2012.4		3.7
PORE	13.60	45.23	66.2	-0.08 ± 0.19		2.85 ± 0.14		0.57 ± 0.32		2011.7 - 2016.4		4.7
POTS	13.07	52.38	144.4	-0.25 ± 0.19		-0.16 ± 0.17		0.23 ± 0.35		2004.0 - 2009.2		5.2
PQRL	6.21	42.98	112.3	-0.02 ± 0.24		-0.02 ± 0.19		-0.80 ± 0.46		2004.0 - 2014.8		9.5
PRAT	11.10	43.89	120.0	0.33 ± 0.20		1.99 ± 0.15		0.67 ± 0.38		2005.2 - 2016.4		11.2
PUEC	3.31	43.69	256.0	0.17 ± 0.13		0.06 ± 0.10		-0.08 ± 0.24		2007.5 - 2015.0		7.5
PUYA	6.48	44.86	1690.3	0.03 ± 0.10		0.29 ± 0.07		1.64 ± 0.16		2005.9 - 2016.4		10.5
PUYV	3.88	45.04	710.4	0.19 ± 0.13		0.38 ± 0.09		-0.06 ± 0.22		2004.7 - 2016.4		11.7
RABU	6.98	44.27	2551.8	0.03 ± 0.11		-0.17 ± 0.08		0.50 ± 0.20		2004.0 - 2015.8		11.8
RIED	13.49	48.20	505.3	0.40 ± 0.60		0.59 ± 0.51		0.57 ± 1.06		2004.0 - 2006.4		2.3
RIXH	7.38	47.73	366.8	0.06 ± 0.26		0.06 ± 0.21		0.43 ± 0.47		2011.2 - 2016.4		5.2
ROHR	14.00	48.57	658.1	-0.19 ± 0.71		0.14 ± 0.61		0.95 ± 1.27		2004.0 - 2006.4		2.3
ROSD	6.63	45.69	1694.5	-0.44 ± 0.11		-0.09 ± 0.08		2.21 ± 0.19		2006.0 - 2016.4		10.5
ROVE	11.04	45.89	261.7	-0.13 ± 0.26		0.57 ± 0.18		1.71 ± 0.44		2006.2 - 2016.4		9.8
RSTL	5.48	43.94	1069.8	-0.28 ± 0.08		0.09 ± 0.05		0.22 ± 0.12		2004.0 - 2016.4		12.4
SAPI	4.91	45.71	246.1	0.12 ± 0.18		-0.09 ± 0.13		-0.09 ± 0.31		2010.0 - 2015.0		5.0
SAUV	4.47	44.26	367.4	-0.07 ± 0.09		0.04 ± 0.06		0.05 ± 0.14		2004.5 - 2016.4		12.0
SBG2	13.11	47.80	1323.4	-0.32 ± 0.13		0.92 ± 0.10		0.38 ± 0.21		2008.8 - 2016.4		7.6
SBGZ	13.11	47.80	1323.6	-0.32 ± 0.13		0.92 ± 0.10		0.38 ± 0.21		2004.2 - 2006.5		2.3
SETE	3.70	43.40	55.0	0.24 ± 0.18		0.11 ± 0.13		-0.31 ± 0.31		2007.8 - 2016.4		8.6
SIMA	5.42	46.22	367.0	-0.04 ± 0.16		-0.27 ± 0.12		-0.12 ± 0.28		2008.9 - 2015.0		6.1
SJDV	4.68	45.88	432.4	-0.01 ± 0.08		0.10 ± 0.06		-0.07 ± 0.12		2004.0 - 2016.4		12.4
SLVT	3.27	43.92	811.8	0.01 ± 0.15		0.14 ± 0.12		0.14 ± 0.26		2007.7 - 2014.8		7.1
SOND	9.85	46.17	529.2	0.17 ± 0.21		-0.24 ± 0.17		1.22 ± 0.43		2006.6 - 2012.9		6.4
SOPH	7.05	43.61	178.8	0.00 ± 0.08		0.16 ± 0.06		0.07 ± 0.14		2004.0 - 2016.4		12.4
SOUR	2.43	42.73	595.6	0.30 ± 0.23		-0.51 ± 0.17		0.05 ± 0.41		2009.4 - 2015.0		5.6
SPRN	16.58	47.68	278.9	0.63 ± 0.15		-0.12 ± 0.11		0.47 ± 0.24		2007.6 - 2016.4		8.8
STEY	5.76	45.24	1394.9	-0.42 ± 0.07		0.06 ± 0.05		1.22 ± 0.10		2004.0 - 2016.4		12.4
STGR	4.57	44.19	136.9	0.14 ± 0.11		-0.10 ± 0.08		-0.39 ± 0.18		2007.5 - 2015.0		7.5
STJ9	7.68	48.62	237.2	0.00 ± 0.07		0.12 ± 0.05		-0.41 ± 0.11		2004.0 - 2016.4		12.4

Annex A. Velocity field table

Site	Long. deg	Lat. deg	Height m	$V_{e,res}$ mm/a	σ_{V_e} mm/a	$V_{n,res}$ mm/a	σ_{V_n} mm/a	V_u mm/a	σ_{V_u} mm/a	Start	End	t_{obs} year
STMR	4.42	43.45	56.1	-0.31 ± 0.16		-0.05 ± 0.13		-1.85 ± 0.27		2008.3 - 2016.4		8.1
SUSE	12.21	45.86	221.7	0.10 ± 0.23		1.33 ± 0.16		-0.65 ± 0.40		2011.4 - 2016.4		5.0
TENC	4.29	45.12	936.5	0.16 ± 0.19		-0.00 ± 0.15		0.31 ± 0.33		2004.5 - 2014.5		10.0
TLSE	1.48	43.56	207.2	0.22 ± 0.23		-0.10 ± 0.18		0.31 ± 0.42		2004.0 - 2009.5		5.5
TORI	7.66	45.06	310.7	0.12 ± 0.26		-0.13 ± 0.19		0.65 ± 0.47		2004.8 - 2016.4		7.4
TRES	5.90	45.68	375.6	-0.18 ± 0.13		-0.22 ± 0.09		0.96 ± 0.22		2007.6 - 2015.0		7.4
TRF2	15.86	47.93	1092.5	0.08 ± 0.26		0.15 ± 0.17		-0.90 ± 0.46		2008.2 - 2016.4		10.0
TRIE	13.76	45.71	323.4	-0.49 ± 0.07		2.47 ± 0.05		-0.01 ± 0.11		2005.0 - 2016.4		11.4
TROC	5.08	46.73	257.5	0.27 ± 0.16		-0.21 ± 0.11		-0.43 ± 0.27		2008.7 - 2015.0		6.3
TROP	6.60	43.22	369.3	-0.21 ± 0.10		0.19 ± 0.07		-0.32 ± 0.16		2005.7 - 2015.8		10.1
UDI1	13.25	46.04	149.3	-0.61 ± 0.08		1.98 ± 0.06		0.07 ± 0.13		2006.4 - 2016.4		10.0
UNPG	12.36	43.12	351.1	0.28 ± 0.61		0.96 ± 0.42		0.59 ± 1.05		2014.0 - 2016.4		2.4
VALD	6.72	43.80	1148.2	-0.01 ± 0.25		-0.29 ± 0.19		0.53 ± 0.46		2009.4 - 2015.0		5.6
VARM	12.57	46.46	2121.4	-0.06 ± 0.28		0.48 ± 0.21		1.78 ± 0.45		2012.6 - 2016.4		3.8
VAUC	5.83	47.66	283.9	-0.17 ± 0.22		0.19 ± 0.16		-1.35 ± 0.37		2008.6 - 2015.0		6.4
VEN1	12.35	45.43	60.4	-0.01 ± 0.10		1.11 ± 0.07		-1.36 ± 0.16		2010.0 - 2016.4		6.5
VERN	10.83	46.87	3127.3	-0.06 ± 0.16		0.61 ± 0.11		2.29 ± 0.27		2010.6 - 2016.3		5.8
VFCH	1.72	47.29	153.3	0.16 ± 0.16		-0.06 ± 0.12		0.12 ± 0.26		2005.4 - 2016.4		10.9
VIGY	6.29	49.20	310.3	-0.32 ± 0.40		0.57 ± 0.30		-0.07 ± 0.68		2010.4 - 2014.7		4.3
VLCH	13.85	46.61	572.1	0.16 ± 0.10		0.91 ± 0.08		0.84 ± 0.17		2004.0 - 2016.4		12.4
VLKM	14.63	46.66	527.3	0.71 ± 0.46		1.11 ± 0.36		0.05 ± 0.80		2004.0 - 2016.4		10.7
WART	12.81	47.65	1749.4	0.03 ± 0.09		0.52 ± 0.07		0.50 ± 0.15		2005.6 - 2016.1		10.5
WELS	14.02	48.16	385.2	0.13 ± 0.10		0.17 ± 0.08		0.17 ± 0.17		2005.3 - 2016.4		11.1
WIEN	16.37	48.22	243.8	-1.00 ± 0.25		0.84 ± 0.21		-0.67 ± 0.44		2004.0 - 2016.4		7.2
WLBH	7.35	48.42	819.1	-0.02 ± 0.10		-0.26 ± 0.08		-2.88 ± 0.19		2004.0 - 2016.4		12.4
WT21	12.88	49.15	657.4	0.05 ± 0.16		0.11 ± 0.12		-0.00 ± 0.25		2010.8 - 2016.4		5.6
WTZR	12.88	49.14	666.0	-0.03 ± 0.07		0.15 ± 0.06		-0.15 ± 0.07		2004.0 - 2016.4		11.4
ZADA	15.23	44.11	64.3	0.15 ± 0.20		2.91 ± 0.14		-0.37 ± 0.34		2011.7 - 2016.4		4.7
ZIM2	7.47	46.88	956.4	-0.09 ± 0.07		0.34 ± 0.05		0.94 ± 0.09		2009.4 - 2016.4		7.0
ZIMM	7.47	46.88	956.3	-0.13 ± 0.06		0.38 ± 0.04		0.95 ± 0.09		2004.0 - 2016.4		12.4
ZOUF	12.97	46.56	1946.5	0.10 ± 0.07		0.89 ± 0.05		1.29 ± 0.11		2005.0 - 2016.4		11.4

Annex B. Discontinuities

No.	Site	Sol	Start	End	T _{obs}	Discontinuity due to
			yyyy.y	yyyy.y	yy.y	Ant Rad Ecc Rec Other
1	ACOM	1	2005.0	- 2016.4	11.4	
2	AFAL	1	2005.0	- 2016.4	11.4	
3	AGDE	1	2007.7	- 2016.2	8.6	
4	AGNE	1	2007.2	- 2015.0	7.8	
5	AIGL	1	2004.0	- 2008.0	4.0	
6	AIGL	2	2008.0	- 2015.0	7.0	Other
7	AIGL	3	2015.0	- 2016.4	1.4	Other
8	AJAC	1	2004.0	- 2008.6	4.6	
9	AJAC	2	2009.0	- 2012.9	4.0	Ant
10	AJAC	3	2013.0	- 2016.4	3.4	Ant
11	ALLE	1	2012.5	- 2014.5	2.0	
12	ALPE	1	2006.8	- 2016.4	9.6	
13	ANNO	1	2007.5	- 2015.0	7.5	
14	ARMI	1	2007.6	- 2015.0	7.4	
15	AUTN	1	2005.4	- 2009.6	4.2	
16	AUTN	2	2009.7	- 2013.4	3.7	Ant Rad
17	AUTN	3	2013.4	- 2016.4	3.0	Ant Rad
18	AUBU	1	2008.5	- 2016.4	7.9	
19	AUMO	1	2008.6	- 2015.0	6.4	
20	AVEN	1	2007.5	- 2015.0	7.5	
21	AXPV	1	2004.0	- 2009.0	5.0	
22	AXPV	2	2009.0	- 2011.8	2.8	Ant
23	AXPV	3	2011.9	- 2016.4	4.5	Ant Rad
24	BANN	1	2004.0	- 2005.0	1.0	
25	BANN	2	2005.0	- 2012.4	7.4	Other
26	BANN	3	2012.4	- 2015.0	2.6	Rec
27	BANN	4	2015.0	- 2016.4	1.4	Rec
28	BART	1	2011.2	- 2015.0	3.8	
29	BAUB	1	2007.9	- 2013.3	5.4	
30	BI2I	1	2007.5	- 2010.5	3.0	
31	BIWI	1	2010.5	- 2014.4	3.9	
32	BLIX	1	2009.3	- 2016.4	7.1	
33	BOSC	1	2006.2	- 2008.9	2.7	
34	BOSC	2	2009.1	- 2014.0	4.9	Rad
35	BREI	1	2005.7	- 2016.1	10.4	
36	BRST	1	2009.5	- 2011.8	2.3	
37	BRST	2	2011.8	- 2016.4	4.6	Other
38	BSCN	1	2005.4	- 2009.0	3.6	

No.	Site	Sol	Start	End	T _{obs}	Discontinuity due to
			yyyy.y	yyyy.y	yy.y	Ant Rad Ecc Rec Other
39	BSCN	2	2009.0	- 2012.9	3.8	Ant
40	BSCN	3	2012.9	- 2016.4	3.5	Ant Rad
41	BUAN	1	2007.9	- 2015.7	7.8	
42	BUIS	1	2008.5	- 2015.0	6.5	
43	BURE	1	2004.7	- 2008.0	3.2	
44	BZRG	1	2004.0	- 2006.4	2.4	
45	BZRG	2	2006.4	- 2007.9	1.6	Other
46	BZRG	3	2008.0	- 2012.1	4.2	Ant
47	BZRG	4	2012.1	- 2016.4	4.3	Ant Rad
48	CAME	1	2004.0	- 2009.9	5.9	
49	CANV	1	2005.0	- 2016.4	11.4	
50	CAPA	1	2012.4	- 2015.0	2.6	
51	CARZ	1	2005.8	- 2015.0	9.2	
52	CAZE	1	2010.4	- 2015.0	4.6	
53	CHIZ	1	2004.0	- 2016.4	12.4	
54	CHAM	1	2004.0	- 2014.9	10.9	
55	CHAR	1	2005.0	- 2009.3	4.4	
56	CHRN	1	2004.0	- 2015.8	11.8	
57	CHTL	1	2004.0	- 2016.4	12.4	
58	CLFD	1	2006.8	- 2016.4	9.6	
59	COMO	1	2006.0	- 2016.4	10.4	
60	CODR	1	2007.4	- 2016.4	9.0	
61	CURA	1	2011.9	- 2015.0	3.1	
62	DEVE	1	2005.8	- 2015.2	9.5	
63	DILL	1	2004.9	- 2012.2	7.3	
64	DILL	2	2012.3	- 2016.4	4.1	Ant Rad
65	DRES	1	2004.0	- 2006.4	2.4	
66	DRES	2	2007.4	- 2010.7	3.4	Ant Rad Ecc Rec
67	DRES	3	2010.7	- 2016.4	5.7	Ant Rad Ecc Rec
68	EGLT	1	2005.4	- 2008.9	3.4	
69	EGLT	2	2008.9	- 2012.8	3.9	Ant
70	EGLT	3	2012.8	- 2016.4	3.6	Ant Rad
71	ENTZ	1	2004.9	- 2009.6	4.6	
72	ENTZ	2	2009.6	- 2014.1	4.5	Ant Rad
73	ENTZ	3	2014.1	- 2016.4	2.3	Ant Rad
74	EOST	1	2007.3	- 2016.4	9.1	
75	ERCK	1	2009.3	- 2016.4	7.1	
76	ERLA	1	2004.0	- 2006.5	2.5	

Annex B. Discontinuities

No.	Site	Sol	Start	End	T _{obs}	Discontinuity due to						
						yyyy.y	yyyy.y	yy.y	Ant	Rad	Ecc	Rec
77	ERLA	2	2006.6 - 2010.6	4.1								Ecc
78	ERLA	3	2010.6 - 2012.2	1.5					Ant	Rad	Ecc	
79	ERLA	4	2012.2 - 2016.4	4.2					Ant	Rad	Ecc	Rec
80	ESAB	1	2005.1 - 2015.0	9.9								
81	ESNO	1	2011.9 - 2015.0	3.1								
82	FAHR	1	2005.6 - 2016.1	10.5								
83	FCLZ	1	2004.0 - 2011.9	7.9								
84	FDOS	1	2006.2 - 2016.2	10.1								
85	FENO	1	2011.9 - 2015.0	3.1								
86	FERH	1	2009.4 - 2012.6	3.2								
87	FFMJ	1	2004.0 - 2005.4	1.4								
88	FFMJ	2	2005.4 - 2008.1	2.7					Ant	Rad		
89	FFMJ	3	2008.2 - 2011.1	2.9					Ant	Rad	Ecc	
90	FFMJ	4	2012.1 - 2016.4	4.3					Ant	Rad	Ecc	Rec
91	FJCP	1	2004.2 - 2015.2	11.0								
92	FRAC	1	2007.5 - 2012.8	5.3								
93	FRAC	2	2012.8 - 2015.0	2.2								Other
94	FUSE	1	2007.7 - 2016.4	8.7								
95	GARI	1	2009.9 - 2011.8	2.0								
96	GARI	2	2011.8 - 2016.4	4.6								Other
97	GENO	1	2004.0 - 2016.4	12.4								
98	GINA	1	2004.0 - 2009.0	5.0								
99	GOET	1	2007.0 - 2011.2	4.2								
100	GOET	2	2011.2 - 2015.5	4.4					Ant	Rad		Rec
101	GRAS	1	2004.8 - 2016.4	11.6								
102	GRAZ	1	2005.9 - 2009.5	3.6								
103	GRAZ	2	2010.4 - 2016.4	6.0					Ant	Rad		Rec
104	GROI	1	2004.5 - 2014.5	10.1								
105	GSR1	1	2004.0 - 2008.7	4.7								
106	GSR1	2	2008.7 - 2016.4	7.7					Ant			Rec
107	GUIL	1	2007.9 - 2016.4	8.5								
108	HEAU	1	2004.0 - 2014.8	10.8								
109	HELM	1	2012.8 - 2016.1	3.4								
110	HFL2	1	2008.2 - 2011.7	3.5								
111	HFLK	1	2004.0 - 2008.2	4.1								
112	HGRA	1	2005.6 - 2016.1	10.5								
113	HKBL	1	2004.0 - 2006.0	2.0								
114	HKBL	2	2006.0 - 2010.4	4.4					Ant			Rec
115	HKBL	3	2011.7 - 2016.4	4.7					Ecc	Rec		
116	HOFJ	1	2007.2 - 2011.1	3.9								
117	HOFJ	2	2011.1 - 2014.4	3.3					Ant	Rad		Rec
118	HOFJ	3	2014.5 - 2016.4	1.9					Ant	Rad		Rec

No.	Site	Sol	Start	End	T _{obs}	Discontinuity due to						
						yyyy.y	yyyy.y	yy.y	Ant	Rad	Ecc	Rec
119	HRIE	1	2005.6 - 2015.4	9.8								
120	HUEG	1	2004.0 - 2005.9	1.9								
121	HUEG	2	2006.0 - 2008.2	2.2								Other
122	HUEG	3	2008.2 - 2013.5	5.3					Ant	Rad		
123	HUEG	4	2013.5 - 2016.4	2.9					Ant	Rad		Rec
124	IENG	1	2004.0 - 2016.4	12.4								
125	IGMI	1	2006.9 - 2008.9	2.0								
126	IGMI	2	2008.9 - 2014.3	5.3					Ant	Rad		
127	IGMI	3	2014.3 - 2016.4	2.1					Ant	Rad		
128	JANU	1	2005.8 - 2016.1	10.3								
129	JOAN	1	2007.5 - 2016.4	8.9								
130	JOUX	1	2004.0 - 2014.9	10.8								
131	JUVI	1	2012.1 - 2014.0	1.8								
132	KARL	1	2004.0 - 2012.2	8.2								
133	KARL	2	2012.2 - 2016.4	4.2								Rec
134	KOE2	1	2008.2 - 2012.9	4.7								
135	KOE2	2	2012.9 - 2016.4	3.5					Ant	Rad	Ecc	
136	KOET	1	2005.5 - 2008.2	2.7								
137	KRBG	1	2004.0 - 2005.6	1.6								
138	KRBG	2	2005.7 - 2010.5	4.8					Ant		Ecc	Rec
139	KRBG	3	2010.5 - 2016.4	5.9					Ant	Rad	Ecc	Rec
140	KTZ2	1	2008.0 - 2010.4	2.4								
141	KTZ2	2	2010.4 - 2012.7	2.3					Ant			Rec
142	KTZ2	3	2012.7 - 2016.4	3.7					Ant	Rad	Ecc	Rec
143	LACA	1	2005.4 - 2014.6	9.1								
144	LAJA	1	2011.9 - 2014.8	3.0								
145	LEBE	1	2005.4 - 2016.4	11.0								
146	LFAZ	1	2005.0 - 2016.4	11.4								
147	LINZ	1	2005.5 - 2013.7	8.2								
148	LINZ	2	2013.8 - 2016.4	2.6					Ant	Rad		Rec
149	LROC	1	2004.0 - 2016.4	12.4								
150	LUCE	1	2007.8 - 2016.4	8.6								
151	LUVI	1	2007.5 - 2014.8	7.3								
152	MARS	1	2004.6 - 2009.2	4.6								
153	MARS	2	2009.2 - 2012.7	3.5					Ant	Rad		
154	MARS	3	2012.8 - 2016.4	3.6					Ant	Rad		Rec
155	MAKS	1	2007.4 - 2016.4	9.1								
156	MANS	1	2004.0 - 2008.1	4.0								
157	MAVE	1	2006.4 - 2015.0	8.6								
158	MDEA	1	2005.1 - 2016.4	11.3								
159	MDOR	1	2009.9 - 2013.9	4.1								
160	MEDI	1	2004.0 - 2016.4	12.4								

Annex B. Discontinuities

No.	Site	Sol	Start	End	T _{obs}	Discontinuity due to						No.	Site	Sol	Start	End	T _{obs}	Discontinuity due to						
						yyyy.y	yyyy.y	yy.y	Ant	Rad	Ecc							yyyy.y	yyyy.y	yy.y	Ant	Rad	Ecc	Rec
161	MICH	1	2004.0 - 2016.4	12.4								203	POGG	1	2006.1 - 2013.0	6.9								
162	MITT	1	2007.2 - 2010.3	3.1								204	POLI	1	2007.5 - 2015.0	7.5								
163	MITT	2	2012.8 - 2016.2	3.4	Rad							205	PORA	1	2008.7 - 2012.4	3.7								
164	MLVL	1	2005.4 - 2008.7	3.3								206	PORE	1	2011.7 - 2016.4	4.7								
165	MLVL	2	2009.0 - 2013.3	4.3	Ant				Rec			207	POTS	1	2004.0 - 2009.2	5.2								
166	MLVL	3	2013.3 - 2016.4	3.1	Ant				Rec			208	PQRL	1	2004.0 - 2008.9	4.9								
167	MOPS	1	2007.8 - 2011.9	4.1								209	PQRL	2	2010.1 - 2014.8	4.7	Ant			Rec				
168	MOPS	2	2012.4 - 2016.3	3.8	Ant			Ecc				210	PRAT	1	2005.2 - 2007.1	1.9								
169	MOCA	1	2006.7 - 2010.6	3.9								211	PRAT	2	2007.1 - 2011.9	4.8				Other				
170	MODA	1	2004.0 - 2016.4	12.4								212	PRAT	3	2011.9 - 2016.4	4.5	Ant		Ecc	Rec				
171	MOGN	1	2004.8 - 2008.2	3.4								213	PUYV	1	2004.7 - 2009.9	5.2								
172	MOGN	2	2008.2 - 2015.0	6.8	Ant	Rad			Rec			214	PUYV	2	2009.9 - 2016.4	6.5	Ant	Rad		Rec				
173	MOLA	1	2007.5 - 2008.6	1.0								215	PUEC	1	2007.5 - 2015.0	7.5								
174	MOLA	2	2008.6 - 2015.0	6.4	Ant			Rec				216	PUYA	1	2005.9 - 2016.4	10.5								
175	MOLV	1	2011.5 - 2015.0	3.5								217	RABU	1	2004.0 - 2015.8	11.8								
176	MONT	1	2007.5 - 2015.0	7.5								218	RIED	1	2004.0 - 2006.4	2.3								
177	MOUS	1	2007.5 - 2014.0	6.5								219	RIXH	1	2011.2 - 2016.4	5.2								
178	MPRA	1	2005.0 - 2016.4	11.4								220	ROVE	1	2006.2 - 2009.7	3.5								
179	MTPL	1	2004.0 - 2013.9	9.9								221	ROVE	2	2010.1 - 2014.0	3.9	Ant		Rec					
180	NICA	1	2004.0 - 2013.0	9.0								222	ROVE	3	2014.0 - 2016.4	2.4	Ant		Rec					
181	NICA	2	2013.0 - 2015.0	2.0	Ant			Rec				223	ROHR	1	2004.0 - 2006.4	2.3								
182	NICE	1	2004.0 - 2016.4	12.4								224	ROSD	1	2006.0 - 2016.4	10.5								
183	NOVE	1	2009.4 - 2012.4	3.0								225	RSTL	1	2004.0 - 2016.4	12.4								
184	NOVE	2	2012.4 - 2016.4	4.0				Other				226	SAPI	1	2010.0 - 2015.0	5.0								
185	OATO	1	2005.8 - 2015.0	9.2								227	SAUV	1	2004.5 - 2016.4	12.0								
186	OBE2	1	2004.0 - 2007.7	3.7								228	SBG2	1	2008.8 - 2016.4	7.6								
187	OBE4	1	2012.7 - 2016.4	3.7								229	SBGZ	1	2004.2 - 2006.5	2.3								
188	OGAG	1	2011.5 - 2014.0	2.5								230	SETE	1	2007.8 - 2012.1	4.3								
189	OGAG	2	2014.0 - 2015.0	1.0				Other				231	SETE	2	2012.1 - 2016.4	4.3			Other					
190	OGAG	3	2015.0 - 2016.4	1.4				Other				232	SIMA	1	2008.9 - 2015.0	6.1								
191	PADO	1	2004.0 - 2013.7	9.7								233	SJDV	1	2004.0 - 2016.4	12.4								
192	PADO	2	2013.7 - 2016.4	2.7	Ant			Rec				234	SLVT	1	2007.7 - 2014.8	7.1								
193	PALI	1	2007.9 - 2015.0	7.1								235	SOND	1	2006.6 - 2012.9	6.4								
194	PALI	2	2015.0 - 2016.4	1.4				Other				236	SOPH	1	2004.0 - 2016.4	12.4								
195	PARD	1	2007.9 - 2015.9	8.0								237	SOUR	1	2009.4 - 2015.0	5.6								
196	PARO	1	2009.0 - 2015.0	6.0								238	SPRN	1	2007.6 - 2011.4	3.8								
197	PAZO	1	2007.9 - 2011.8	3.9								239	SPRN	2	2011.4 - 2016.4	5.0	Ant		Rec					
198	PAZO	2	2011.8 - 2016.2	4.3	Ant	Rad		Rec				240	STEY	1	2004.0 - 2016.4	12.4								
199	PFA2	1	2008.8 - 2016.4	7.6								241	STGR	1	2007.5 - 2015.0	7.5								
200	PFAN	1	2004.2 - 2007.9	3.7								242	STJ9	1	2004.0 - 2016.4	12.4								
201	PIGN	1	2007.5 - 2015.0	7.5								243	STMR	1	2008.3 - 2009.2	1.0								
202	PLOE	1	2006.9 - 2016.4	9.5								244	STMR	2	2009.2 - 2015.2	6.0			Other					

Annex B. Discontinuities

No.	Site	Sol	Start	End	T_{obs}	Discontinuity due to						
						yyyy.y	yyyy.y	yy.y	Ant	Rad	Ecc	Rec
245	STMR	3	2015.3 -	2016.4	1.1							Other
246	SUSE	1	2011.4 -	2016.4	5.0							
247	TENC	1	2004.5 -	2009.6	5.2							
248	TENC	2	2009.6 -	2014.5	4.9	Ant						Rec
249	TLSE	1	2004.0 -	2009.5	5.5							
250	TORI	1	2004.8 -	2009.8	5.0							
251	TORI	2	2014.0 -	2016.4	2.4	Ant			Ecc	Rec		
252	TRES	1	2007.6 -	2015.0	7.4							
253	TRF2	1	2008.2 -	2010.4	2.2							
254	TRF2	2	2008.4 -	2011.6	3.2	Ant			Rec			
255	TRF2	3	2011.8 -	2016.4	4.6	Ant	Rad	Ecc	Rec			
256	TRIE	1	2005.0 -	2016.4	11.4							
257	TROC	1	2008.7 -	2015.0	6.3							
258	TROP	1	2005.7 -	2015.8	10.1							
259	UDI1	1	2006.4 -	2016.4	10.0							
260	UNPG	1	2014.0 -	2016.4	2.4							
261	VALD	1	2009.4 -	2015.0	5.6							
262	VARM	1	2012.6 -	2016.4	3.8							
263	VAUC	1	2008.6 -	2013.4	4.8							
264	VAUC	2	2013.4 -	2015.0	1.6				Other			
265	VEN1	1	2010.0 -	2016.4	6.5							
266	VERN	1	2010.6 -	2016.3	5.8							
267	VFCH	1	2005.4 -	2008.5	3.0							
268	VFCH	2	2008.5 -	2012.7	4.2				Other			
269	VFCH	3	2012.8 -	2016.4	3.6	Ant			Rec			
270	VIGY	1	2010.4 -	2014.7	4.3							
271	VLCH	1	2004.0 -	2010.4	6.4							
272	VLCH	2	2010.4 -	2016.4	6.0	Ant	Rad		Rec			
273	VLKM	1	2004.0 -	2005.8	1.8							
274	VLKM	2	2005.8 -	2006.0	0.2				Other			

No.	Site	Sol	Start	End	T_{obs}	Discontinuity due to							
						yyyy.y	yyyy.y	yy.y	Ant	Rad	Ecc	Rec	Other
275	VLKM	3	2006.0 -	2007.2	1.2							Other	
276	VLKM	4	2007.2 -	2007.9	0.7							Other	
277	VLKM	5	2008.0 -	2008.2	0.2							Other	
278	VLKM	6	2008.9 -	2009.7	0.8							Rec	
279	VLKM	7	2010.4 -	2011.4	1.0							Rec	
280	VLKM	8	2011.4 -	2014.1	2.7							Rec	
281	VLKM	9	2014.1 -	2015.1	1.0							Rec	
282	VLKM	10	2015.3 -	2016.4	1.1	Ant	Rad	Ecc	Rec				
283	WART	1	2005.6 -	2016.1	10.5								
284	WELS	1	2005.3 -	2010.2	4.9								
285	WELS	2	2010.2 -	2016.4	6.2	Ant	Rad					Rec	
286	WIEN	1	2004.0 -	2009.0	5.0								
287	WIEN	2	2014.2 -	2015.0	0.8	Ant	Rad	Ecc	Rec				
288	WIEN	3	2015.0 -	2016.4	1.4	Ant	Rad	Ecc	Rec				
289	WLBH	1	2004.0 -	2016.4	12.4								
290	WT21	1	2010.8 -	2016.4	5.6								
291	WTZR	1	2004.0 -	2009.5	5.5								
292	WTZR	2	2010.5 -	2016.4	5.9	Ant						Rec	
293	ZADA	1	2011.7 -	2016.4	4.7								
294	ZIM2	1	2009.4 -	2013.8	4.4								
295	ZIM2	2	2013.8 -	2016.4	2.6							Rec	
296	ZIMM	1	2004.0 -	2016.4	12.4								
297	ZOUF	1	2005.0 -	2016.4	11.4								

Total number of changes 58 33 13 56 22

Shortcuts:

Ant – antenna change

Rad – radom change

Ecc – antenna eccentricity change

Rec – receiver change

Sol – solution number